

AD-A254 243



MENTATION PAGE

Form Approved
OMB No. 0704-0188

is estimated to average 1 hour per response, including the time for reviewing instructions, searching existing data sources, gathering and reviewing the collection of information, sending comments regarding this burden estimate or any other aspect of this collection of information, including this burden estimate, to Washington Headquarters Services, Directorate for Information Operations and Reports, 1215 Jefferson Davis Highway, Suite 1204, Arlington, VA 22202-4302, and to the Office of Management and Budget, Paperwork Reduction Project (0704-0188), Washington, DC 20503.

1. AGENCY USE ONLY (Leave blank)	2. REPORT DATE 1991	3. REPORT TYPE AND DATES COVERED THESIS	
4. TITLE AND SUBTITLE The Effect of Electron-Density Gradients on Propagation of Radio Waves in the Mid-Latitude Trough		5. FUNDING NUMBERS <div style="border: 1px solid black; border-radius: 50%; width: 40px; height: 40px; display: flex; align-items: center; justify-content: center; margin: 10px auto;">1</div>	
6. AUTHOR(S) Peter J. Citrone, Captain			
7. PERFORMING ORGANIZATION NAME(S) AND ADDRESS(ES) AFIT Student Attending: Utah State University		8. PERFORMING ORGANIZATION REPORT NUMBER AFIT/CI/CIA-92-058	
9. SPONSORING/MONITORING AGENCY NAME(S) AND ADDRESS(ES) AFIT/CI Wright-Patterson AFB OH 45433-6583		10. SPONSORING/MONITORING AGENCY REPORT NUMBER	
11. SUPPLEMENTARY NOTES			
12a. DISTRIBUTION/AVAILABILITY STATEMENT Approved for Public Release IAW 190-1 Distributed Unlimited ERNEST A. HAYGOOD, Captain, USAF Executive Officer		12b. DISTRIBUTION CODE	
13. ABSTRACT (Maximum 200 words) <div style="text-align: center; margin-top: 20px;">SDTIC ELECTE AUG 26 1992 A D</div> <div style="text-align: right; margin-top: 20px;">92-23626 </div> <div style="margin-top: 20px;">92 8 25 060</div>			
14. SUBJECT TERMS		15. NUMBER OF PAGES 153	
		16. PRICE CODE	
17. SECURITY CLASSIFICATION OF REPORT	18. SECURITY CLASSIFICATION OF THIS PAGE	19. SECURITY CLASSIFICATION OF ABSTRACT	20. LIMITATION OF ABSTRACT

THE EFFECT OF ELECTRON-DENSITY GRADIENTS
ON PROPAGATION OF RADIO WAVES
IN THE MID-LATITUDE TROUGH

by

Peter J. Citrone

A thesis submitted in partial fulfillment
of the requirements for the degree

of

MASTER OF SCIENCE

in

Physics

(Upper Atmosphere Option)

Approved:

Jan J. Sijka
Major Professor

Kay D. Baker
Committee Member

Bl. Feyn
Committee Member

Lawrence A. Tuttle
Dean of Graduate Studies

Accession	
NTIS	<input checked="" type="checkbox"/>
DTIC	<input type="checkbox"/>
Unann	<input type="checkbox"/>
Justi	<input type="checkbox"/>
By	
Date	
Doc	
A-1	

UTAH STATE UNIVERSITY
Logan, Utah

1991

DTIC QUALITY INSPECTED 1

ACKNOWLEDGEMENTS

I am most indebted to my advisor, Dr. Jan Sojka, for his guidance, resources, and assistance throughout this entire effort. Our discussions, work-sessions, and hall-meetings provided the background and impetus I needed to conduct this study. Jan especially helped me through the problems I encountered with the ray-tracing program, the interface with his model output, modification of the model output, and the writing of this thesis.

Dr. Jurgen Buchau was also instrumental throughout my research. During my visit to the Geophysics Laboratory and numerous phone calls, Jurgen put aside a busy schedule to answer my questions on radio-wave propagation, the observational campaign, the OTH-B radar, and the digisonde measurements. He also provided the digisonde measurements, which were crucial data in my research. Dr. Bill Denig and Dr. Fred Rich provided the DMSP measurements and the interplanetary magnetic field data, and answered questions regarding these data. Dr. Jim Whalen, Dr. Jim Moore, Dr. Ed Weber, Dr. S. Basu, and Dr. B. Dandekar also assisted me while at the Geophysics Laboratory. Mike Squires and Pete Speck from the USAF Environmental Technical Applications Center (ETAC) provided data from the ETAC climatic database. Capt. Gary Huffines, Ron Lepping, Rob Daniell, Barb Emery, Maj. Richard Peer, and Capt Randy Thomas all provided important data and/or guidance.

I would also like to express my gratitude to my other committee members, Dr. Bela Fejer and Dr. Kay Baker, for their assistance in the final phases. Dr. Fejer and Dr. David Crain helped me to grasp some of the more complex radio-

propagation concepts. Dr. Vince Wickwar also gave his valuable time to answer questions regarding incoherent scatter radar data. My fellow office mates, Capt. Tom Frooninckx and Capt David Payne, provided insight, arguments, and answers to my questions. They put up with me. Graduate student Eric Kluzek was especially helpful with the conversion of the ray-tracing program.

Linda, you held me together through the many frustrations and gave me the encouragement I needed to survive. I'm very happy I made you my wife, and we brought a beautiful son into the world. Zachary, you kept me sane and insane. For this, I thank you. I'd also like to extend my gratitude to my parents; educating me was not easy. Finally, I'd like to thank God this is over.

Peter J. Citrone

TABLE OF CONTENTS

	Page
ACKNOWLEDGEMENTS	ii
LIST OF TABLES	v
LIST OF FIGURES	vi
ABSTRACT	xii
Chapter	
I. INTRODUCTION	1
II. RADIO-WAVE PROPAGATION AND THE MID-LATITUDE TROUGH	7
III. IONOSPHERIC MEASUREMENTS	36
IV. MODIFICATION OF TIME-DEPENDENT IONOSPHERIC MODEL OUTPUT WITH LATITUDINAL ELECTRON- DENSITY PROFILES FROM DIGISONDE TROUGH DEPICTIONS	67
V. RAY-TRACING SIMULATIONS TO EXAMINE GROUND RANGE	86
VI. EFFECTS OF THREE-DIMENSIONAL GRADIENTS IN ELECTRON DENSITY ON RADIO-WAVE PROPAGATION IN THE TROUGH REGION	119
VII. CONCLUSIONS	143
VIII. RECOMENDATIONS FOR FUTURE RESEARCH	147
REFERENCES	148
APPENDIX	150

LIST OF TABLES

Table	Page
1. Summary of Geophysical Conditions	41
2. Season	68
3. Solar Activity Level	68
4. Geomagnetic Activity Level	68
5. Summary of Ground-Range Tests at 6.0 MHz	100
6. Largest Ground-Range Differences at Each Azimuth	103
7. Conditions for Vertical Ray Refraction to Surface	138
8. Ray-Tracing Fixed-Input Conditions	153

LIST OF FIGURES

Figure	Page
1. The effect of a one-dimensional gradient in electron density on ray propagation, as expressed by Snell's law	12
2. Breit and Tuve's theorem depicting the true path TBR, virtual path TAR, true height h , virtual height h' , and ground range TR of a radio wave refracting in the ionosphere	14
3. Ray-propagation geometry for various ray frequencies at a fixed elevation angle	16
4. Ray-propagation geometry for a fixed frequency at various elevation angles	18
5. The effect of strong horizontal electron-density gradients from the trough poleward wall on radio-wave propagation	20
6. The effects of an enhanced E region on radio-wave propagation	22
7. Relative positions of the high-latitude plasma convection pattern, main trough, ionization hole, and quiet-time auroral oval	25
8. Contour maps of average $\log_{10} N_m F_2$ (cm^{-3}) over Millstone Hill, Massachusetts plotted as functions of local time and invariant latitude	26
9. Atmospheric Explorer-C satellite measurements of horizontal ion-drift velocity components and total-ion concentration at 250 km altitude in the evening MLT sector	28
10. Depiction of the stagnation line in the plasma convection pattern of the evening sector in a non-rotating coordinate system	32

11.	Mid-latitude plasma convection trajectories in the <i>Spiro et al.</i> [1978] stagnation-line model, plotted in dipole latitude and solar local time (SLT) coordinates	33
12.	Location of the GL aircraft track with respect to the coverage area of the East Coast Radar System (ECRS)	37
13.	Location of the GL aircraft track, Goose Bay (65° CGLAT), Argentia (58° CGLAT), and DMSP F8 and F9 satellite passes in corrected geomagnetic coordinates	38
14.	10.7-cm solar-flux values from February to April 1989	42
15.	3-Hour Kp index-values from 2-8 March 1989	43
16.	Hourly averages of the magnitude of the average field vector of the IMF (B), and the B_y and B_z IMF components (in geocentric solar magnetospheric coordinates) from the IMP-8 satellite	45
17.	Digisonde trough depictions for the three experimental periods	50
18.	Millstone Hill incoherent scatter radar depictions of the trough for the last two experimental periods	53
19.	Latitudinal $N_m F_2$ gradients of the equatorward wall calculated from the digisonde and incoherent scatter radar trough depictions	56
20.	Latitudinal $N_m F_2$ gradients of the poleward wall calculated from the digisonde and incoherent scatter radar trough depictions	57
21.	Latitudinal trough profiles at 1830-0200 CGMLT, taken from the digisonde $N_m F_2$ trough depictions for the first experimental period	59

22.	Latitudinal trough profiles at 1830-0200 CGMLT, taken from the digisonde $N_m F_2$ trough depictions for the second experimental period	60
23.	Latitudinal trough profiles at 1830-0200 CGMLT, taken from the digisonde $N_m F_2$ trough depictions for the third experimental period	61
24.	Latitudinal trough profiles at 2000-0200 CGMLT, taken from the Millstone Hill incoherent scatter radar $N_m F_2$ trough depictions for the second experimental period	62
25.	Invariant latitude (INV LAT) trough profiles derived from DMSP electron-density measurements at 868 km altitude	65
26.	Latitudinal profiles of $N_m F_2$ from the TDIM trough representation for one-hour MLT bins, centered at 1830-0230 MLT	71
27.	Latitudinal profiles of $N_m F_2$ from the digisonde trough depictions for the first experimental period	72
28.	Latitudinal profiles of $N_m F_2$ from the digisonde trough depictions for the second experimental period	73
29.	Latitudinal profiles of $N_m F_2$ from the digisonde trough depictions for the third experimental period	74
30.	Modification of original TDIM vertical gradients by inserting a reduced $N_m F_2$ value and applying a logarithmic vertical scaling factor	77
31.	Trough representations resulting from modification by digisonde latitudinal $N_m F_2$ profiles and DMSP latitudinal electron-density gradients of the trough wall	78
32.	Latitudinal $N_m F_2$ gradients of the equatorward wall calculated from the TDIM and digisonde trough depictions	82

33.	Latitudinal $N_m F_2$ gradients of the poleward wall calculated from the TDIM and digisonde trough depictions	83
34.	Trough representations depicted in contours of $\log_{10} O^+$ concentration at 300 km altitude in MLAT-MLT coordinates (TDIM and digisonde troughs from period one)	89
35.	Trough representations depicted in contours of $\log_{10} O^+$ concentration at 300 km altitude in MLAT-MLT coordinates (digisonde troughs from periods two and three)	90
36.	Trough representations depicted in contours of $\log_{10} O^+$ concentration at 300 km altitude in MLAT-MLT coordinates (DMSP troughs from period one)	91
37.	Ray-tracing results of ground-range tests for a range of elevation angles (10-60°) at a fixed frequency of 6.0 MHz and an azimuth of 63.0°	95
38.	Ray-tracing results of ground-range tests for a range of elevation angles (10-60°) at a fixed frequency of 6.0 MHz and an azimuth of 53.5°	96
39.	Ray-tracing results of ground-range tests for a range of elevation angles (10-60°) at a fixed frequency of 6.0 MHz and an azimuth of 40.0°	97
40.	Ray-tracing results of ground-range tests for a range of elevation angles (10-60°) at a fixed frequency of 6.0 MHz and an azimuth of 0.0°	98
41.	Ground-range difference and ground-range ratio for ray-tracing test results from the first experimental period at a fixed frequency of 6.0 MHz and an azimuth of 63.0°	105
42.	Ground-range difference and ground-range ratio for ray-tracing test results from the first experimental period at a fixed frequency of 6.0 MHz and an azimuth of 53.5°	106

43.	Ground-range difference and ground-range ratio for ray-tracing test results from the first experimental period at a fixed frequency of 6.0 MHz and an azimuth of 40.0°	107
44.	Ground-range difference and ground-range ratio for ray-tracing test results from the first experimental period at a fixed frequency of 6.0 MHz and an azimuth of 0.0°	108
45.	Ray-tracing results of ground-range tests from the first experimental period for a range of frequencies (3.0-13.0 MHz) at a fixed elevation angle (18.0°) and an azimuth of 63.0°	111
46.	Ray-tracing results of ground-range tests from the first experimental period for a range of frequencies (3.0-13.0 MHz) at a fixed elevation angle (25.0°) and an azimuth of 53.5°	112
47.	Ray-tracing results of ground-range tests from the first experimental period for a range of frequencies (3.0-13.0 MHz) at a fixed elevation angle (30.0°) and an azimuth of 40.0°	113
48.	Ray-tracing results of ground-range tests from the first experimental period for a range of frequencies (3.0-13.0 MHz) at a fixed elevation angle (30.0°) and an azimuth of 0.0°	114
49.	Ground-range difference and ground-range ratio for ray-tracing test results from the first experimental period at a fixed frequency of 10.0 MHz and an azimuth of 63.0°	117
50.	Log ₁₀ X and the three-dimensional gradients of electron density along the ray-path (63.0° azimuth, 12.9° elevation, 6.0 MHz frequency)	123
51.	Log ₁₀ X and the three-dimensional gradients of electron density along the ray path (53.5° azimuth, 18.7° elevation, 6.0 MHz frequency)	126

52.	Log ₁₀ X and the three-dimensional gradients of electron density along the ray path (40.0° azimuth, 25.4° elevation, 6.0 MHz frequency)	129
53.	Log ₁₀ X and the three-dimensional gradients of electron density along the ray path (63.0° azimuth, 10.0° elevation, 6.0 MHz frequency)	132
54.	Log ₁₀ X and the three-dimensional gradients of electron density along the ray path (63.0° azimuth, 10.0° elevation, 11.0 MHz frequency)	134
55.	Altitude profiles of log ₁₀ N _e (cm ⁻³) along the TDIM ray path from Figure 53	136
56.	Ground projection of the ray path from Figure 54 in MLAT-MLT coordinates	141

ABSTRACT

The Effect of Electron-Density Gradients on Propagation
of Radio Waves in the Mid-Latitude Trough

by

Peter J. Citrone, Master of Science

Utah State University, 1991

Major Professor: Dr. Jan J. Sojka
Department: Physics

This thesis examines high-frequency radio propagation in the mid-latitude trough through the use of a numerical ray-tracing computer program. The trough representation from a sophisticated ionospheric model (Time-Dependent Ionospheric Model) is altered by inserting latitudinal profiles of electron density from digisonde measurements in the mid-latitude trough. The resulting modifications to the model output are realistic of the large-scale electron-density structure in the mid-latitude trough. Ray-tracing simulations through the original and modified model output reveal large ground-range errors (200-1600 km) for rays which refract in the trough equatorward wall of the modified model output. The source of the ground-range error is the overestimation of electron density in the trough by the model, which causes the vertical electron-density gradients to be falsely enhanced in the original model output. Rays that reach apogee in the

trough base of the realistic digisonde trough representations are usually trapped, or they penetrate the entire ionosphere. Horizontal deviations of rays which propagate through the strong latitudinal electron-density gradients of the trough wall from the realistic digisonde trough representations are typically less than ten km.

(164 pages)

CHAPTER I

INTRODUCTION

Mankind uses high-frequency (HF) radio propagation systems to obliquely bounce radio pulses (rays) off the ionosphere for three general purposes: point-to-point telecommunication, navigation, and over-the-horizon radar surveillance. This study was designed to investigate environmental problems associated with the over-the-horizon backscatter (OTH-B) radar in the region of the mid-latitude ionospheric trough. However, the lessons learned from this study can be applied to the other HF radio-propagation systems as well, since they operate under the same physical principles.

Over-the-horizon backscatter radars utilize oblique-propagation principles to transmit HF (5-28 MHz) radio pulses through the ionosphere to locate aircraft within a range of approximately 800-3700 km. The OTH-B radar at Bangor Air Force Base in Maine often experiences radio-wave (ray) deviation and distortion problems when operating in the mid-latitude ionospheric trough (R. Peer, private communication, 1990), a plasma-depleted region just equatorward of the auroral oval in the nightside F region.

Often rays which propagate into the trough penetrate the entire ionosphere and escape to space. Another problem associated with the trough is its tendency to trap rays; they neither ascend nor descend through the ionosphere. Such rays may eventually land, but at such a great distance that their signal strength is weakened too much to be of use in detecting targets. Additionally, the strong

horizontal electron-density gradients in the poleward and equatorward trough walls cause large ground-range and azimuthal deviations in the ray paths, thereby producing significant errors in the location of the received signal (J. Buchau, private communication, 1990). All of these problems affect the refraction of the ray as it propagates through the trough.

An additional problem associated with the trough is the presence of significant small-scale (tens of km) fluctuations in the plasma density (called plasma irregularities), which cause the transmitted ray to lose signal-strength relative to the ambient-noise level. This distortion problem, though significant, will not be addressed in this study, because it requires the inclusion of small-scale plasma irregularities in the depiction of the troughs to be used in ray-tracing simulations. The trough depictions used in this study include only large-medium scale electron-density structure, because the primary measurement techniques used to develop the trough depictions are not capable of detecting the smaller-scale irregularities. Additionally, the effects of realistic large scale electron-density gradients found in the trough walls on ray propagation are not well known.

In order to detect the aircraft, the OTH-B radar operator must know the general location the transmitted ray interacts with the ionosphere. Since the ionosphere is a dynamic propagation medium, with diurnal, seasonal, solar-cycle, geomagnetic-activity level, and latitudinal dependencies, the radar operator often encounters problems interpreting the state of the ionosphere. To illuminate a specific target at a known location with the radar pulse, the operator must know (in advance) the electron-density structure and behavior of the ionosphere in the

direction of the radar pulse at altitudes ranging from about 60-400 km.

The OTH-B radar operator is responsible for surveillance over a wide area within the radar's range. To accomplish this, the electron-density structure over the surveillance area must be predicted by an ionospheric model. If the ionospheric-model prediction is not representative of actual conditions, the ray does not land where the operator intends. According to *Dandekar* [1985] (p. 10-38),

a model is a numerical statistical description of the ionosphere in terms of location (geographic or geomagnetic latitudes and longitudes), time (solar zenith angle), seasons, and other factors such as the solar activity (10.7 cm solar flux, sunspot number).

There are three main types of ionospheric models: statistical, empirical, and physical [*Rush*, 1986]. Statistical models are the most common type of model used as ionospheric radio-propagation models. A statistical model is derived from a global climatology of ionospheric measurements, most commonly monthly-median values of the critical frequency of the E, F₁, and F₂ regions. These representations are often not very accurate, especially in regions that are characterized by rapid spatial or temporal changes in electron density (electron-density gradients). Their advantages are their simplicity and wide availability. An example of a statistical model used widely for radio-communication purposes is the IONCAP model [*Dandekar*, 1985].

Empirical models combine certain features of the statistical and physical models to simulate the electron-density structure of the ionosphere on a global scale. They combine a simplified theoretical model of the ionosphere, which is

based on the chemistry of the lower regions (i.e., Chapman theory of the E and F₁ regions), with a global statistical model of the more complex F₂ region. The International Reference Ionosphere (IRI) is a widely-known empirical model used to predict the electron and ion composition, density, and temperature of the D, E, F₁, and F₂ regions [*Rush*, 1986].

The most sophisticated, and usually the most realistic, ionospheric models are the physical models. They are based on the physical processes which control the structure and behavior of the ionosphere. Since they numerically solve time-dependent equations which describe the physical mechanisms that form and control the ionosphere as functions of altitude, location, and time, they require high-speed computers to run their sophisticated software. The most complex physical model available is the one developed by *Sojka and Schunk* [1983], called the Time-Dependent Ionospheric Model (TDIM).

The TDIM numerically solves the F-region ion continuity and momentum equations and the F-region ion and electron energy equations for the following ions: NO⁺, O₂⁺, N₂⁺, O⁺, N⁺, and He⁺. Processes that are simulated in the TDIM include multi-ion chemistry, photoionization and auroral ionization, ambipolar plasma diffusion, plasma transport, neutral winds, and the ion-electron-neutral thermal balance. *Schunk* [1988] and *Sojka* [1989] published recent review articles describing the TDIM, its development, and theoretical model studies.

The goal of this study is to better understand ray refraction in the nightside trough. I hope to quantify the specific trough electron-density conditions that cause rays which enter into the trough to experience significant ground-range

errors and large horizontal (azimuthal) deviations. I used digisonde (digital ionosonde) measurements to develop realistic trough electron-density distributions. The digisonde measurements originated from an observational campaign in March 1989 designed to test OTH-B radar performance in the trough (J. Buchau, private communication, 1990). Since the digisonde trough measurements are available at least hourly at several locations in the trough region, they have the capability of providing a near-real time, reasonably accurate trough depiction for use in ray-tracing simulations.

To simulate ray propagation in the mid-latitude trough, I used the *Jones and Stephenson* [1975] ray-tracing program in conjunction with the TDIM and digisonde trough representations. Prior to the ray-tracing tests, I compared the TDIM trough representation with the digisonde trough depictions from the observational campaign to identify any major differences which would lead to disagreement in the ray-tracing simulations. Large differences in ray-tracing results between rays which propagated in the TDIM and digisonde troughs would indicate the severity of the trough-modelling problem, since the TDIM trough representation is regarded as the most realistic trough simulation available.

I will first review oblique radio-propagation fundamentals and mid-latitude trough morphology and trough-formation mechanisms (Chapter II). In Chapter III, I will examine geophysical conditions during the observational campaign and the ionospheric electron-density measurements used to develop realistic trough depictions. In Chapter IV, I will compare the digisonde trough representation with the TDIM trough representation for the appropriate geophysical conditions. I will

also describe the process of modifying the TDIM trough representation for use as the propagation medium in the ray-tracing simulations. Next, I will describe the ray-tracing simulations performed through the TDIM and realistic trough representations, present the results, and discuss the physical processes which cause the various ray-path behaviors (Chapters V and VI). In Chapter VII, I will present my conclusions. I will make recommendations for future study in Chapter VIII.

CHAPTER II

RADIO-WAVE PROPAGATION AND THE MID-LATITUDE TROUGH

Overview of Radio-Wave Propagation

I will review the morphology and formation of the mid-latitude trough in the second part of this review chapter. The first part of this chapter will primarily cover some of the fundamentals of oblique radio propagation, that is, ray propagation incident on the lines of constant electron density at an oblique angle. In oblique propagation, high-frequency radio waves (3-30 MHz) refract as they propagate through vertical electron-density gradients in the ionosphere. *Davies* [1965, 1969] and *Budden* [1961] have published highly detailed textbooks on the subject.

A simplified treatment of oblique propagation neglects the effects of the geomagnetic field, electron-neutral collisions, and ionospheric curvature. However, only ionospheric curvature, as opposed to a flat ionosphere approximation, significantly affects radio-wave refraction, except for specialized circumstances. For instance, the geomagnetic field causes unusual propagation effects if the wave frequency does not exceed the gyrofrequency [*Dieminger*, 1968]. Additionally, an enhanced D region may cause all of the ray's energy to be lost to the neutral population (total ray absorption), thereby halting propagation of the ray.

Vertical-incidence radio propagation is not directly used for radio communication, navigation, or over-the-horizon surveillance purposes. However,

vertical-incidence sounding with ionosondes is a vital tool in the study of ionospheric structure directly over the ionosonde. Also, vertical-incidence principles are fairly simple, so they are often used to introduce the more complex topic of oblique propagation.

Ionospheric Sounding Principles

Ionospheric sounding involves the use of an ionosonde to transmit a radio-wave pulse at vertical incidence. Assuming the pulse reflects (as opposed to penetrates the entire ionosphere), the radar echo is received at the same location it was transmitted from. The elapsed time from transmission to reception is used to calculate the virtual reflection height, with the assumption the radio pulse travels at the speed of light in a vacuum (c). This simplified explanation is not entirely correct, however, because the radio pulse actually travels at the group velocity (u), which is somewhat slower than c . The reflection height calculated for a pulse assumed to travel at the speed of light is called the virtual height, which is always somewhat greater than the actual (true) height.

The refractive index of a medium is a measure of the amount of refraction a wave encounters as it propagates through the medium. In oblique radio-wave propagation, the vertical variation of electron density in the ionosphere is manifested as a vertical variation of refractive index. Much as in the propagation of light waves through a medium (i.e., glass) with a changing refractive index, radio waves propagating through ionospheric plasma interact with a variable refractive index and bend towards the region with the higher refractive index. Neglecting the

effects of earth's magnetic field and collisions between electrons and the neutral atmospheric constituents, the refractive index (n) can be calculated at a given location,

$$n^2 = 1 - X = 1 - (f_p^2 / f^2) \quad (1)$$

$$X = N_e e^2 / 4\pi^2 \epsilon_0 m f^2 \quad (2)$$

where f_p is plasma frequency, f is wave frequency, N_e is electron density, e is elementary unit of charge, ϵ_0 is permittivity of free space, and m is electron rest mass.

In the ionosphere, the vertical variation of electron density is usually much larger than the horizontal variations (latitude and longitude). Below the ionosphere, $X = 0$ ($N_e = 0$), so $n = 1$. Within the ionosphere, $N_e > 0$, so $n < 1$. The refractive index decreases as the ray propagates higher in altitude through increasing electron density.

For vertical-incidence sounding, the ray undergoes a reflection back towards the surface at the altitude where the ray frequency is equal to the plasma frequency, so $n = 0$ ($X = 1$) at ray apogee. If the ray frequency exceeds the maximum plasma frequency of the ionosphere overlying the transmitter, the ray penetrates the entire ionosphere and escapes to space. The maximum plasma frequency of each ionospheric layer is called the critical frequency of that layer. The highest electron density is in the F_2 region, except during periods of enhanced auroral activity, when the auroral-E region peak electron density may exceed the F -region peak density. Otherwise, the F_2 region critical frequency (f_oF_2) is the

critical (or penetration) frequency of the whole ionosphere.

The plasma frequency at a specific location and altitude can be used to calculate the electron density,

$$N_e = 1.24 \times 10^4 f_n^2 \quad (3)$$

where N_e is electron density in electrons/cm³ and f_n is plasma frequency in MHz. This relation results from inserting the constants into equation (2) and rearranging to solve for N_e .

The ionosphere affects radio-wave transmission in two general ways. First, a wave propagating along a path with a changing electron density experiences refraction, and for certain conditions, reflection. Second, the electron population of the ionosphere absorbs energy from the wave, which it then transfers to the neutral atmospheric constituents via collisions, thereby attenuating the signal. Signal attenuation is especially important in the D region. I will not further discuss radio-wave absorption in this review. *Hargreaves* [1979] and *Chamberlain and Hunten* [1987] review absorption theory in detail.

Radio-Wave Refraction

Radio-wave refraction in the ionosphere arises from the effect of free electrons on the phase velocity of the propagating radio wave. Phase velocity (v) is the velocity at which planes of constant phase propagate and is equal to the product of the wave frequency and wavelength. The phase velocity is related to

the speed of light in a vacuum by,

$$v = c (1 - N_e e^2 / 4\pi^2 m f^2)^{-1/2} \quad (4)$$

$$v = c (1 - 8.1 \times 10^{-5} N_e / f^2)^{-1/2} \quad (5)$$

For a given wave frequency, phase velocity increases as electron density increases.

Since the refractive index (n) equals c/v ,

$$n = (1 - 8.1 \times 10^{-5} N_e / f^2)^{1/2} \quad (6)$$

Thus, for a given frequency, n decreases as the radio wave passes into a region of higher electron density. This relation, formally called Snell's law, demonstrates radio-wave refraction for a horizontally-stratified ionosphere, as in the highly simplified case of Figure 1 [Dieminger, 1968].

In Figure 1, a ray refracts as it passes across a sharp boundary from a region of lower to higher electron density. This can be explained by the fact that the ray's phase velocity increases as electron density increases (equation (5)). In other words, the upper portion of the wavefront moves faster than the lower part as it moves into a region of higher N_e , causing the ray to bend. As shown in Figure 1, the ray bends away from the region of higher electron density.

Another manifestation of Snell's law is that the ray bends away from the direction of the component of the electron-density gradient that is perpendicular to the ray path (as shown in Figure 1). The resultant ray trajectory is affected by the vector sum of the perpendicular components of the electron-density gradient in all three dimensions. The vertical gradient usually dominates the two horizontal

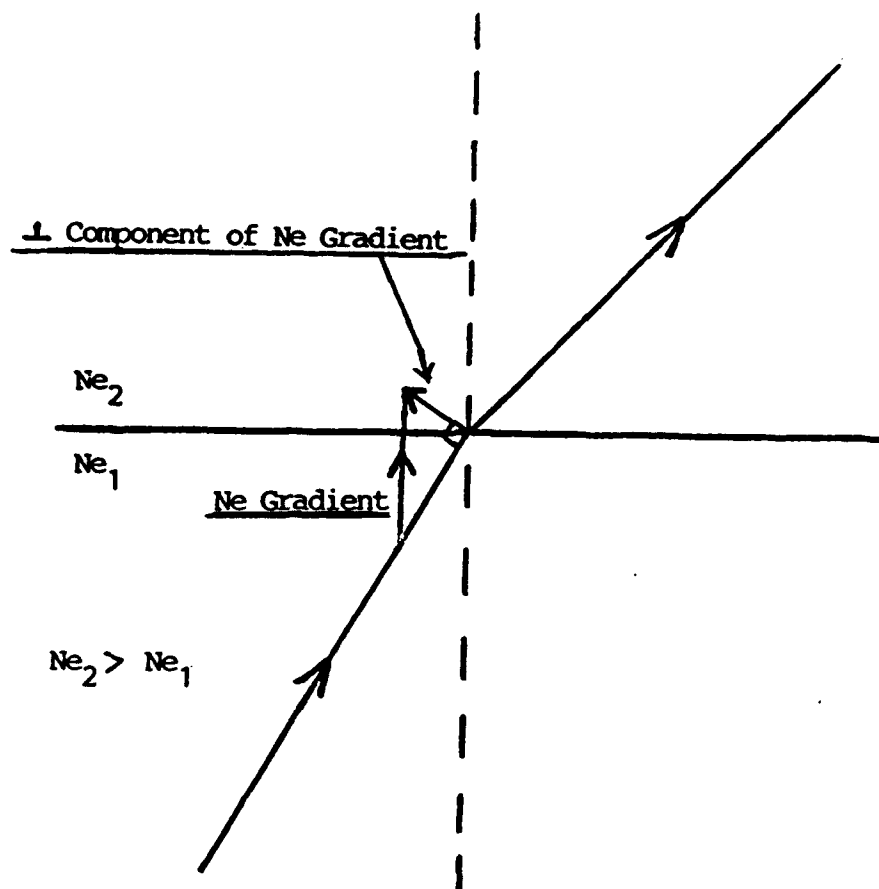


Fig. 1. The effect of a one-dimensional gradient in electron density on ray propagation, as expressed by Snell's Law. The ray bends away from the direction of the component of the gradient that is perpendicular to the path.

gradients, but under certain conditions, a strong horizontal gradient can greatly affect ray propagation, resulting in horizontal ray deviations (azimuthal deviations) [Buchau *et al.*, 1973]. Under most conditions, vertical gradients control the ray's landing point in ground range.

Ray-Propagation Geometry

As mentioned earlier, the virtual height of reflection (calculated by measuring the radio pulse's time delay between transmission and reception) is always greater than the true height of reflection. This is because the radio pulse travels at the group velocity ($u = c \times n$), which is slower than the phase velocity of propagation, ($v = c/n$, where $n < 1$). Breit and Tuve's theorem describes the geometric relationship between the virtual path and true path of ray propagation, as shown in Figure 2 [Davies, 1969].

In Figure 2, the radio wave actually follows the curved path TBR, with the true reflection height h and ground range TR. Ground range refers to the distance of the ray from the transmitter, as measured along the earth's surface. Group path is a measure of the distance the ray travels along the actual ray path. According to Breit and Tuve's theorem, the time interval for a radio wave moving at the group velocity to traverse the curved (true) path TBR is equal to the time taken for a radio wave moving at the speed of light in a vacuum to traverse the triangular (virtual) path TAR. Since the ray actually travels at the group velocity along the curved path TBR, the true height is always less than the virtual height.

Like the calculation of ground range, this calculation of virtual height is

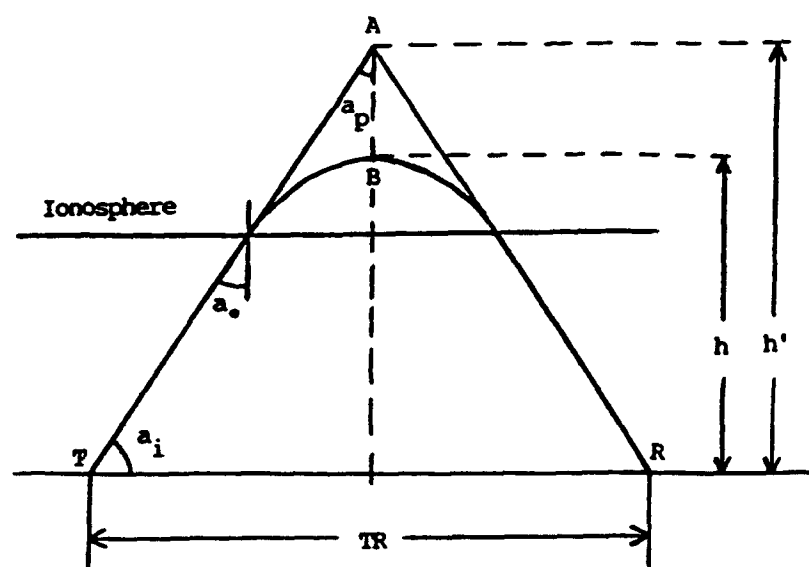


Fig. 2. Breit and Tuve's theorem depicting the true path TBR, virtual path TAR, true height h , virtual height h' , and ground range TR of a radio wave refracting in the ionosphere. Adapted from *Dieminger* [1968] and *Davies* [1969].

erroneous, because it is made under the simplifying assumptions that the ray traverses the equivalent virtual path TAR at the speed of light in a vacuum, and the ionosphere is flat and horizontally uniform. To acquire accurate values for ground range, a correction is made for a curved ionosphere, a complex geometrical operation discussed by *Dieminger* [1968] and *Davies* [1969]. A true-height analysis, as discussed in detail by *Titheridge* [1988], can be performed to acquire the true height.

The secant law relates the frequency (f) of a ray incident at the bottom of a horizontally-stratified ionosphere at an oblique angle a_0 (Figure 2) with the equivalent vertical-incidence frequency f_v (the frequency that is reflected from vertical incidence at the same true height, consequently the plasma frequency f_n at that height),

$$f = f_n (\sec a_0) \quad (7)$$

In simpler terms, the secant law indicates that a given horizontal ionospheric layer will reflect higher frequency rays as the ray-path obliquity (angle a_0) increases [*Dieminger* 1968].

Figure 3 illustrates oblique ray-propagation geometry for various frequencies at a fixed elevation angle from a fixed transmitter site. A ray transmitted at a higher frequency penetrates higher into the ionosphere before it is refracted, and eventually, returned back to earth. Such a ray also lands farther in ground range (assuming it does not penetrate the entire ionosphere), because as the ray travels farther in altitude, it also travels farther in ground range. Rays

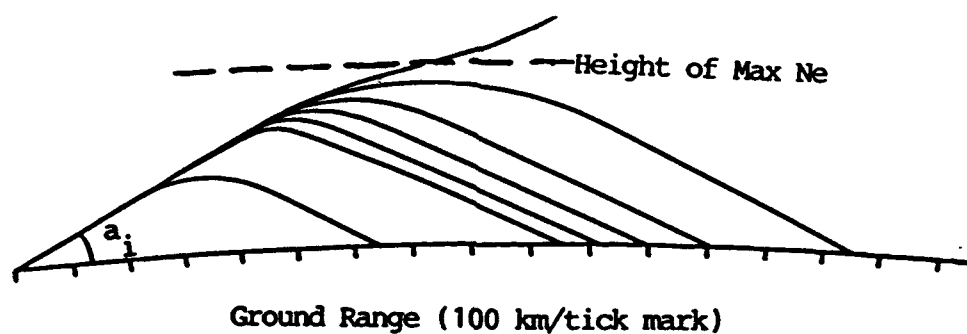


Fig. 3. Ray-propagation geometry for various ray frequencies at a fixed elevation angle (a_i). The ray apogee increases with increasing frequency until the ray reaches beyond the height of the maximum electron density, whereupon it penetrates.

which travel beyond the altitude of the maximum electron density of the ionosphere penetrate the entire ionosphere and escape to space.

Figure 4 similarly illustrates ray propagation geometry, but for a fixed frequency at various elevation angles. Generally, rays launched at higher elevation angles penetrate deeper into the ionosphere and (excluding the penetrating rays) land closer to the transmitter in ground range. For low elevation-angle rays, the propagation path is long, and the ray lands at distant ground ranges. For higher elevation-angle rays, the propagation path and ground range decrease until the skip distance is surpassed. The skip distance marks the shortest distance radio-wave reception is possible for a given frequency. The skip zone is the region where radio-wave reception is not possible for rays bounced off the ionosphere, although the ground wave will reach ground ranges of 50-300 km, depending on the wave frequency, antenna, ground conductivity and other factors.

Rays launched at higher elevation angles can be effectively trapped for a time (Figure 4) as they propagate parallel to the horizontally-stratified ionosphere. At still higher elevation angles, the rays penetrate the entire ionosphere and escape to space. This is because as the elevation angle increases, the ray eventually travels higher than the altitude of the maximum electron density. Once the ray exceeds this altitude, it escapes to space, because the vertical electron-density gradient becomes negative (decreasing density with increasing height), causing the ray to refract upward.

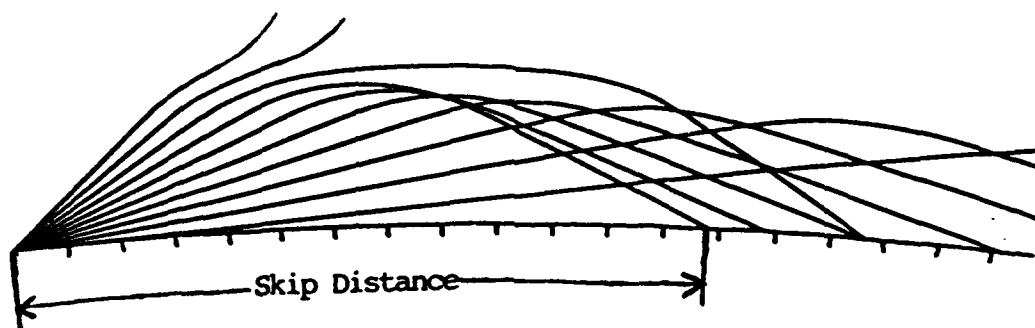


Fig. 4. Ray-propagation geometry for a fixed frequency at various elevation angles. Rays launched at higher elevation angles generally penetrate deeper into the ionosphere. The skip distance marks the shortest distance radio-wave reception is possible for a given frequency.

Complications Caused by the Ionosphere

Several complicated ray geometries are possible due to the ray path's orientation with respect to the geomagnetic field, different ionosphere layers, curvature and tilts of the layers, and magnetospheric ducting. *Davies* [1969] discusses these cases and others in detail. They won't be discussed in this review. Instead, I'll review two ionospheric effects on ray propagation of importance to this study: 1) effects of strong horizontal electron-density gradients, and 2) effects of an underlying layer, typically the E region.

The mid-latitude trough typically has the strongest horizontal electron-density gradients in the ionosphere, especially where the evening equatorward trough wall intersects the dusk terminator [*Davies and Rush*, 1985]. Trough latitudinal electron-density gradients are strong in both the equatorward and poleward trough walls, while the longitudinal gradients are strong only at the dusk and dawn terminators. Figure 5 shows the effects of strong horizontal electron-density gradients on ray-path deviation. In Figure 5, rays are incident on a trough poleward wall at varying degrees of incidence. The trough poleward wall in this depiction is a relatively narrow region characterized by a strong, positive latitudinal electron-density gradient (electron density increases with increasing latitude across the wall). Rays which are incident at more direct angles to the poleward wall (rays 1-3 in Figure 5) may experience a slight deviation to the right as they pass through the wall. This slight deviation results from Snell's law, though for a horizontal rather than vertical electron-density gradient. The deviation is minimal, because the strong latitudinal gradients are not maintained for a long distance across the

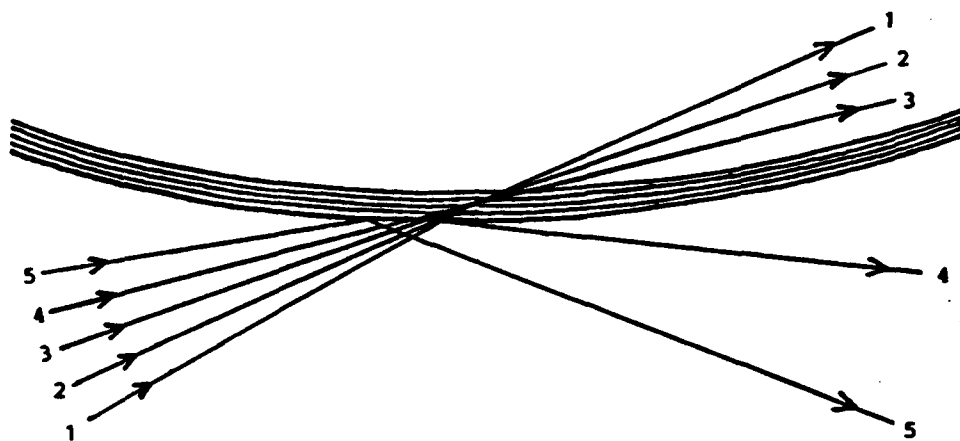


Fig. 5. The effects of strong horizontal electron-density gradients from the trough poleward wall on radio-wave propagation. Rays 1-3 experience a slight deviation as they refract through the wall. Rays 4-5 are within the critical angle, so they skip-off the trough wall and undergo total internal reflection.

ray path.

However, rays which are obliquely-incident on the strong trough-wall latitudinal gradient (rays 4 and 5 in Figure 5) beyond a critical angle deviate sharply without penetrating the trough wall. Such rays are said to skip-off the trough wall and undergo a total internal reflection (K. Baker, private communication, 1991). This situation is analogous to a stone which strikes the water's surface at an oblique angle, causing it to skip-off without penetrating the water's surface. The conditions which lead to a total internal reflection occur within a narrow range of incidence angles to a strong horizontal electron-density gradient, such as in a steep trough wall, or at the terminator. *Buchau et al.* [1973] and *Helms and Thompson* [1973] have investigated this phenomena and found azimuthal deviations as large as 200-400 km from the ray's intended landing point.

As shown by *Davies* [1969] in Figure 6, an enhanced E region acts to extend the ray's ground range for a given elevation angle and frequency. This effect is due to the changing vertical electron-density gradient within the E region, with respect to the vertical gradient that would exist in the absence of the E region. As the ray enters the E region below the peak E-region density (f_oE), the vertical gradient points upward (positive), and the ray refracts slightly toward the ground (away from the direction of the gradient). If f_oE is high enough, the ray will refract towards the surface, reaching apogee in the E region (below f_oE).

However, as shown in Figure 6, if the ray is able to penetrate beyond f_oE , the vertical electron-density gradient points downward (negative) as the electron density decreased between the E and F regions; the ray refracts back upwards.

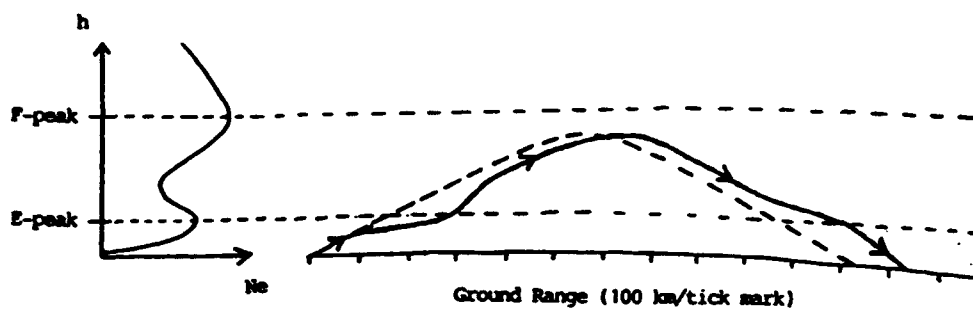


Fig. 6. The effects of an enhanced E region on radio-wave propagation. An enhanced E region extends the ray's ground range, due to changing vertical electron-density gradients within the E region. Below the E-peak, the vertical gradient is positive. Just above the E-peak, the vertical gradient is negative. Adapted from *Davies* [1969].

The same effect occurs on the ray's descent, except in reverse order. The net effect is to increase the ground range of the ray's landing point, since the ray was displaced away from the receiver during the ascent and descent through the E region.

Overview of the Mid-Latitude Trough

The mid-latitude (or main) trough is a region of the F-region ionosphere characterized by reduced plasma density. Trough plasma density is usually about five to ten times lower than that of the normal mid-latitude F region, but it can be as much as 100 times lower. A primary factor in formation of the nocturnal mid-latitude trough is the dominance of chemical loss processes in the absence of ionization sources in the nightside F region. However, theoretical modeling and experimental observations indicate the mid-latitude trough (trough) has no single cause [Schunk, 1983]. Instead, various chemical and transport processes compete to produce significant plasma-density depletions in the F region at a variable invariant-latitude range of 55-75° [Moffett and Quegan, 1983].

For the remainder of this chapter I will review large-scale trough morphology and briefly describe trough formation mechanisms. The predominant physical process contributing to trough formation involves competition of the effects of earth's rotation and the auroral electric field on high-latitude plasma convection. This competition causes regions of stagnated plasma flow (predominantly in the evening magnetic local time (MLT) sector), where trough plasma density decays to low values in the absence of ionization sources.

Trough Morphology

The trough is a significant depletion of electron density (or total ion density), usually in the nocturnal F region along a narrow latitudinal band varying between invariant latitudes of 55-75° [Moffett and Quegan, 1983]. It is not a static feature, due to the competition of dynamical, chemical, and transport trough-formation mechanisms. Since the trough is predominantly an F-region phenomenon, O^+ is typically the dominant trough ion, except in the light-ion trough (800-1500 km altitude). Figure 7 [Schunk, 1983] depicts the relative positions of the high-latitude plasma convection pattern, main trough, ionization hole, and the quiet-time auroral oval. Features to note are: 1) anti-sunward plasma convection across the polar cap, with return sunward flow at lower latitudes, 2) a two-cell convection pattern, resulting from competition of the high-latitude plasma convection pattern with corotating plasma, 3) corotational plasma convection at 55° invariant latitude, 4) auroral oval, positioned farther poleward on the dayside, and 5) main trough extending from 1600-0600 MLT, equatorward of the oval.

Figure 8 [Moffett and Quegan, 1983] shows the maximum electron density (obtained from satellite beacon transmissions), plotted as functions of local time (LT) and invariant latitude for winter and summer over Millstone Hill, Massachusetts. The trough shows clearly as a depletion in electron density during the nocturnal hours (2100-0600 LT) near 60-65° invariant latitude. The trough moved equatorward through the night, and though still evident in the summer, was

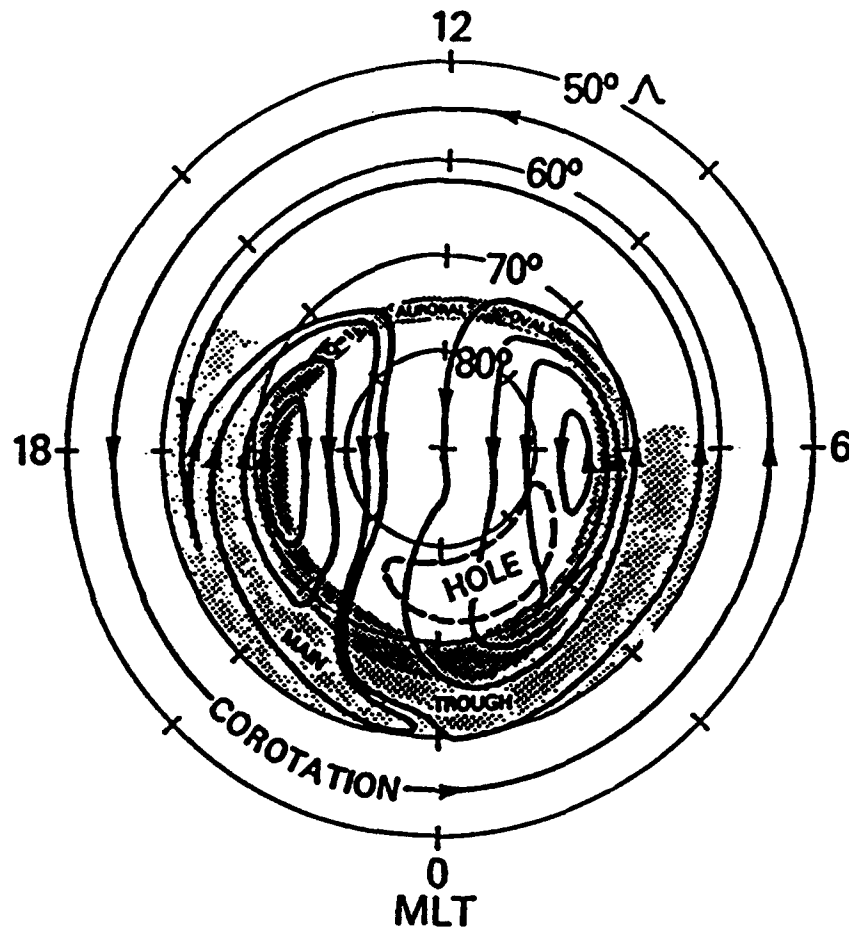


Fig. 7. Relative positions of the high-latitude plasma convection pattern, main trough, ionization hole, and quiet-time auroral oval. From *Schunk* [1983].

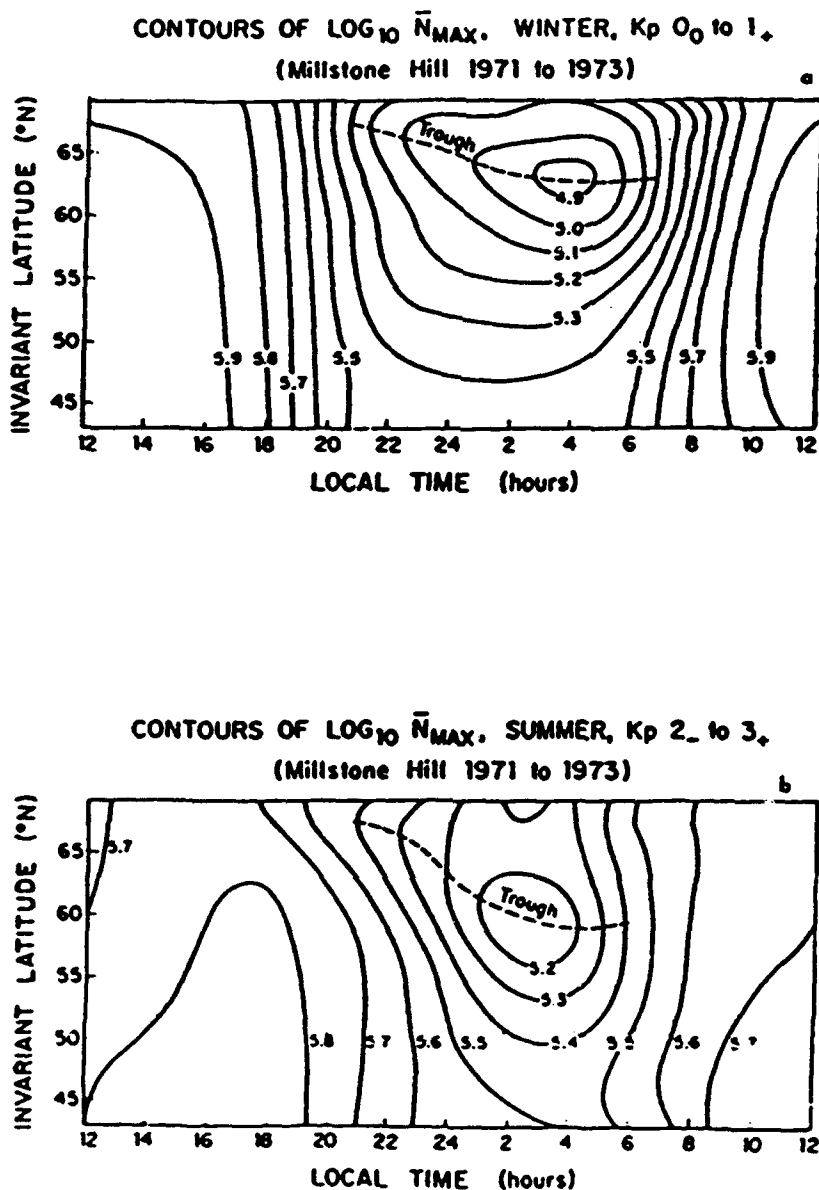


Fig. 8. Contour maps of average $\log_{10} N_m F_2$ (cm^{-3}) over Millstone Hill, Massachusetts plotted as functions of local time and invariant latitude for (a) winter, low magnetic activity, and (b) summer, medium magnetic activity. From Moffett and Quegan [1983].

deeper in the winter.

The auroral oval, just poleward of the trough, expands and moves equatorward during magnetic storms and substorms. The auroral oval effectively pushes the trough equatorward during periods of enhanced magnetic activity and pulls the trough poleward as it retracts after storms. The trough moves equatorward (about two degrees of latitude per unit Kp) for increasing geomagnetic activity [*Moffett and Quegan, 1983*].

Figure 9 [*Spiro et al., 1978*] shows Atmosphere Explorer-C (AE-C) satellite measurements of horizontal ion-drift velocity components and total ion concentration (at 250 km) in the evening MLT sector of the northern hemisphere. This figure depicts the vital role the high-latitude plasma convection pattern plays in trough formation in the evening sector. The component of earth's corotation velocity is shown as the dashed line on the velocity plots. *Spiro et al. [1978]* identified four characteristic regions from Figure 9. In region A (equatorward of the trough), the F-region plasma corotated eastward; ion concentration was relatively constant. In region B (the equatorward wall of the trough), the ion-drift velocity started to differ from corotation (slowed in speed and turned westward); ion concentration started to decrease. In region C (the base of the trough, about 2000 MLT), the ion-drift velocity switched to westward and increased in speed. Ion concentration reached a minimum just equatorward of the base of the steep poleward wall. The ion velocity peaked at the poleward edge of the trough. In region D (the auroral oval), the ion-drift velocity decreased. Ion concentration

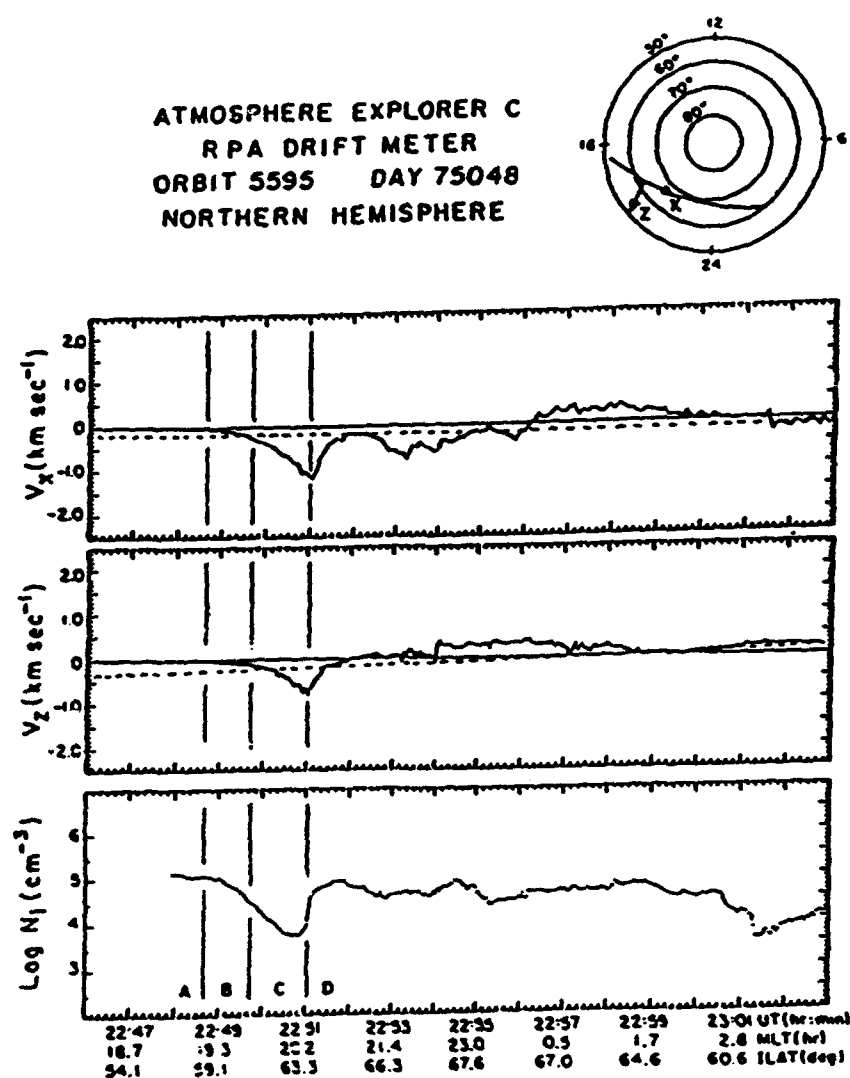


Fig. 9. Atmospheric Explorer-C satellite measurements of horizontal ion-drift velocity components and total-ion concentration at 250 km altitude in the evening MLT sector. The satellite track and orientation of the drift-measurement axes are shown. The component of earth's corotation velocity is shown as the dashed line on the velocity plots. From *Spiro et al.* [1978].

increased rapidly between the trough-minimum density region and the auroral oval.

Spiro et al. [1978] observed from data in Figure 9 (and similar data) that slow eastward ion drift predominates in the equatorward portion of the evening trough, while rapid poleward ion drift is often observed in the poleward portion (sometimes exceeding 2.5 km/s). Also, the ion concentration decreases smoothly across the transition region (stagnation line), where the plasma flow slows down and reverses. This flow stagnation region will be further addressed in the subsequent section regarding trough-formation mechanisms.

These seven trough features are generally well agreed upon by researchers [*Moffett and Quegan*, 1983]. 1) The trough usually occurs in the nocturnal ionosphere in a band stretching from the evening-morning MLT sectors. Though troughs are most often observed when the solar zenith angle exceeds 90°, similar plasma density depletions have been observed in the day sector, usually in the pre-dusk and post-dawn sectors [*Whalen*, 1989]. 2) The trough is more pronounced and most commonly observed in the winter and equinox; summer occurrences are less evident and limited to 1900-0300 MLT. 3) The poleward wall of the trough is positioned just equatorward of the auroral oval and is often very steep. As reported by *Schunk et al.* [1976], the poleward wall is usually relatively narrow (two to four degrees of latitude wide), reflecting the abrupt increase in electron density associated with the auroral ionization. 4) The trough moves equatorward through the night (from dusk to dawn MLT). The trough may shift poleward in

the morning sector during quiet magnetic periods. 5) The trough moves equatorward during periods of strong magnetic activity. 6) In the morning sector, the observed trough shapes are more variable than those observed before midnight. Typically, both latitudinal walls are more gradual and complex in structure. Also, ion-drift velocities do not differ much from rotation, and strong shears are usually absent. 7) Trough formation and behavior is not directly dependent on the 11-year solar cycle.

Other trough features which are less important or not well understood include the following statements. 1) The trough is observed to extend into the topside ionosphere (roughly 1000 km) and at altitudes below the F peak [*Moffett and Quegan*, 1983]. In the topside ionosphere, the trough is a depletion of H^+ rather than O^+ and is termed the light-ion trough. 2) The trough's equatorward wall is usually wider (three to eight degrees of latitude, wider for low magnetic activity) and more gradual than the poleward wall [*Schunk et al.*, 1976]. 3) Trough width usually varies between four to five degrees of latitude [*Schunk et al.*, 1976], though it can be as much as ten degrees wide. Trough width has been observed to vary with local time (LT) and Kp. *Schunk et al.* [1976] reported the trough is usually narrow near midnight LT and wide near dawn and dusk. Also, trough width tends to decrease as Kp increases. 4) Trough depth varies widely with LT and Kp. Commonly, electron concentrations are a factor of about five to ten times lower than those on either latitudinal side [*Schunk et al.*, 1976]. 5) The trough is deepest near midnight LT, where electron concentration is often a factor

of eight to ten times lower than on either side. 6) In the early-morning sector, the trough is shallower, and both walls become more gradual. 7) Trough depth increases with increasing magnetic activity. 8) Deep troughs are usually narrow, while shallow troughs are usually wide.

High-Latitude Plasma Flow Effects on Trough Formation

According to *Schunk et al.* [1976], the absence of photoionization sources combined with normal F-region recombination (decay) rates is an important factor in trough formation. This fact is evident when examining why the trough is predominantly a nocturnal phenomenon; plasma concentration decreases when a source of ionization is lacking over a prolonged period in the presence of normal decay rates. Concentration can decrease by an order of magnitude or more when plasma becomes stagnated (slow drift rates) in the nocturnal F region.

Spiro et al. [1978] investigated the role of high-latitude plasma convection in trough formation by proposing the formation of a stagnation line in the evening sector (Figure 10), which marks the transition between slow eastward flow (equatorward of the line) and faster westward flow (poleward of the line). The left panel in Figure 11 [*Spiro et al.*, 1978] shows a closer view of Spiro's stagnation-line model. Plasma flow is reduced for a three-degree wide latitudinal band at and equatorward of the line. The plasma flux tubes (starting at dusk at about 55-58° magnetic latitude) drift slowly eastward into the evening sector as they corotate with mid-latitude plasma.

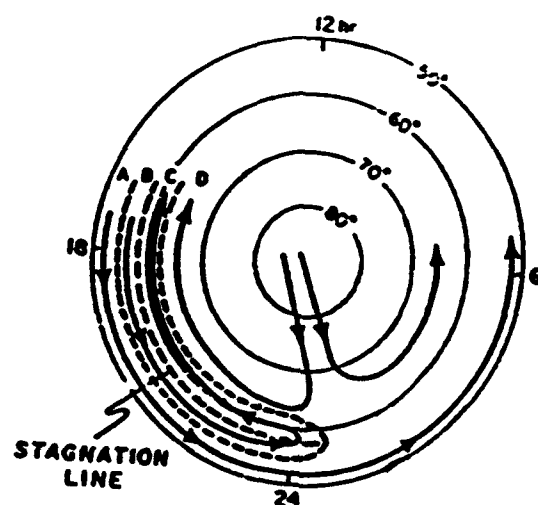


Fig. 10. Depiction of the stagnation line in the plasma convection pattern of the evening sector in a non-rotating coordinate system. The line marks the transition between slow eastward flow (equatorward of the line) and faster westward flow (poleward of the line). From *Spiro et al.* [1978].

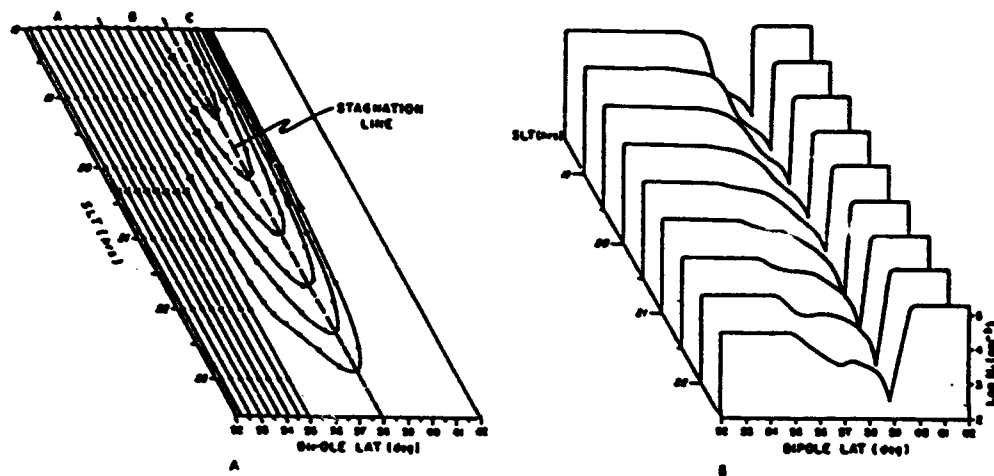
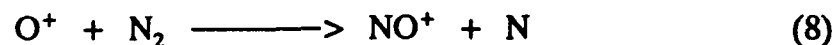


Fig. 11. (a) Mid-latitude plasma convection trajectories in the *Spiro et al.* [1978] stagnation line model, plotted in dipole latitude and solar local time (SLT) coordinates. The interval between successive dots along a trajectory indicates the passage of one hour. (b) Model ion-density (N_i) profiles associated with the convection trajectories of (a). From *Spiro et al.* [1978].

In the trough, the plasma drifts toward midnight and begins to slow down and reverse to westward flow at higher latitudes as it passes across the stagnation line. Due to the lack of photoionization sources combined with normal F-region decay rates over the longer period for the flow to stagnate and reverse, the electron density is greatly diminished in the evening sector (as low as 10^3 cm^{-3} near midnight) along a latitudinal band about one degree of latitude poleward of the stagnation line (right panel of Figure 11). *Collis and Haggstrom* [1988] have since confirmed the Spiro et al. model by reporting four cases of troughs (measured via incoherent scatter radar) positioned in a region of strongly convecting plasma about two degrees of latitude poleward of the stagnation line. The plasma had been depleted on the slow trip across the stagnation line.

An additional process (investigated by *Schunk et al.* [1976]) influences trough development to a lesser (or less understood) degree. This process is the depletion of the O^+ constituent of ionospheric plasma resulting from rapid ion-drift velocities associated with strong high-latitude (auroral) electric fields. Frictional interaction between the rapidly-moving ions and the neutral molecules causes increased Joule heating in the auroral region. The temperature increase acts to increase the rate of the ion-interchange reaction:



The resulting increase in NO^+ concentration decreases electron density because NO^+ has a stronger affinity for electrons than does O^+ .

The degree to which the various processes contribute to trough formation depends on a complex set of conditions, including degree of magnetic activity, presence of ionization sources, auroral electric field strength, high-latitude plasma convection rates, season, location (MLT and invariant latitude), neutral winds, and diffusion rates (vertical and horizontal). But, as *Schunk et al.* [1976] emphasized, trough behavior is most dependent on the rate of high-latitude plasma convection in the absence of photoionization sources and the O^+ loss rate associated with strong auroral electric fields.

CHAPTER III

IONOSPHERIC MEASUREMENTS

Overview

During early March 1989, scientists from the Geophysics Laboratory (GL) at Hanscom Air Force Base, Massachusetts conducted a coordinated OTH-B radar/airborne ionospheric measurement campaign to determine OTH-B radar performance while transmitting through the complex electron-density gradient structure of the trough. The East Coast Radar System (ECRS), the OTH-B radar at Bangor, Maine, attempted to detect the Airborne Ionospheric Observatory (AIO) as it flew repeatedly through the night-time trough from both equatorward and poleward approaches. On three occasions, the AIO flew from Goose Bay, Labrador to the region south of Greenland (Figure 12). During the three experimental periods (seven to eight hours each), the AIO remained in the OTH-B radar coverage area at a ground range of approximately 800-1400 nautical miles to provide a target with a precisely known location for the radar to illuminate. The AIO maintained a heading of about 45° with respect to the radar beams (J. Buchau, private communication, 1990).

A digisonde (digital ionosonde) aboard the AIO took vertical-incidence trough measurements every three to five minutes during the flights, from which f_oF_2 values were derived. Figure 13 shows the aircraft track in corrected geomagnetic coordinates, located in between two ground-based digisondes (Goose

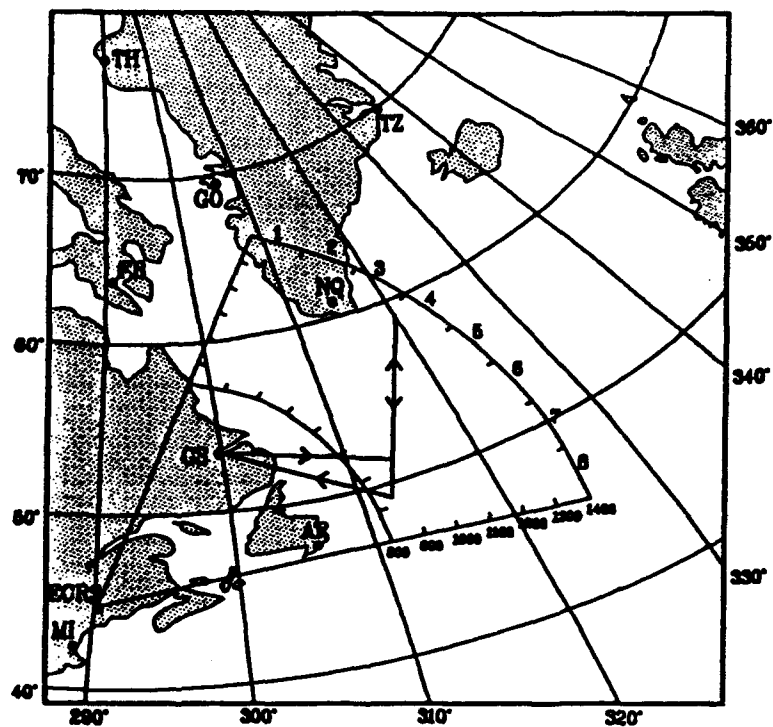


Fig. 12. Location of the GL aircraft track with respect to the coverage area of the East Coast Radar System (ECRS). Also shown are digisonde locations Goose Bay (GS), Argentina (AR), and Narssarssuaq (NQ).

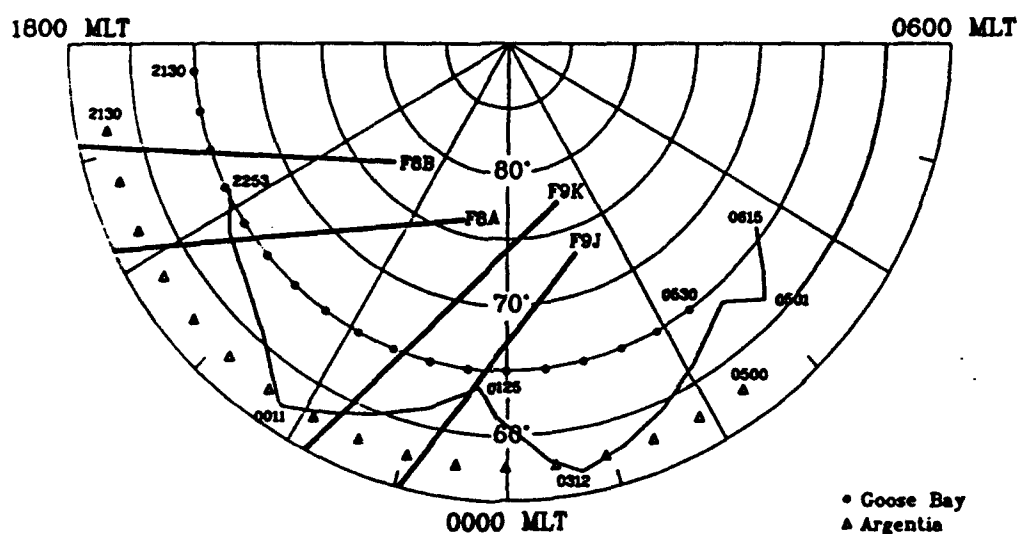


Fig. 13. Location of the GL aircraft track, Goose Bay (65° CGLAT), Argentina (58° CGLAT), and DMSP F8 and F9 satellite passes in corrected geomagnetic coordinates.

Bay (GB) and Argentia (AR), Newfoundland). Figure 12 shows the ground-based digisonde locations with respect to the aircraft track in geographic coordinates. At night, the trough is generally located within the latitudinal band between the two digisonde stations. The F8 and F9 Defense Meteorological Satellite Program (DMSF) trajectories that were over the experimental area during the time of the experiment are also shown on Figure 13. The ground-based digisondes took measurements every five minutes from about 2130-0530 Universal Time (UT), providing f_oF_2 values throughout the experimental periods, (except during periods of enhanced absorption effects, E-region blanketing and spread-F). Ground-based digisondes have a larger antenna surface area than the airborne digisonde, giving them a higher signal-to-noise ratio, better sensitivity, and higher resolution.

Description of Geophysical Conditions

I used three-hourly planetary magnetic index (Kp index) and daily 10.7-cm solar flux to indicate the level of geomagnetic and solar activity, respectively, during the three experimental periods. Fortunately, the IMP-8 (Interplanetary Monitoring Platform) satellite was positioned in the solar wind to measure the interplanetary magnetic field (IMF) during the three periods. The IMF conditions helped to roughly indicate the degree of magnetic reconnection and energy coupling between the solar wind and magnetosphere, providing a connection between the solar and geomagnetic activity for the periods of the GL experiment.

The GL scientists flew the AIO for the following three experimental periods:

Period 1: 2 March/2147 UT - 3 March/0457 UT, 1989
Period 2: 6 March/2253 UT - 7 March/0657 UT, 1989
Period 3: 7 March/2200 UT - 8 March/0610 UT, 1989

Refer to Table 1 for a summary of the geophysical conditions during the three experimental periods. Table 1 also depicts the actual geophysical conditions I used to determine the appropriate input conditions for the TDIM model output (addressed in Chapter IV).

The 11-year solar cycle was approaching solar maximum in March 1989. The 10.7-cm solar flux values during 2-8 March generally reflected this trend. For each period, I averaged the 10.7-cm solar flux values for the two days prior to and the day of the experiment (3-day solar flux averages in Table 1). To put the 3-day solar flux averages into proper context, I also averaged the 10.7-cm solar flux values for the interval 30 days before and 30 days after the experiment periods, obtaining 60-day averages centered around the periods (listed in Table 1). The 60-day averages (centered in early March) include about two solar rotation cycles (the solar flux peaks near 10 February and 14 March, as shown in Figure 14). The periods fell between the two peaks, on the early approach to the mid-March peak. As expected, the 3-day solar flux averages for the three experiment periods (170.5, 191.6, 198.0) were below the 60-day average (near 210).

Figure 15 is a plot of the 3-hour Kp index values from 2-8 March 1989. Geomagnetic activity was generally weak to moderate, as evidenced in Table 1 by

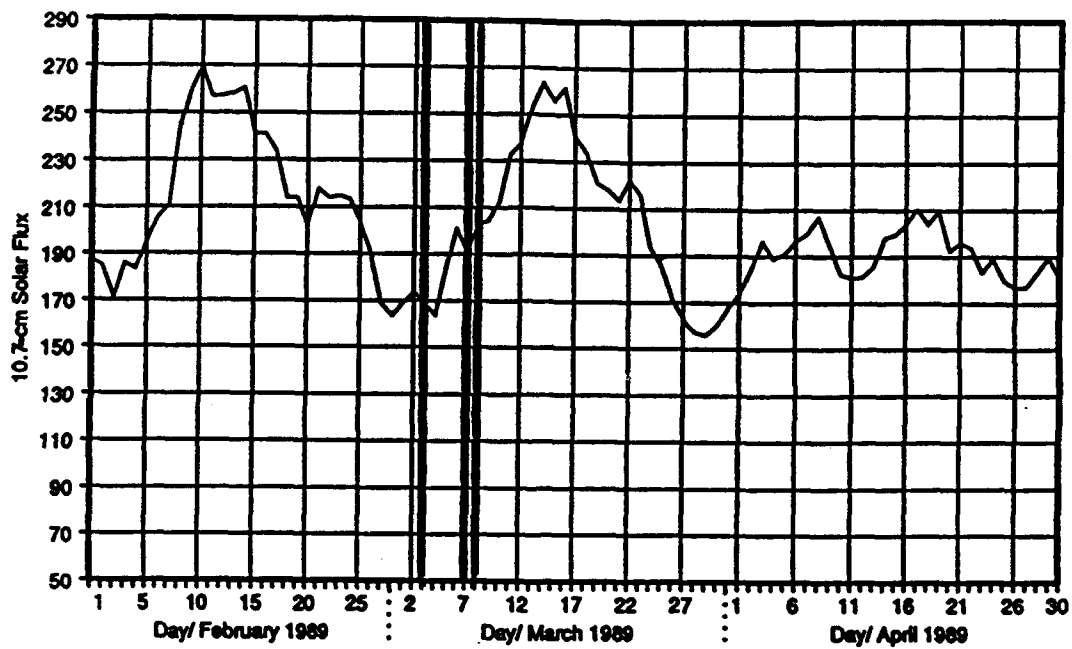


Fig. 14. 10.7-cm solar flux values from February to April 1989. Units are 10^{-22} Webers $\text{m}^{-2} \text{Hz}^{-1}$. The three GL experimental periods are shaded.

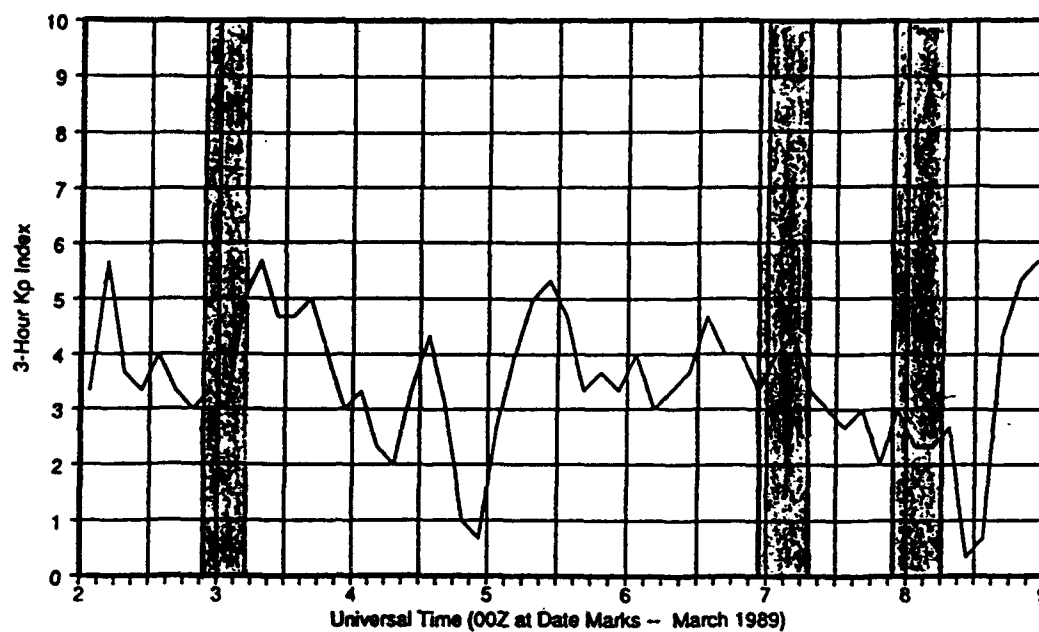


Fig. 15. 3-Hour Kp index values from 2-8 March 1989. The three GL experimental periods are shaded.

the 3-hour Kp values, ranging from 2.0-5.0 and averaging 3.6, 4.0, and 2.4 for the three periods, respectively. For each period, I averaged the 3-hour Kp values for a 12-hour period. This average included the geomagnetic-activity level approximately four to six hours before the periods to account for the recent geomagnetic history of the ionosphere.

There were clear differences between the three periods. The first two periods were the most disturbed. During the first period, a moderate substorm occurred towards the end of the experiment, as shown by a rise in Kp index from 3.0 to 5.0 between 3 March/0000-0600 UT. The Kp index was more steady prior to and during the second period, ranging between 3.3-4.3. The third period was clearly the least disturbed; the Kp index ranged between 2.0-3.0 during the 12-hour period.

Figure 16 depicts the hourly averages of the B_y and B_z IMF components for 2-8 March 1989. I plotted the hourly averages of B_y and B_z in the geocentric solar magnetospheric (GSM) coordinate system, the most suitable reference frame to examine solar wind-magnetosphere interactions. A steady negative B_z indicates stronger energy coupling between the IMF and the geomagnetic field through magnetic reconnection. As a result, geomagnetic storms and substorms are more frequent and intense during periods of steady negative B_z . Additionally, the TDIM model output used to simulate the trough conditions during the GL experiment was for a negative B_z input condition.

To summarize the IMF conditions for the three periods, I calculated averages of the hourly averages of B_x , B_y , and B_z for the periods (including one

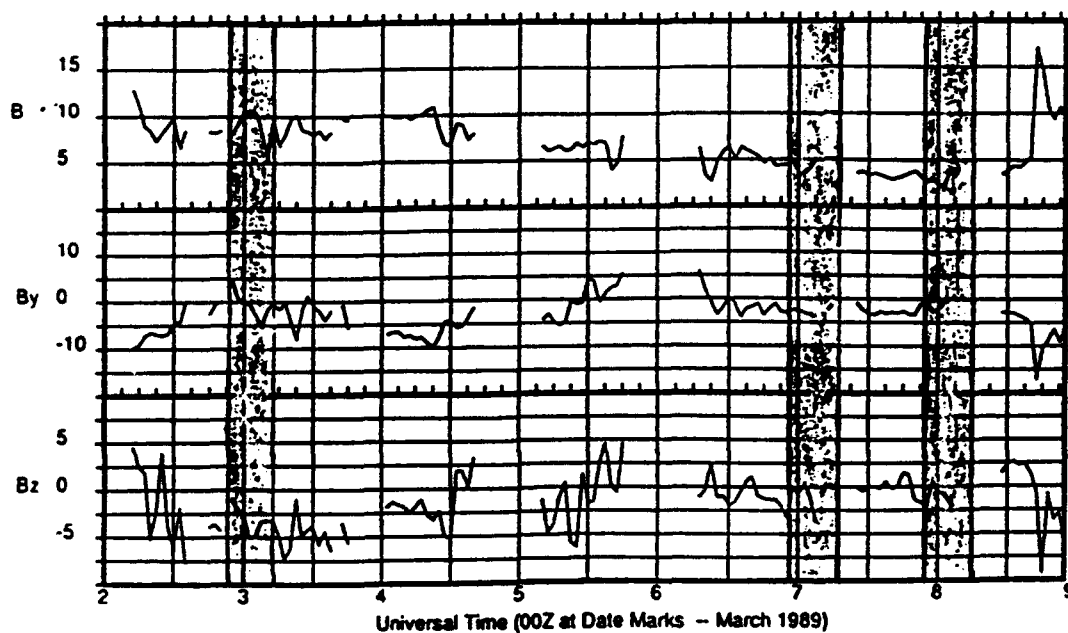


Fig. 16. Hourly averages of the magnitude of the average field vector of the IMF (B), and the B_y and B_z IMF components (in geocentric solar magnetospheric coordinates) from the IMP-8 satellite. Units are nano-teslas. The three GL experimental periods are shaded.

hour prior to), as shown in Table 1. The averages of the hourly averages of B_y and B_z were negative over the time interval for all three periods, though both B_y and B_z often turned briefly positive. The only clear exception to this was during the first period, when B_z was negative throughout the entire period and ranged from -1.0 to -5.0 nT (nano-Teslas). In Table 1, I recorded the percentage of 5-minute averages of B_y and B_z that were negative for the three periods (including the hour prior). The percentages of negative 5-minute average B_y and B_z components were 60% or more for all three periods. For period one, 98% of the 5-minute averages of B_z were negative, while 100% of the 5-minute averages of B_y were negative for period two, indicating highly stable B_z and B_y components for experimental periods one and two, respectively.

Overview of Electron-Density Measurements

I used three types of ionospheric measurements to examine the nightside trough electron-density structure and its associated horizontal gradients: 1) airborne and ground-based digisonde f_oF_2 values, 2) Defense Meteorological Satellite Program (DMSP) in-situ measurements of electron density, and 3) Millstone Hill incoherent scatter radar (ISR) electron-density measurements. The digisondes at Goose Bay and Argentia took measurements every five minutes, and the AIO digisonde took measurements every three to five minutes along the AIO track. With Equation (3), I converted digisonde f_oF_2 values to F_2 peak electron densities (N_mF_2), which were representative of ionospheric conditions roughly 200 km or less above the altitude of radio-wave refraction, depending on the depth the ray penetrated the

ionosphere.

I used digisonde electron-density measurements to represent trough structure for two reasons. First, digisonde measurements are usually available hourly from several stations in the trough region. Data from several (two or more) strategically positioned stations can provide the user with key electron-density measurements to construct a realistic trough depiction, or to update an electron-density model with actual f_oF_2 measurements. Second, the user can access digisonde data in near-real time, within minutes of the actual measurements. These two advantages are not provided by a more sophisticated data source, such as an incoherent scatter radar.

The digisonde electron-density measurements served three main purposes in this study. Their initial role was to accurately represent the actual trough electron-density conditions during the three experimental periods, which are displayed and discussed in this chapter. They also provided the basis for comparison with the TDIM model output for the corresponding geophysical conditions, enabling me to examine the model's ability to simulate the trough's electron-density structure. The most significant role of the digisonde measurements was to provide representative electron-density values and horizontal gradients from actual trough measurements. These would be incorporated into the TDIM model output for use in ray-tracing simulations. Even if the digisonde measurements did not provide a highly accurate representation of the trough for the specific experimental periods, they will have served their primary purpose in this study if they provided realistic trough electron-density values and horizontal gradients for use in ray tracing.

As shown by Figure 13, temporal resolution provided by the digisonde stations was good in the longitudinal direction at Goose Bay and Argentia latitudes. Longitudinal temporal resolution at latitudes between Goose Bay and Argentia was sporadic, due to its dependence on the aircraft's location. Latitudinal spatial resolution was also poor, since it was based on an interpretation from only three reporting stations within about seven degrees of latitude. However, DMSP satellites passed over the GL experiment area three to four times per study period (Figure 13) and measured the in-situ electron density every second along the orbital path (about 868 km altitude at the evening trough latitude). Thus, the DMSP passes provided high-resolution latitudinal profiles along the orbital paths during the few minutes the satellites passed through the topside trough. The Millstone Hill ISR data depicted the latitudinal and longitudinal variation of $N_m F_2$ for the last two experimental periods. I used the ISR data to check the validity of the digisonde trough depictions.

Trough Conditions From Digisonde Measurements

In order to produce a trough representation from the digisonde measurements taken in the manner shown in Figure 13, I had to assume the trough remained a relatively stationary feature as the digisonde stations corotated underneath. Based on this assumption, as the stations passed under the trough, the gradient changes they experienced were not due to time-varying phenomena, such as substorms. Instead, they were measuring the spatial gradients which varied as

they moved into a different part of the trough.

To depict the trough from the evening to post-midnight magnetic local time sectors in this manner, I plotted the $N_m F_2$ values (converted from digisonde $f_o F_2$ values) for Goose Bay, Argentina, and the AIO on corrected geomagnetic (CGM) polar plots for the three experimental periods (Figure 17) and analyzed the density contours every $1.0 \times 10^5 \text{ cm}^{-3}$ ($10 \times 10^4 \text{ cm}^{-3}$). I chose this contour interval because of its relevance to trough electron densities; trough-minimum $N_m F_2$ is commonly below 10^5 cm^{-3} . The statistical positions of the auroral oval are shown for the respective Q-index values during the three periods. The Q index is used to determine the latitudinal position of the auroral oval for various geomagnetic-activity levels, as measured by the Kp index. I used polar projection plots which transform between geographic and corrected geomagnetic coordinates (J. Buchau, private communication, 1990) to convert geographic position at a specific universal time to corrected geomagnetic latitude (CGLAT) and local time (CGMLT).

The trough shifted to lower latitudes as it advanced in CGMLT through the night sector. Trough-minimum densities were $4.0\text{-}8.0 \times 10^4 \text{ cm}^{-3}$ during each period. For the last two experimental periods, I used infrequent digisonde $f_o F_2$ values from Narssarssuaq, Greenland (approximately 69° CGLAT) to provide data coverage poleward of Goose Bay (about 0230 CGMLT for the second period and around 2000-2200 and 0300-0500 CGMLT for the third period on Figure 17).

The Figure 17 plots are smooth interpretations of $N_m F_2$ values from digisonde measurements taken at two fixed ground locations about seven degrees of latitude

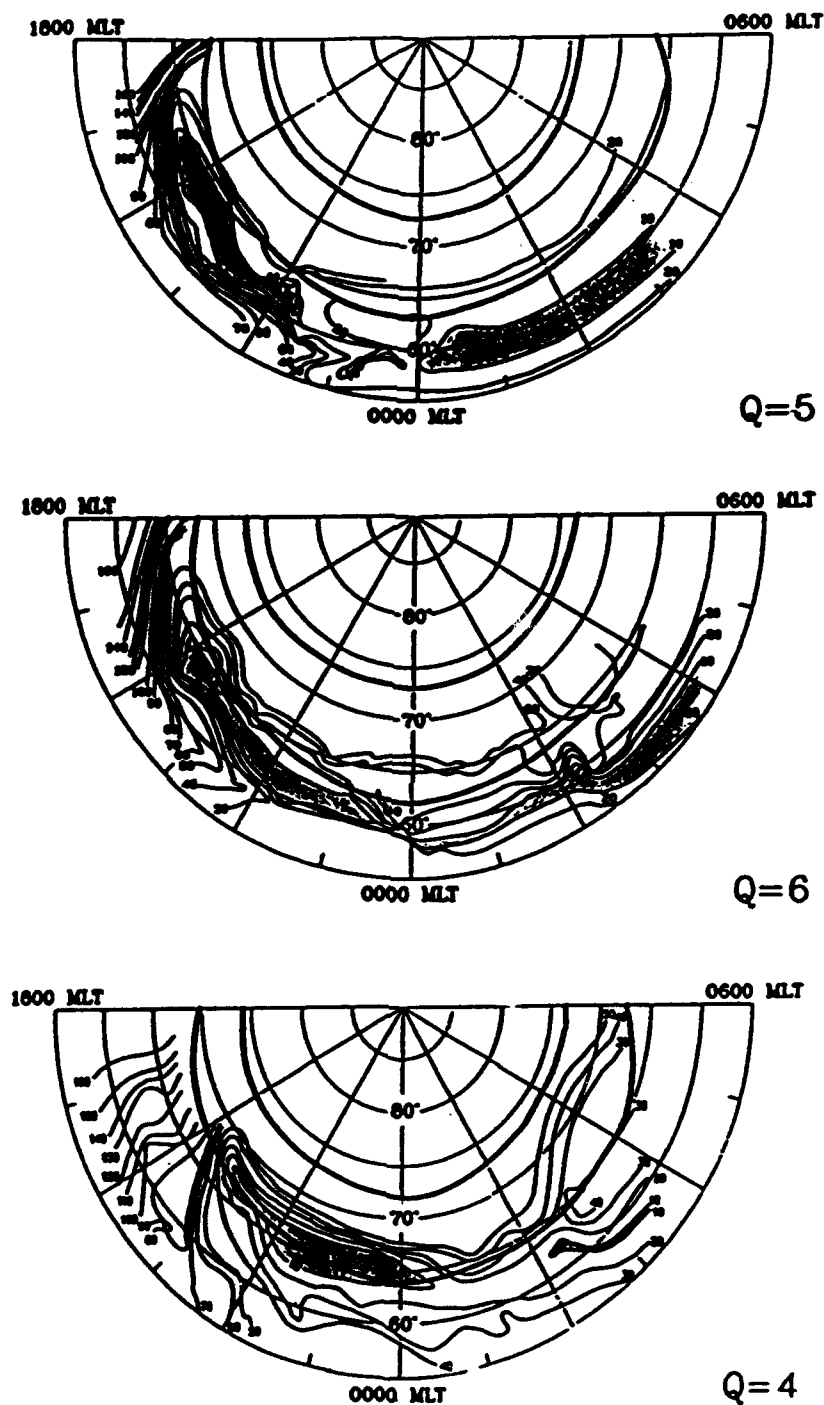


Fig. 17. Digisonde trough depictions for the three experimental periods, shown sequentially from top to bottom. $N_m F_2$ values calculated from digisonde $f_o F_2$ values were plotted for Goose Bay, Argentina, and the AIO in corrected geomagnetic coordinates. Electron density was analyzed in contours of $1.0 \times 10^5 \text{ cm}^{-3}$.

apart, with the AIO filling the gaps in-between only along its flight path (Figure 13). Data coverage was poor in some trough regions, especially between Goose Bay and Argentia away from the AIO track. During the third experimental period, digisonde f_oF_2 values were not available at Argentia after 2105 CGMLT. To fill this gap, I used automated ionosonde values every 30 minutes (instead of digisonde values every five minutes) from about 2130-0300 CGMLT for Argentia. Additionally, digisonde measurements were unavailable sporadically due to spread-F and E-region blanketing, which was particularly severe at Goose Bay in the morning sector. In the morning sector, much of the trough had shifted equatorward of Argentia, moving it out of the digisonde network used in this study. Since the data coverage was deficient in the morning sector, I performed the ray-tracing simulations (reported in Chapter V) in the evening sector.

The strongest horizontal electron-density gradients occurred near the evening terminator and the equatorward wall of the evening trough limb, following sunset at F-region altitudes. The trough poleward and equatorward walls often had steep gradients, especially in the early evening equatorward wall. The first two periods had the strongest equatorward-wall gradients (from about 60-65° CGLAT and 1800-2000 CGMLT on Figure 17). The equatorward-wall gradients during the third period were weaker and occurred higher in latitude (about 65-70° CGLAT) and later in the evening sector (2000-2100 CGMLT). The poleward-wall gradients were less certain, due to the data deficiency poleward of Goose Bay.

In the region between Goose Bay and Argentia, where the aircraft provided

data, I was sometimes able to analyze trough electron-density structure in more detail. For example, regions of slightly-enhanced electron density appeared near 60-65° CGLAT, roughly between 2300-0000 CGMLT during the first two periods and 0200-0300 CGMLT during the last two periods on Figure 17. Perhaps auroral precipitation contributed to the local electron density in the enhanced regions via precipitation-induced ionization or plasma-instability processes. The equatorward auroral boundaries from the F9 DMSP passes near 2300-0000 CGMLT penetrated to about 63-65° CGLAT during the first two periods, supporting this idea. A second possibility is that the enhanced regions are higher-density plasma patches which drifted across the polar cap into the midnight sector via the anti-sunward plasma convection channel [Buchau *et al.*, 1988].

Comparison of Digisonde and ISR Trough Depictions

To check the validity of the digisonde trough depictions of Figure 17, I replotted the $N_m F_2$ values from Millstone Hill incoherent scatter radar measurements (from Figure 5 in the Buonsanto *et al.* [1990] paper) in corrected geomagnetic coordinates for the last two periods (Figure 18), at the same scale as the digisonde depictions. The Millstone Hill ISR was not operational during the first period. Since I only plotted values every degree of CGLAT and every 30 minutes of CGMLT and contoured the data as for Figure 17, the resulting depictions are not as detailed as the original geodetic-UT figure. Some smaller-scale features were smoothed out by the reduction in resolution, and some inaccuracy was likely

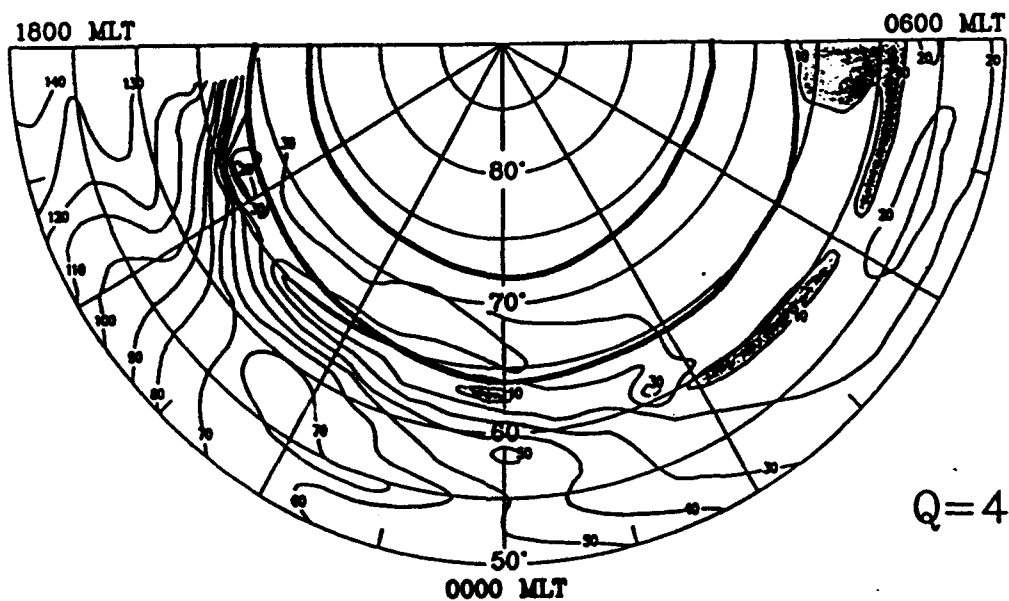
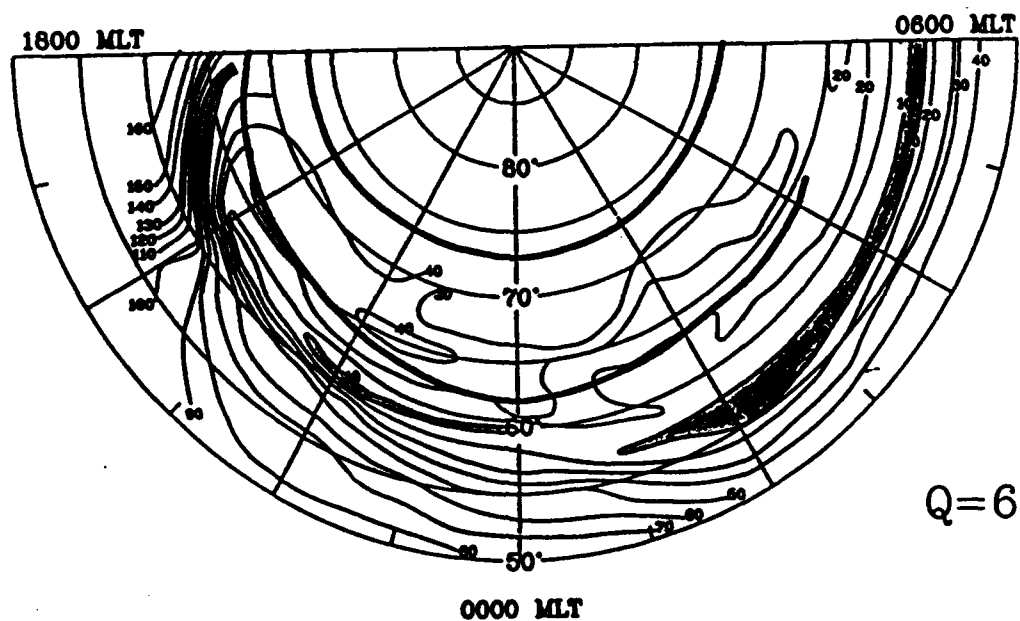


Fig. 18. Millstone Hill incoherent scatter radar depictions of the trough for the last two experimental periods, shown sequentially from top to bottom. $N_m F_2$ values were plotted in CGM coordinates. Transformed from *Buonsanto et al.* [1990].

introduced during the coordinate transformation. But the large-scale trough structure and horizontal electron-density gradients are still apparent. With these limitations in mind, and those of the digisonde depictions, I compared the digisonde and ISR depictions for the last two periods in terms of large-scale electron-density structure and horizontal gradients in the various trough sectors.

Upon examination of Figures 17 and 18, there were some clear differences in trough latitudinal location, depth, width, and latitudinal electron-density gradients. Overall, the locations of the trough-minimum electron densities agreed within about one to two degrees of latitude, though the ISR trough-minimum regions (below $1.0 \times 10^5 \text{ cm}^{-3}$) were about two to three degrees of latitude narrower. However, the ISR troughs were much wider after 0100-0200 CGMLT. The electron density was below $2.0 \times 10^5 \text{ cm}^{-3}$ over much of the morning sector on the ISR depictions, in sharp contrast to the elevated electron densities ($3.0\text{-}5.0 \times 10^5 \text{ cm}^{-3}$) poleward of the digisonde trough-minimum regions on Figure 17. Differences in trough shape, depth, and width between the ISR and digisonde depictions led to localized differences in the electron-density gradient.

Overall, the digisonde and ISR depictions generally agreed in latitudinal location of the trough-minimum electron densities, but smaller-scale trough structure was markedly different. The largest differences occurred in the morning sector. Large-scale agreement was fairly good in the early evening sector (before 2000 MLT), which is where the strongest horizontal gradients were located.

With the exception of the evening trough limb, the horizontal gradients of the

trough walls are strongest along a constant meridian. Thus, I plotted latitudinal electron-density profiles of the trough equatorward and poleward walls. However, judging gradients from a logarithmic plot can be deceiving; a profile that appears steep on the low end of one logarithmic interval (i.e., 5.0-5.2) may not be as steep as one that appears gradual on the high end (i.e., 5.7-5.9). To avoid this problem, I calculated the maximum latitudinal electron-density gradients (minimum gradient length of two degrees of latitude) of the equatorward and poleward trough walls every 30 minutes (where available) from 1830-0230 CGMLT for the digisonde (DIG) and ISR depictions. The equatorward- and poleward-wall latitudinal gradients are plotted against latitude in Figures 19 and 20, respectively.

The equatorward-wall gradients from Figure 19 were typically strongest in the early evening sector, generally between 1830-2030 CGMLT for both depictions. The digisonde and ISR depictions showed a similar dynamic range (roughly $0.5\text{-}2.5 \times 10^3 \text{ cm}^{-3} \text{ km}^{-1}$), but individual values were as much as a factor of three different at specific CGMLTs, though they usually agreed within a factor of two. Some of the disagreement was likely due to the poorer latitudinal resolution of the digisonde depictions.

The overall lack of agreement of the poleward walls on Figure 20 was due in part to the sparsity of digisonde data poleward of Goose Bay and the low resolution of the digisonde profiles relative to the ISR profiles. Most values range from $0.3\text{-}1.7 \times 10^3 \text{ cm}^{-3} \text{ km}^{-1}$, and no trend in CGMLT was apparent. The local peaks near 2100, 2300, and 0000 CGMLT may have been associated with discrete

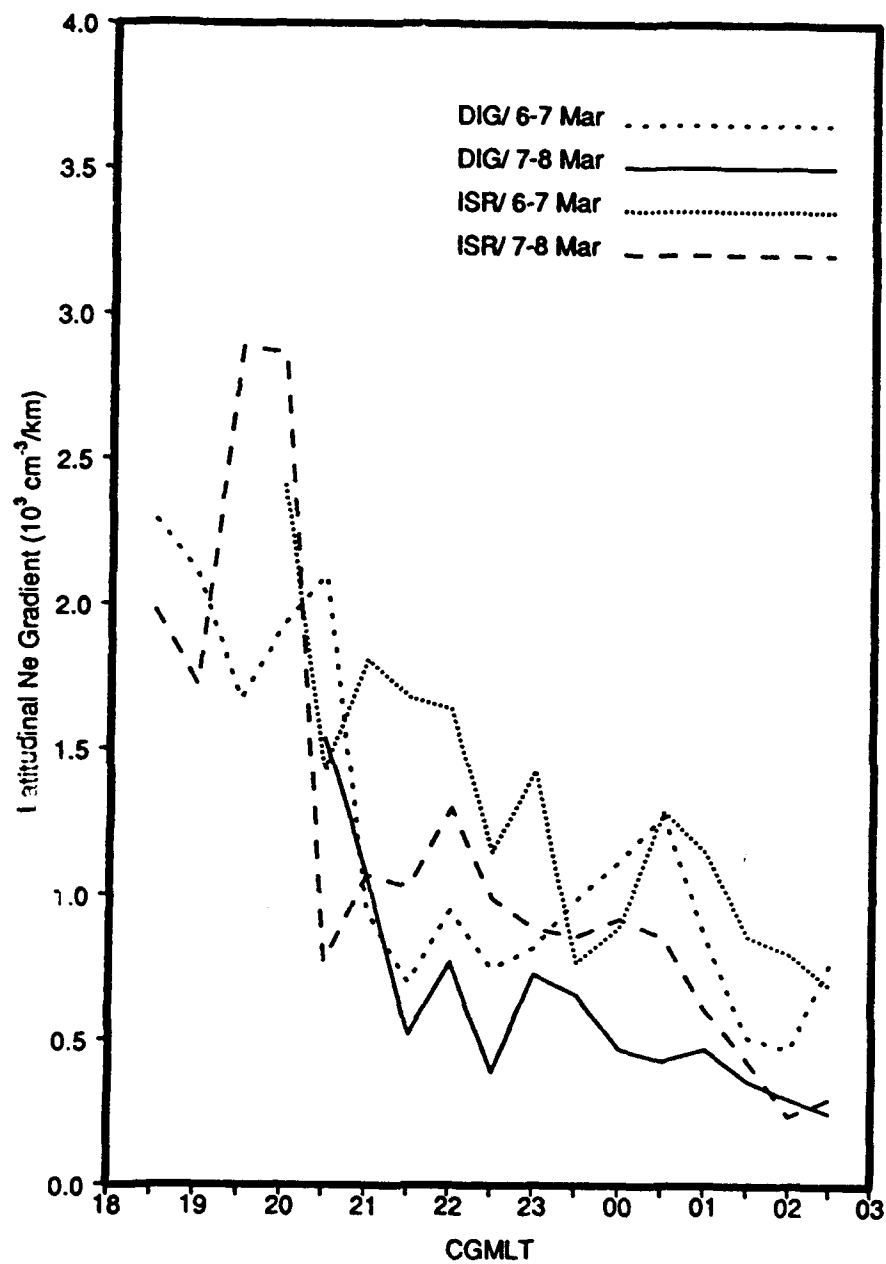


Fig. 19. Latitudinal $N_m F_2$ gradients of the equatorward wall calculated from the digisonde and incoherent scatter radar trough depictions (Figures 17 and 18). Values were plotted every 30 minutes of CGMLT.

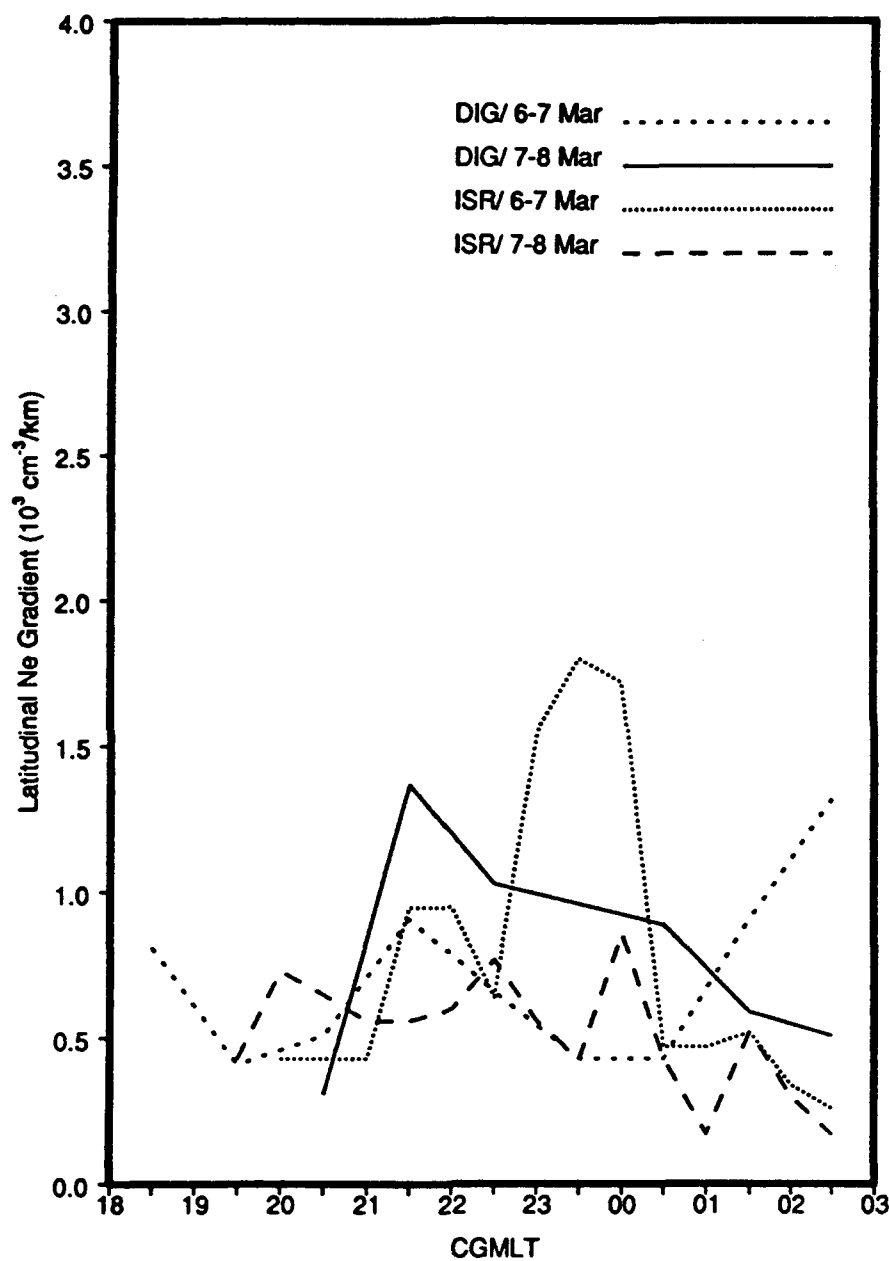


Fig. 20. Latitudinal $N_m F_2$ gradients of the poleward wall calculated from the digisonde and incoherent scatter radar trough depictions (Figures 17 and 18). Values were plotted every 30 minutes of CGMLT.

auroral activity. Though the digisonde and ISR gradients disagreed at specific CGMLTs, they fell into a similar range of values overall, indicating the digisonde latitudinal gradients in the trough walls were representative of actual values.

Figures 21 to 23 are latitudinal trough profiles from the digisonde N_mF_2 data interpretations (Figure 17). I plotted N_mF_2 every degree of latitude along constant meridians (every 30 minutes from 1830 to 0200 CGMLT), grouping the 16 latitudinal profiles into four CGMLT quadrants. The profiles clearly show the trough moved equatorward as the night progressed. Trough electron density was reduced by a factor of about three to ten of that on the equatorward and poleward edges of the trough. The troughs from the first two experimental periods (Figures 21 and 22) showed similar latitudinal variation with CGMLT, which is reasonable since the geomagnetic-activity level was similar for these two periods. These troughs first appeared between 1900-1930 CGMLT at about 64-66° CGLAT (Quadrant 1). They moved gradually equatorward, to be located at about 56-60° CGLAT in the morning sector (Quadrant 4). The corresponding DMSP electron-precipitation data and visual auroral imagery showed the auroral oval had also moved equatorward in the late evening-early morning sector. During the third period (Figure 23), the trough was located farther poleward than it was during the first two periods, as expected, since it was the quietest period geomagnetically. The trough appeared later (2030 CGMLT) at about 66-68° CGLAT. By the morning, the trough had only penetrated to approximately 59-65° CGLAT.

Figure 24 shows latitudinal trough profiles of N_mF_2 values from the

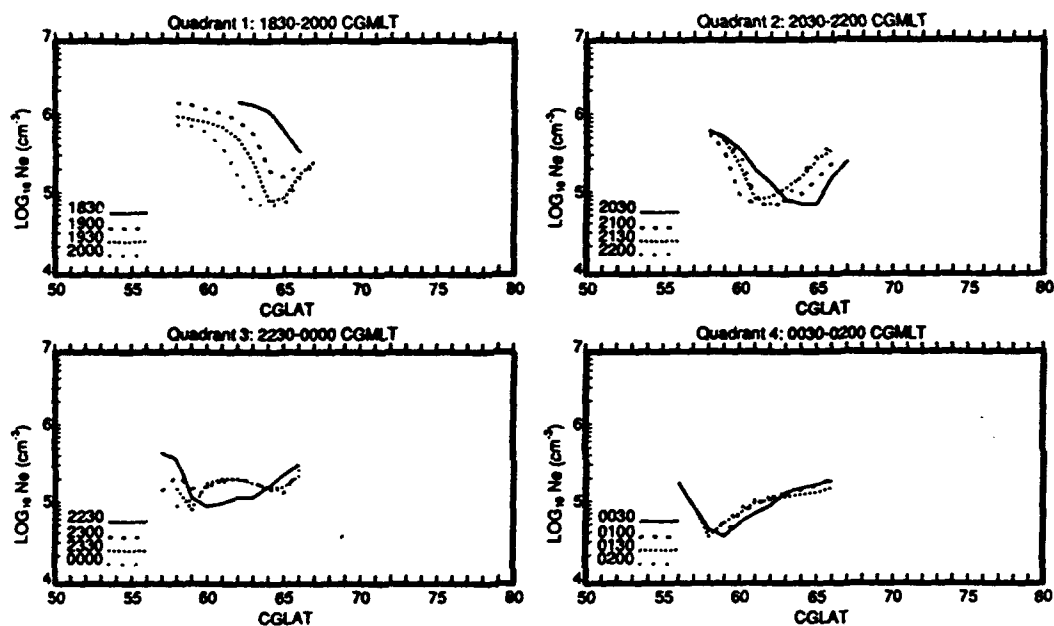


Fig. 21. Latitudinal trough profiles at 1830-0200 CGMLT, taken from the digisonde $N_m F_2$ trough depictions (Figure 17) for the first experimental period.

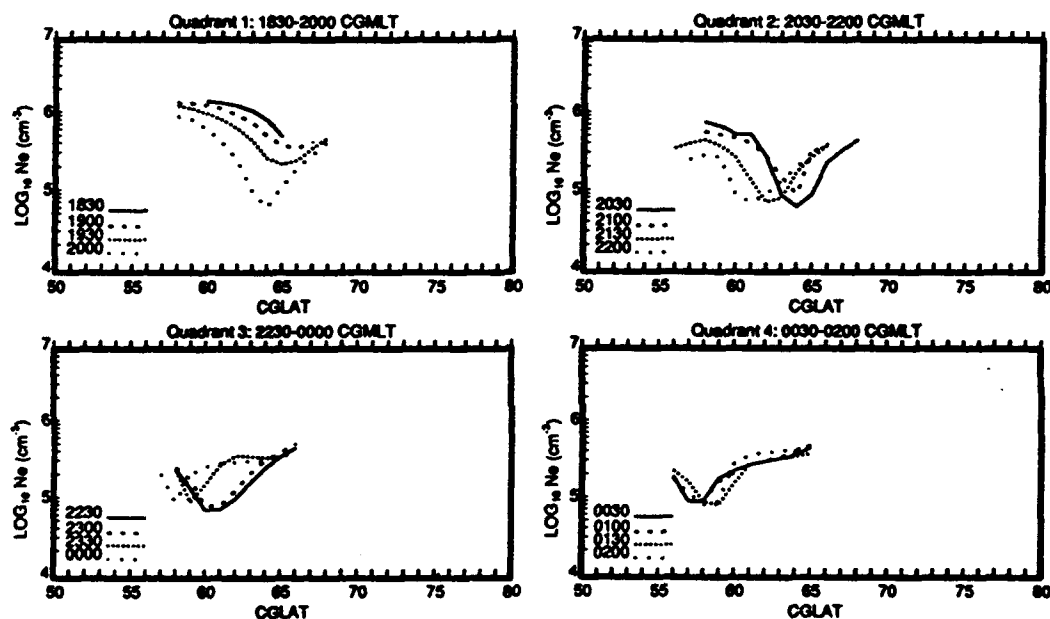


Fig. 22. Latitudinal trough profiles at 1830-0200 CGMLT, taken from the digisonde $N_m F_2$ trough depictions (Figure 17) for the second experimental period.

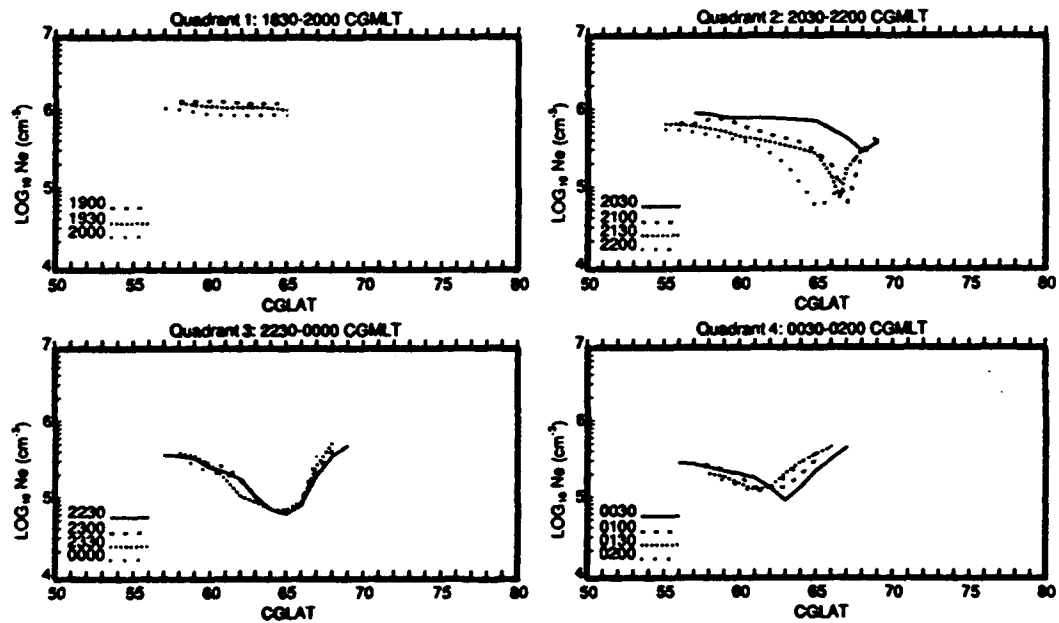


Fig. 23. Latitudinal trough profiles at 1830-0200 CGMLT, taken from the digisonde $N_m F_2$ trough depictions (Figure 17) for the third experimental period.

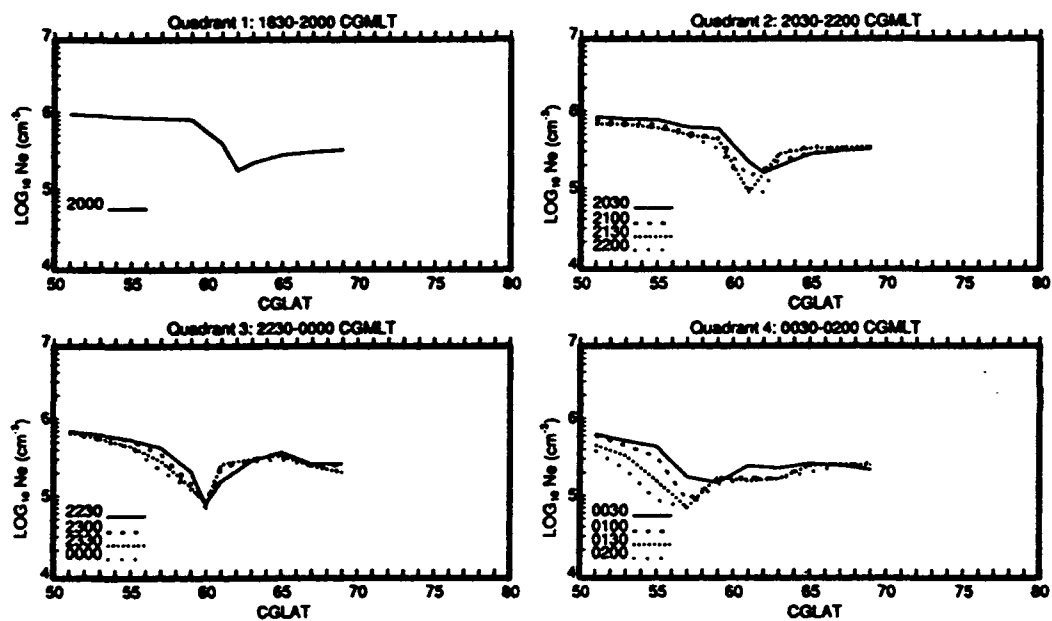


Fig. 24. Latitudinal trough profiles at 2000-0200 CGMLT, taken from the Millstone Hill incoherent scatter radar $N_m F_2$ trough depiction (Figure 18) for the second experimental period.

Millstone Hill ISR for the second experimental period. The ISR profiles and the corresponding digisonde profiles (Figure 22) usually agreed in trough depth. At the worst, the digisonde troughs were two to three times deeper. During the third period, the digisonde trough profiles were usually about two to four times deeper than the ISR trough profiles (not shown). With the exception of the morning sector, the digisonde trough profiles showed more variability with CGMLT, and were approximately two to three degrees of latitude wider than the corresponding ISR profiles. The digisonde trough profiles were usually about one to two degrees of latitude poleward of the corresponding ISR profiles.

The localized differences between the digisonde and ISR latitudinal electron-density profiles indicate the digisonde data did not provide an entirely accurate representation of trough conditions during the experimental periods. The ISR profiles were likely more representative of actual conditions, by virtue of their better spatial resolution. Placement of more digisonde stations at latitudes between Goose Bay and Argentia would have improved the resolution of the trough latitudinal profiles.

As stated earlier, the primary purpose of the digisonde latitudinal profiles in this study was to provide realistic trough depictions with representative horizontal electron-density gradients for use in the ray-tracing simulations. Both the digisonde and ISR trough depictions satisfied the conditions for realistic trough representations, as discussed in Chapter II. The latitudinal gradients from both depictions fell within a realistic range. The differences in detailed trough structure

did not reduce the validity of the study's main goal: to determine the effect of realistic trough electron-density values and gradients on ray propagation.

DMSP Latitudinal Electron-Density Profiles of the Trough

Figure 25 shows invariant latitude (INV LAT) trough profiles derived from in-situ electron-density measurements from DMSP F8 and F9 satellites at an orbital altitude of 868 km. The DMSP orbital paths are shown in Figure 13 in corrected geomagnetic coordinates. I plotted electron-density values every five seconds, including major inflection points in between. The steepest electron-density gradients from these latitudinal profiles were usually along the poleward trough wall or just equatorward of the trough minimum.

I compared the DMSP latitudinal trough profiles (Figure 25) with the digisonde latitudinal trough profiles in Figures 21 to 23. As stated earlier, the DMSP electron-density profiles had much finer spatial resolution than the digisonde N_mF_2 latitudinal profiles (though about 400-500 km higher in altitude), revealing not only the large-scale (> 100 km) electron-density structure, but also the smaller-scale density fluctuations (tens of km). However, spatial and temporal coverage from the DMSP measurements was poor, since each satellite only took measurements along its orbital path, which passed over the region of interest every 110 minutes. The digisonde N_mF_2 depictions had much better spatial and temporal coverage, since the three stations over a wide area provided data simultaneously every five minutes for six to seven hours.

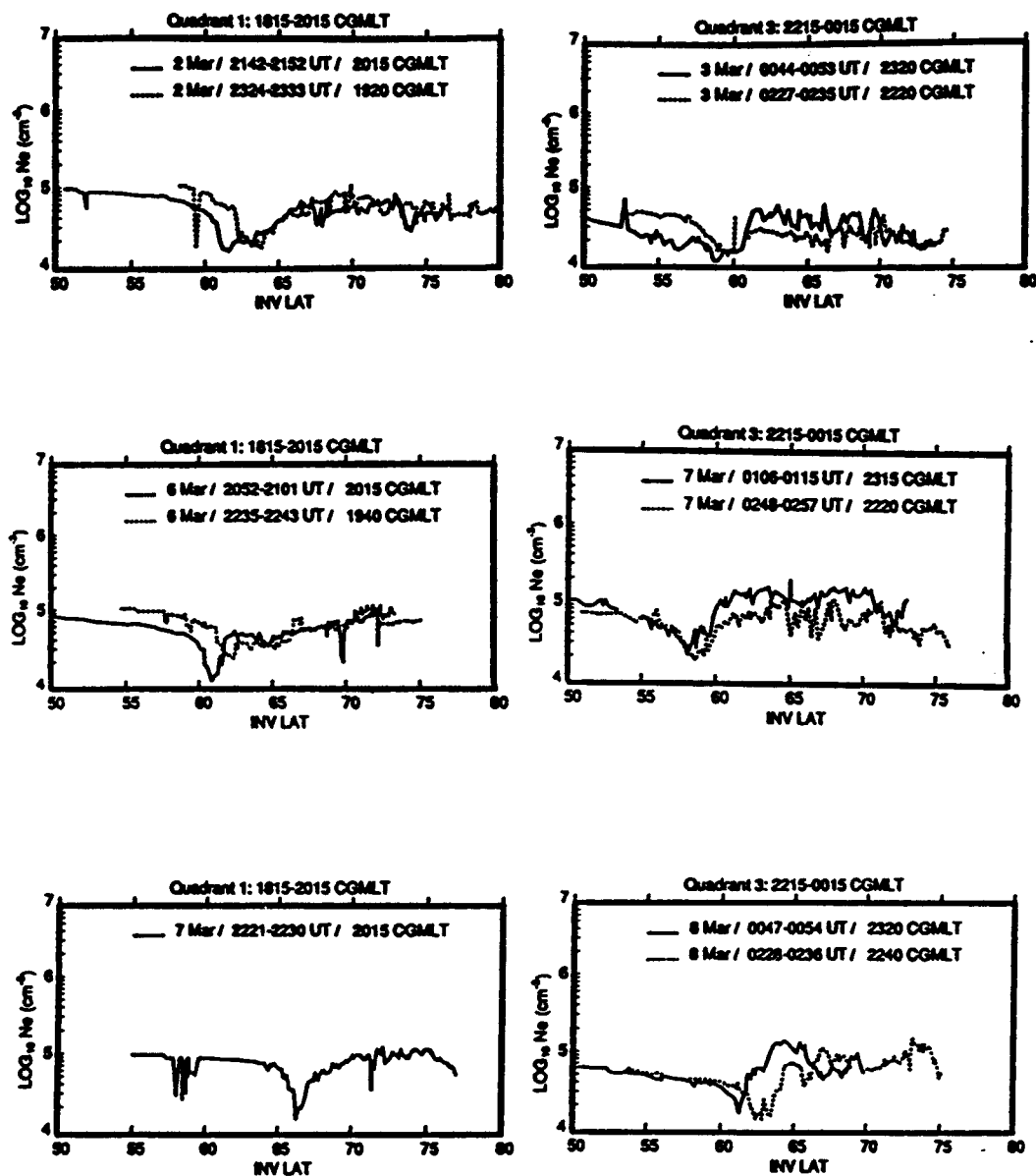


Fig. 25. Invariant latitude (INV LAT) trough profiles derived from DMSP electron-density measurements at 868 km altitude. DMSP passes for the three experimental periods are shown sequentially from top to bottom.

At trough latitudes, vertical trough structure aligns along magnetic field lines (which slope slightly equatorward with increasing altitude), since plasma diffuses along field lines between the F region and topside ionosphere. As expected, the DMSP trough-minimum densities were consistently slightly equatorward (1.5-2.0° latitude) of the $N_m F_2$ trough-minimum densities. This alignment with the DMSP troughs further reinforces the validity of the digisonde trough depictions.

CHAPTER IV

MODIFICATION OF TIME-DEPENDENT IONOSPHERIC MODEL OUTPUT
WITH LATITUDINAL ELECTRON-DENSITY PROFILES
FROM DIGISONDE TROUGH DEPICTIONS*Overview*

As mentioned in Chapter III, the primary role of the digisonde measurements was to incorporate actual trough electron-density measurements into the TDIM output for use in ray-tracing simulations. By performing ray-tracing tests through the updated TDIM output (containing realistic electron-density values and horizontal gradients), I investigated the sensitivity of ray propagation to actual trough conditions. In this chapter, I describe the comparisons made between the TDIM trough representation and the three digisonde trough depictions. I also discuss how latitudinal $N_m F_2$ profiles from the digisonde depictions (Figures 21 to 23) were used to scale the corresponding TDIM trough profiles at all altitudes. Finally, I address how the digisonde profiles were further altered with steeper trough-wall gradients characteristic of the higher-resolution DMSP electron-density profiles.

TDIM Input/Output Criteria

Before comparing the digisonde trough depictions with the TDIM output, I had to select the output most appropriate to the actual geophysical conditions during the three experimental periods. The input criteria in Tables 2, 3, and 4 specify the TDIM output conditions and the associated geophysical parameters for

TABLE 2. Season

Season	Julian Day (Day 1 = 0)
Winter	357
Summer	173
Equinox (Spring)	82

TABLE 3. Solar Activity Level

Solar Activity Level (Solar Cycle Year)	10.7-cm Solar Flux (10^{22} W/m ² - Hz)
Solar Maximum (1981)	210
Solar Medium (1984)	130
Solar Minimum (1987)	70

TABLE 4. Geomagnetic Activity

Geomagnetic Activity Level	3-Hour Kp Index Value
High	6.0
Medium	3.5
Low	1.0

the available TDIM output from previous model runs [Sojka, 1989]. All output criteria listed are for B_z negative and B_y strongly negative. As mentioned in Chapter III, the average B_y and B_z IMF components were primarily negative during the three periods. By comparing the actual ionospheric conditions listed in Table 1 with the model output criteria in Tables 2 to 4, I determined the specific TDIM output most appropriate to the ionospheric conditions of the three experimental periods were for negative B_y and B_z IMF components, spring equinox, solar maximum, and medium geomagnetic activity.

TDIM Latitudinal N_mF_2 Trough Profiles

The TDIM couples and numerically solves the F-region ion continuity and momentum equations and the ion/electron energy equations [Sojka, 1989, and Schunk, 1987] for a three-dimensional spatial array of magnetic latitude (MLAT), magnetic local time (MLT), and altitude. The latitudinal resolution is two degrees of latitude in 20 bins between 51-89° MLAT, and the MLT resolution is one hour in 24 bins (00-23 MLT). The bins are arranged such that the 51° MLAT bin ranges from 50-52° MLAT. Similarly, the 23 MLT bin spans one hour from 2300:00-2359:59 MLT (HHMM:SS) and is effectively centered at 2330 MLT. Altitude resolution varies over 37 altitude bins, with the highest resolution (four to eight km) at lower altitudes (100-204 km), decreasing in a step-like manner to the lowest resolution (100 km) at the highest altitudes (600-800 km). To account for universal time (UT) variations, the calculations are done for 12 UT bins (0-23 UT in two-hour intervals). For example, the 23 UT bin spans from 2200:00-

2359:59 UT.

Figure 26 shows latitudinal profiles of $N_m F_2$ from the TDIM output for the nine MLT bins, centered at 1830-0230 MLT in one hour increments. Since the data are in terms of $N_m F_2$, the values come from various altitudes, each of which represents the height of the F_2 -peak electron density ($H_m F_2$) at its specific location.

Overall, the TDIM troughs appeared shallow and wide, with no appreciable poleward wall. Troughs in adjacent MLT bins showed little variance. The TDIM troughs showed a definite trend with MLT. The equatorward-wall latitudinal gradients were weakest in the early evening (1830-1930 MLT) and gradually increased to peak by early morning (0130-0230 MLT). The TDIM troughs gradually shifted equatorward with increasing MLT, while the overall electron-density values decreased from evening to morning.

Digisonde Latitudinal Trough Profiles of $N_m F_2$

Figures 27 to 29 show the digisonde latitudinal $N_m F_2$ profiles for the three experimental periods, respectively. I inserted these profiles directly into the TDIM $N_m F_2$ output, thereby replacing the previous values and modifying the TDIM output. The TDIM values at other altitudes were scaled to preserve the shape of the original electron-density altitude profiles, as explained in the next section. These figures differ from Figures 21 to 23 in several respects. For instance, the latitudinal resolution was reduced from one to two degrees of latitude in Figures 27 to 29, and the profiles were plotted every 60 minutes (instead of every 30

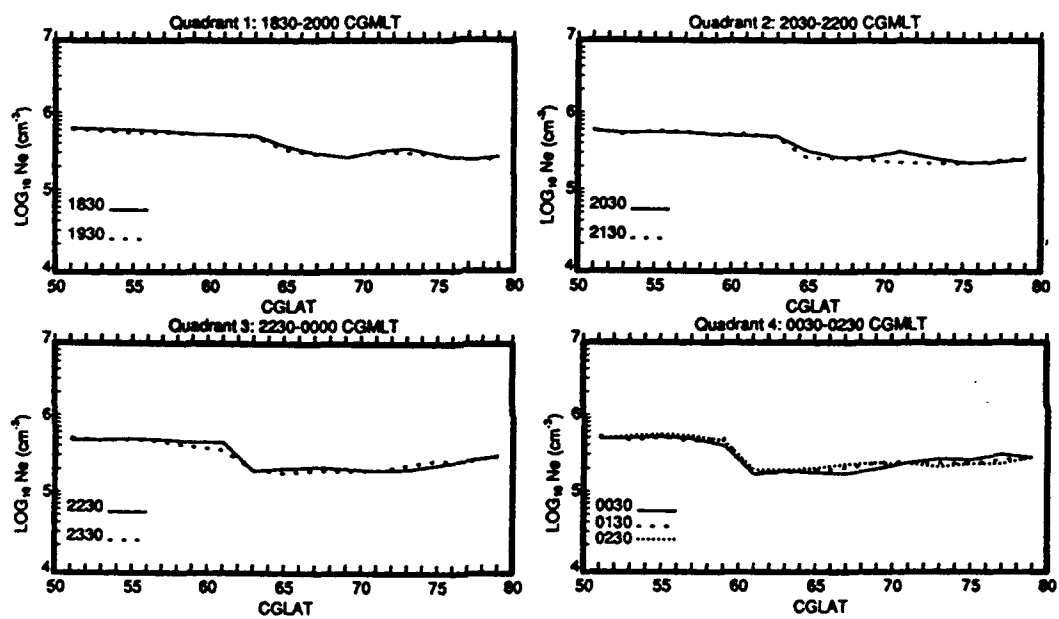


Fig. 26. Latitudinal profiles of $N_m F_2$ from the TDIM trough representation for one-hour MLT bins, centered at 1830-0230 MLT.

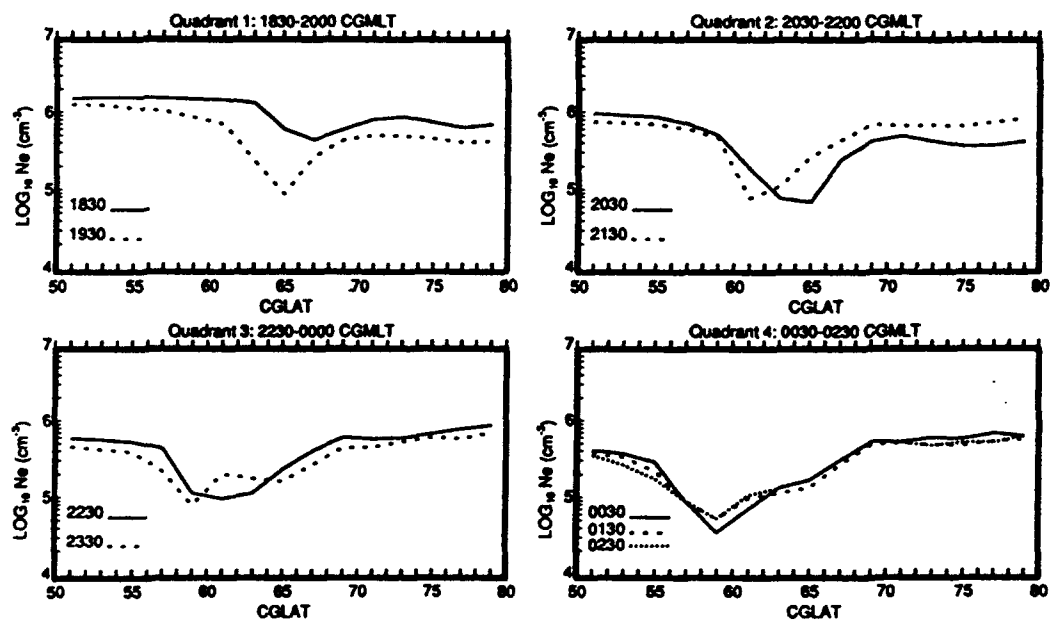


Fig. 27. Latitudinal profiles of $N_m F_2$ from the digisonde trough depictions for the first experimental period. The profiles were scaled on the equatorward and poleward edges for use in modifying the TDIM output.

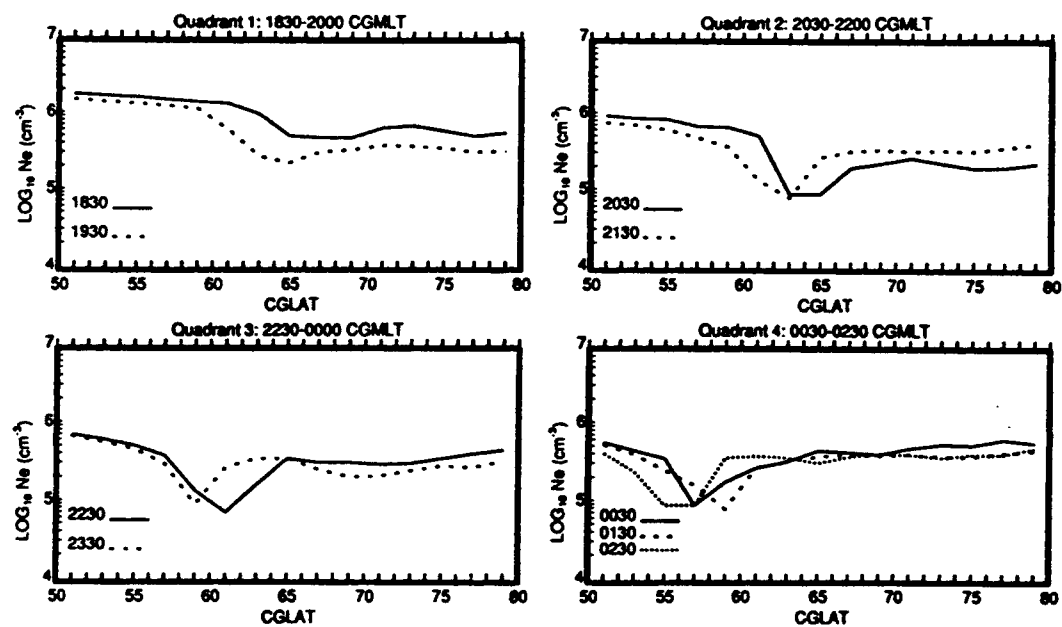


Fig. 28. Latitudinal profiles of $N_m F_2$ from the digisonde trough depictions for the second experimental period. The profiles were scaled on the equatorward and poleward edges for use in modifying the TDIM output.

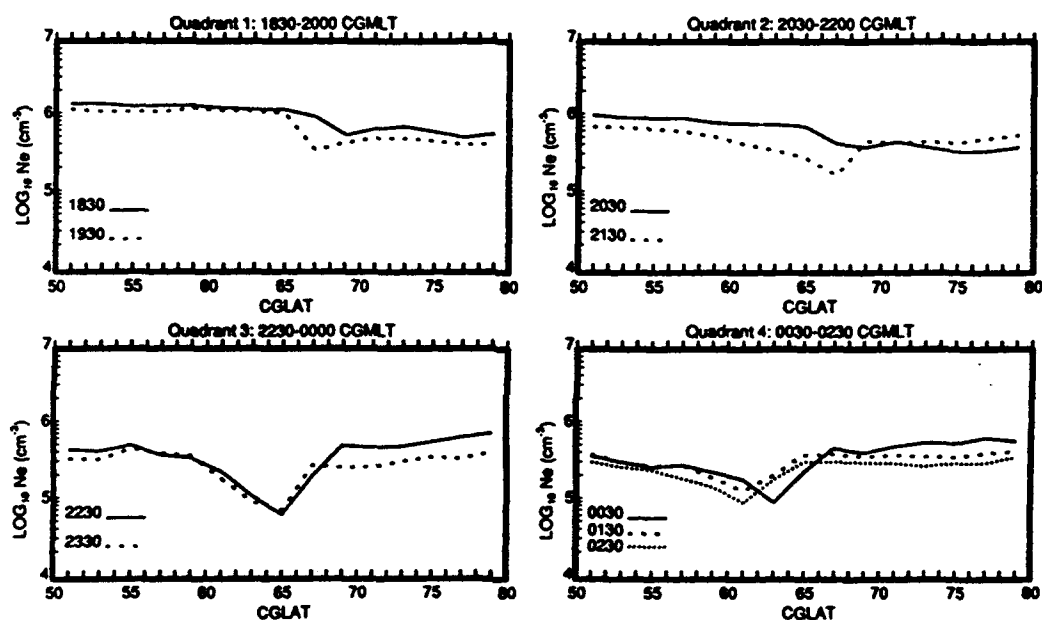


Fig. 29. Latitudinal profiles of $N_m F_2$ from the digisonde trough depictions for the third experimental period. The profiles were scaled on the equatorward and poleward edges for use in modifying the TDIM output.

minutes as in Figures 21 to 23) to properly match the TDIM latitudinal and local time resolutions. The reduced latitudinal resolution decreased the trough-wall $N_m F_2$ gradients slightly (i.e., 1830, 1930, 2230 CGMLT), but to preserve the gradients exactly would have meant altering the trough latitude location and/or minimum electron density. I chose to not change the trough latitude and minimum electron density for each digisonde profile, knowing that I might alter them later when I insert steeper trough-wall gradients characteristic of the DMSP profiles.

The Modification Process

Since the trough is primarily an F-region phenomena and O^+ is usually the dominant F-region ion, I substituted the digisonde $N_m F_2$ values for the peak O^+ concentration ($[O^+]$) of the TDIM profiles (both in logarithmic values), assuming $N_m F_2$ is nearly equal to peak $[O^+]$ at $H_m F_2$. This simple modification only replaced the $[O^+]$ values at $H_m F_2$. The correction required the shape of the original TDIM $[O^+]$ vertical profile to be preserved at all altitudes. This was accomplished by applying a vertical scaling factor (VSF),

$$VSF = \text{OLD TDIM PEAK } [O^+] - \text{DIG } N_m F_2 \quad (9)$$

$$\text{NEW TDIM } [O^+(h)] = \text{OLD TDIM } [O^+(h)] - VSF \quad (10)$$

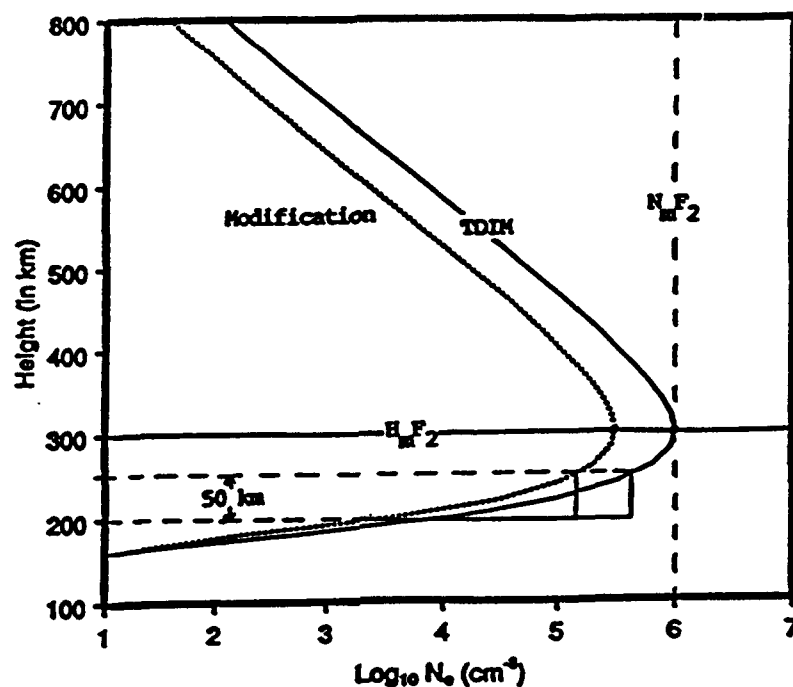
where OLD TDIM PEAK $[O^+]$ is the original TDIM peak $[O^+]$, DIG $N_m F_2$ is the digisonde $N_m F_2$ used to replace OLD TDIM PEAK $[O^+]$, OLD TDIM $[O^+(h)]$ is the O^+ concentration at a given altitude before the modification, and NEW TDIM

$[O^+(h)]$ is the O^+ concentration at a given altitude after the modification. All values in equations (9) and (10) are logarithmic.

Figure 30 shows an example of how I scaled the original TDIM $[O^+]$ vertical profiles, while still preserving the shape of the curve. In this example, the digisonde $N_m F_2$ value was less than the original TDIM peak $[O^+]$ (as was usually the case in the trough). As shown on Figure 30, applying the VSF to preserve the shape of the curve caused the vertical gradient to change at a given altitude range. Insertion of a lower $N_m F_2$ value from the digisonde measurements decreased the strength of the vertical gradient of the modified profile at the same altitude range. A higher $N_m F_2$ value similarly increased the vertical gradient.

The modification process required that I add realistic $N_m F_2$ values equatorward and poleward of the digisonde profiles in Figures 21, 22, and 23, resulting in extended profiles spanning from 51-79° CGLAT in Figures 27, 28, and 29, respectively. These additions were required to prevent unwanted drastic changes in the modified TDIM profiles, which would have been introduced at the latitudinal edges of the digisonde profiles if I had inserted the original digisonde profiles. I scaled the $N_m F_2$ additions to match the smooth TDIM gradients poleward and equatorward of the trough, but at $N_m F_2$ values consistent with the shape of the original digisonde profiles.

The three trough representations from Figure 31 depict trough structure in contours of O^+ concentration at 300 km altitude in MLAT-MLT coordinates. The top panel of Figure 31 depicts the original TDIM output (from Figure 26), while the resulting modification of the TDIM output by the first period's digisonde



Original
TDIM
Vertical
Gradient

$$\left[\frac{\text{antilog}_{10}(5.7) - \text{antilog}_{10}(5.4) \text{ cm}^{-3}}{50 \text{ km}} \right] = 5.0 \times 10^3 \text{ cm}^{-3}/\text{km}$$

Modification
(0.5 reduction
of $\log_{10} N_e$)
Vertical
Gradient

$$\left[\frac{\text{antilog}_{10}(5.2) - \text{antilog}_{10}(4.9) \text{ cm}^{-3}}{50 \text{ km}} \right] = 1.6 \times 10^3 \text{ cm}^{-3}/\text{km}$$

Fig. 30. Modification of original TDIM vertical gradients by inserting a reduced $N_m F_2$ value and applying a logarithmic vertical scaling factor (VSF) of 0.5 to correct O^+ concentration at altitudes of 100-800 km.

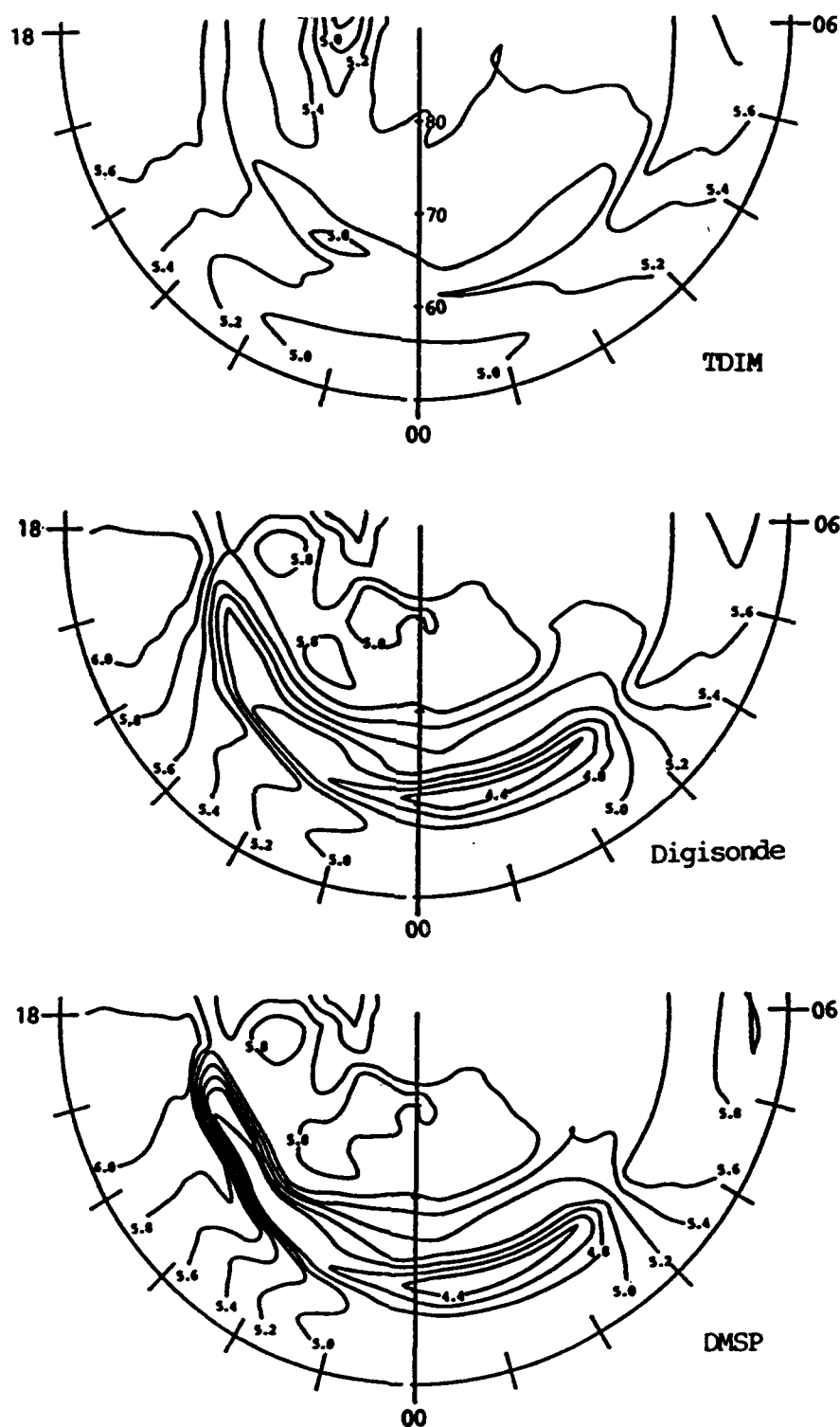


Fig. 31. Trough representations resulting from modification by digisonde latitudinal $N_m F_2$ profiles and DMSP latitudinal electron-density gradients of the trough wall. The troughs are depicted in contours of $\log_{10} O^+$ concentration at 300 km altitude in MLAT-MLT coordinates.

latitudinal profiles (from Figure 27) is shown in the middle panel. I applied the same methodology to modify the TDIM trough profiles with the scaled digisonde profiles from the second and third periods (Figures 28 and 29, respectively). The bottom panel of Figure 31 shows the modification resulting from the insertion of latitudinal electron-density gradients characteristic of the DMSP profiles from Figure 25; the modifications were made from 1900-2200 MLT. Even though the DMSP electron-density measurements were made at an orbital altitude of about 868 km, I assumed the DMSP latitudinal gradients of the trough wall were representative of values below the F_2 peak. Large-scale trough structure (depth, width, and steepness) is generally consistent for altitudes ranging from at least the F_2 peak to the topside F region [Moffett and Quegan, 1983].

To produce latitudinal electron-density gradients on the order of those found in the DMSP measurements in the trough wall, I altered the digisonde modifications to the TDIM output only in the region of the equatorward and poleward trough walls. Since I was constrained to follow the two-degree latitudinal resolution of the TDIM output, I altered the electron-density values only at three latitudes: at the latitude of the top edges of the two trough walls and at the trough-minimum density. This alteration resulted in trough-wall latitudinal gradients of $4.0 \times 10^3 \text{ cm}^{-3} \text{ km}^{-1}$ for the first case (altered from 1900-2200 MLT) and $2.9 \times 10^3 \text{ cm}^{-3} \text{ km}^{-1}$ for the second case (altered from 2100-0000 MLT). These trough-wall gradients exceeded the digisonde equatorward-wall gradients in the evening sector by a factor of about 1.5 to 2.0.

Thus, I used the digisonde latitudinal electron-density profiles as the

primary input to the original model output (i.e., a first-order update to the zeroth-order model approximation) to simulate the large-scale distribution of electron density. To this background distribution, I added large-scale latitudinal gradients characteristic of the DMSP profiles to increase the trough-wall latitudinal gradients (i.e., a second order improvement to the first-order approximation). The resulting model output, modified first by the digisonde latitudinal profiles and again by trough-wall latitudinal gradients characteristic of DMSP troughs, were the updated mediums through which I conducted the ray-tracing simulations (reported in Chapter V).

Comparisons of TDIM and Digisonde Trough Profiles

Significant differences exist between the scaled digisonde trough profiles in Figures 27 to 29 and the unmodified TDIM trough profiles in Figure 26. The most obvious difference is the scaled digisonde troughs were better defined, with much deeper minimum densities after 1830 MLT. The digisonde troughs also showed more variability with respect to MLT. For the sake of simplicity and compatibility, I assumed there was no difference between corrected geomagnetic coordinates used in the digisonde profiles and geomagnetic coordinates used in the TDIM profiles.

For the first experimental period (Figure 27), the digisonde profiles were approximately three to ten times deeper than the TDIM profiles at the trough-minimum densities. The largest difference was in the early morning sector (0030-0230 MLT), where the digisonde profiles were about eight to ten times deeper at

the trough-minimum densities. With respect to latitudinal location, the digisonde troughs were about two to four degrees of latitude equatorward of the TDIM troughs. The trough profiles from the second period (Figure 28) were similar to those from the first period (Figure 27), which is not surprising, since the two periods experienced similar geophysical conditions. As in Figure 27, the digisonde trough profiles from Figure 28 were better defined, steeper, and deeper than the corresponding TDIM profiles. Though there were differences in trough depth, width, and latitudinal location at specific MLTs between the troughs from the first two periods, they were similar overall.

The trough profiles from Figure 29 provided the closest match to the TDIM trough profiles, especially from 1830-2130 MLT; the best match was at 2030 MLT. The digisonde N_mF_2 values were slightly higher, but the gradients were similar. Agreement with respect to trough latitude was quite good. Compared to the profiles in Figures 27 and 28, the trough profiles from Figure 29 were generally shallower and shifted about two to six degrees of latitude poleward, as expected since the third period was the quietest period geomagnetically.

Comparisons of Trough-Wall Latitudinal Gradients

As in Figures 19 and 20, I calculated and plotted the latitudinal electron-density gradients of the equatorward and poleward walls, which are shown in Figures 32 and 33, respectively, for the TDIM output and the digisonde values from the three experimental periods. Instead of plotting the gradient values every 30 minutes of MLT (as in Figures 19 and 20), I only plotted hourly values

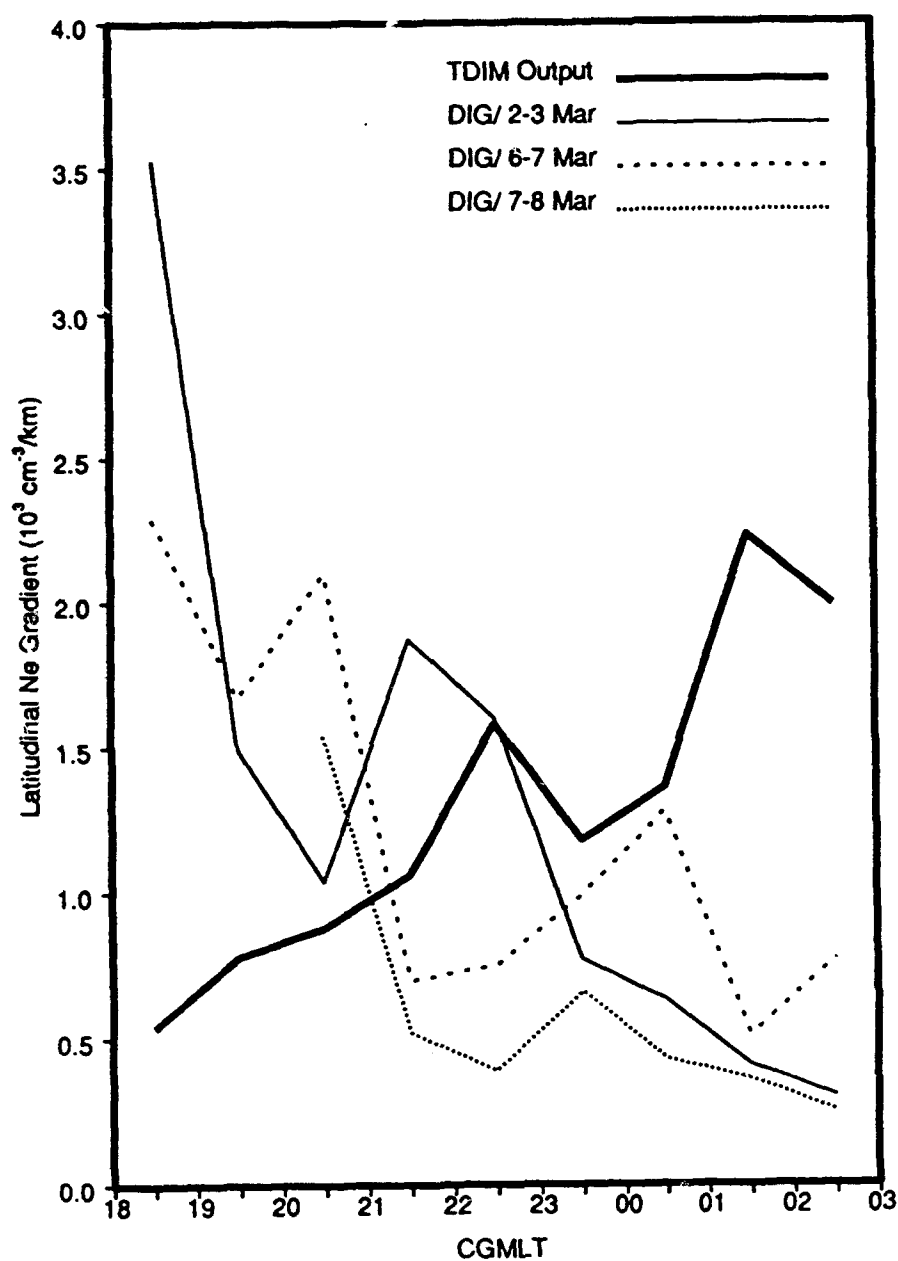


Fig. 32. Latitudinal $N_m F_2$ gradients of the equatorward wall calculated from the TDIM and digisonde trough depictions (Figures 26 and 17, respectively). Values are plotted every 60 minutes of CGMLT.

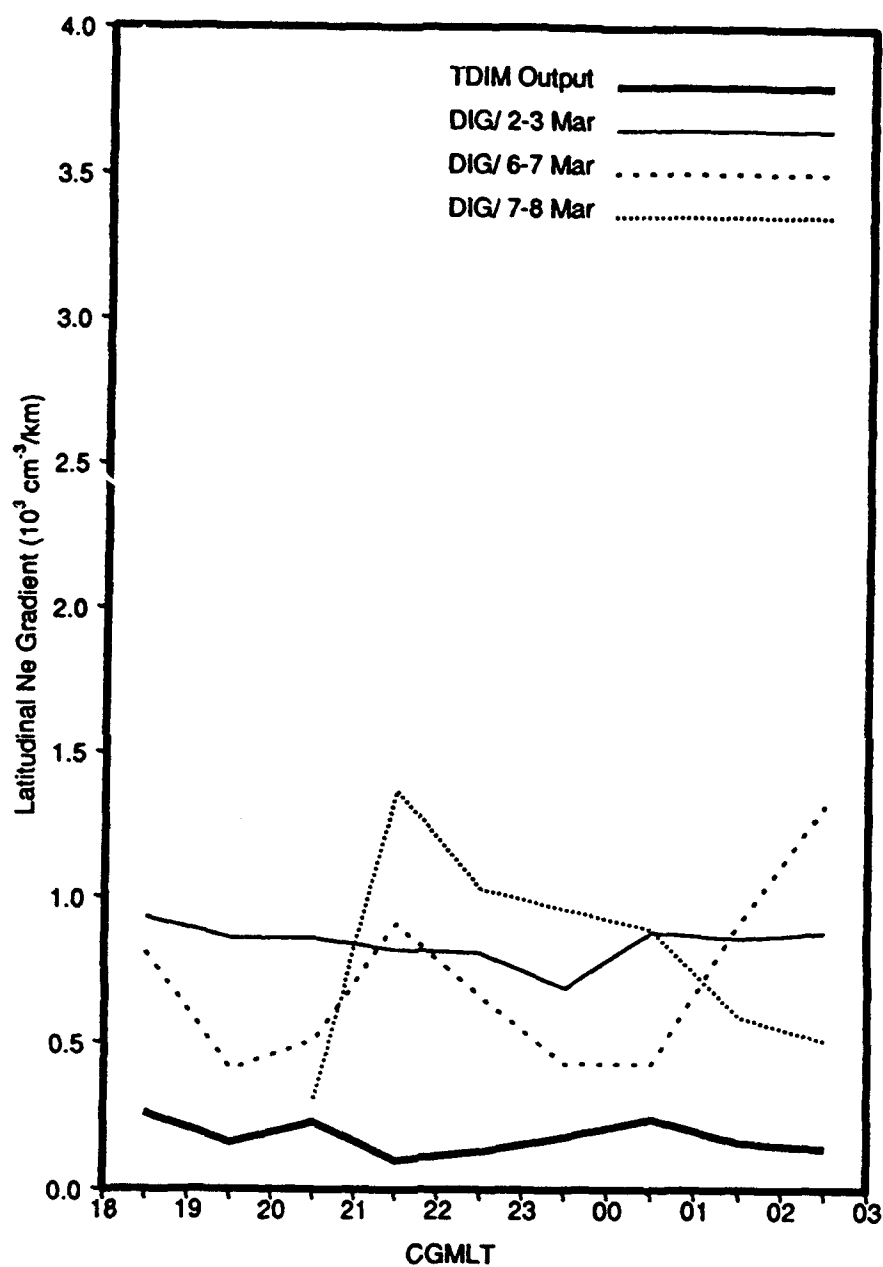


Fig. 33. Latitudinal $N_m F_2$ gradients of the poleward wall calculated from the TDIM and digisonde trough depictions (Figures 26 and 17, respectively). Values are plotted every 60 minutes of CGMLT.

(centered at half past the hour, i.e., 2030 MLT) from 1830-0230 MLT to match the MLT resolution of the TDIM output.

In reference to the latitudinal gradients of the equatorward wall from Figure 32, no period consistently had the strongest gradients over the range of MLTs shown, though the third period typically had the weakest gradients. Though there were large differences in the gradients for the three periods, they all generally decreased from evening to morning, contrary to the trend shown by the equatorward-wall gradients from the TDIM output. A comparison of equatorward-wall gradients from the digisonde depiction for the first period and the TDIM output shows the digisonde gradients were about two to seven times stronger than the TDIM gradients from 1830-2130 MLT (except at 2030 MLT), though the TDIM gradients were two to five times stronger after 2230 MLT. They were nearly identical at 2230 MLT. The equatorward-wall gradients from the second period were similar to the those of the first period, though the peaks at specific MLTs seemed to anticorrelate.

On Figure 33, the latitudinal gradients of the poleward wall from the TDIM output were always weaker than the digisonde gradients from the three experimental periods. There was little MLT variation in the poleward-wall gradients from the first period, in contrast to the equatorward-wall gradients. In Figure 33, the poleward-wall gradients from the digisonde trough depictions were consistently about two to seven times stronger than the corresponding poleward-wall gradients from the TDIM trough representation. The poleward-wall gradients from the second and third periods varied more with respect to MLT than those

from the first period. Localized peaks in the poleward-wall latitudinal gradients may have been associated with discrete auroral activity. However, as mentioned in Chapter III, the poleward-wall gradients were less certain than the equatorward-wall gradients, due to the data deficiency poleward of Goose Bay.

CHAPTER V

RAY-TRACING SIMULATIONS TO EXAMINE GROUND RANGE

Overview

I used a modified version of the *Jones and Stephenson* [1975] numerical ray-tracing program to simulate radio-wave propagation through trough representations from the TDIM model output, the digisonde modifications to the TDIM output, and the DMSP modifications of the digisonde trough-wall electron-density gradients. I established two primary objectives for the ray-tracing simulations. First, by comparing ray-tracing results through the digisonde and DMSP trough representations to the TDIM modelled trough, I identified the largest ground-range differences for the rays that reached the surface. I assumed the ray-tracing simulations through the digisonde and DMSP trough depictions represented actual radio waves propagating through the mid-latitude trough. Following this assumption, the differences in ray-tracing results between the TDIM and digisonde/DMSP trough representations signified the ability of the most sophisticated ionospheric model available to simulate the electron-density structure of the trough for use in numerical ray-tracing simulations.

Second, by performing ray-tracing tests through realistic digisonde and DMSP trough representations, I examined the effects of realistic three-dimensional electron-density gradients on ray propagation. My ultimate goal was to determine the sensitivity of high-frequency radio propagation systems, such as the OTH-B

radar, to electron-density values (and their associated three-dimensional gradients) found in realistic troughs.

Jones and Stephenson Ray-Tracing Program

The *Jones and Stephenson* [1975] ray-tracing computer program numerically integrates Hamilton's equations to simulate ray propagation through the ionosphere, taking into account the effects of electron density, earth's magnetic field, and the electron-neutral collision frequency in the computation of the ionospheric refractive index. The program's subroutines provided an earth-centered dipole model of the geomagnetic field, an exponential height-profile model of the electron-neutral collision frequency, and a means to interface with the three-dimensional distributions of electron density provided by the TDIM output and its modifications.

Huffines [1990] altered the ray-tracing program to interface with the TDIM electron-density model output. He accomplished this by creating computer subroutines to perform a three-dimensional spline fit to the modelled electron-density distribution at any position with respect to altitude, magnetic latitude, and magnetic local time. This refinement allowed the program to calculate the three spatial components of the electron-density gradient along the ray path, satisfying the program's requirement that they remain continuous functions of position. The Appendix contains further details on the ray-tracing program, its operation, and the subroutines I used in this study.

Ray-Tracing Methodology

All ray-tracing tests were performed in the evening MLT sector, where the strongest horizontal electron-density gradients were located. The transmitter site used in all the ground-range simulations was located at 49.0° north, 290.6° west in geographic coordinates (59.0° north MLAT, and 2030 MLT in geomagnetic coordinates). This location was about five degrees of latitude poleward of the OTH-B radar site at Bangor, Maine. I chose this transmitter site because it provided the ability to test a wide range of launch elevation angles (10.0 - 60.0°) in close proximity to the trough representations (Figures 34 to 36). The transmitter site would be located at Bangor if the trough representations in Figures 34 to 36 were shifted about five degrees of latitude equatorward.

Figures 34 to 36 show the transmitter site with respect to the trough representations from the TDIM output and the corresponding modifications from the three experimental periods; trough structure is depicted in contours of O^+ concentration at 300 km altitude in MLAT-MLT coordinates. The approach I used was to select four azimuth angles of transmission to aim the rays through different trough regions, as shown in Figures 34 to 36. For each trough representation tested, I performed ray-tracing tests at each of the four azimuths for variable elevation angles (10.0 - 60.0°), while keeping frequency constant at 6.0 MHz. I then ray traced through the trough representations from the TDIM output and the digisonde and DMSP trough representations from the first period for variable frequencies (3.0-13.0 MHz) at a constant elevation angle (different for

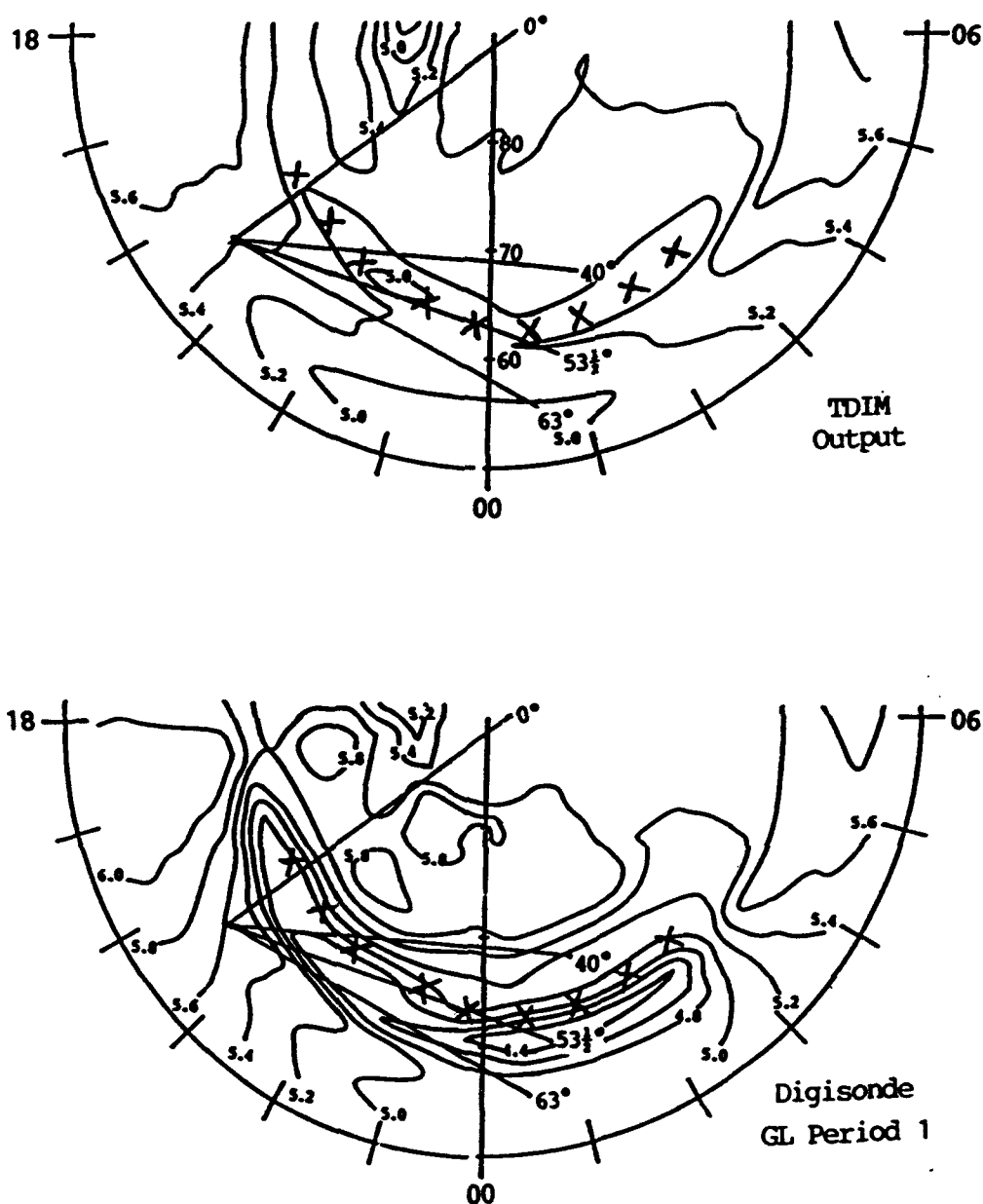


Fig. 34 Trough representations depicted in contours of $\log_{10} O^+$ concentration at 300 km altitude in MLAT-MLT coordinates. The top panel shows the TDIM trough depiction and the bottom panel shows the digisonde trough depiction from the first experimental period. The line of X's marks the location of trough-minimum densities from the TDIM output.

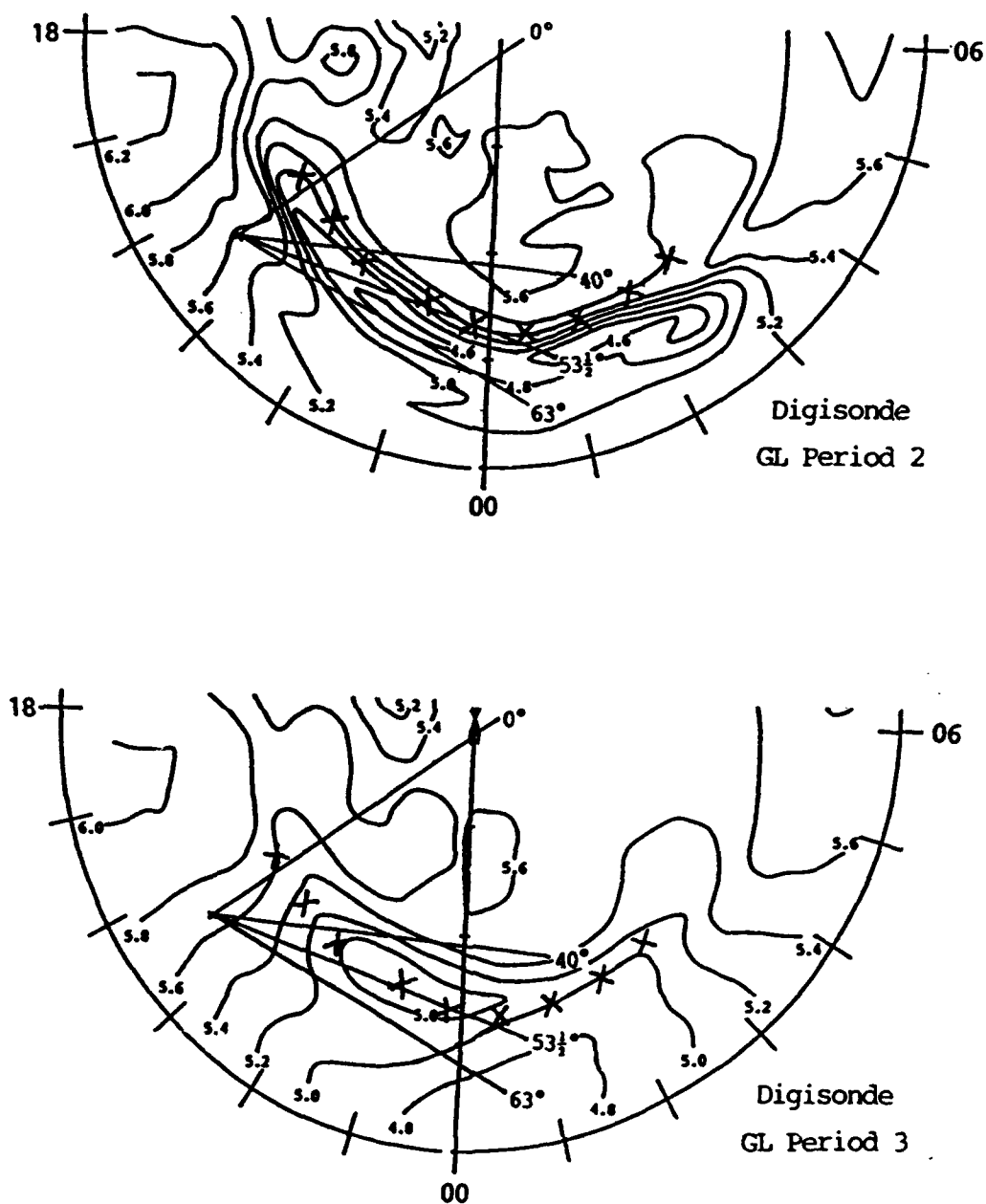


Fig. 35. Trough representations depicted in contours of $\log_{10} O^+$ concentration at 300 km altitude in MLAT-MLT coordinates. The top and bottom panels show the digisonde trough depictions from the first and second experimental periods, respectively. The line of X's marks the location of trough-minimum densities from the TDIM output.

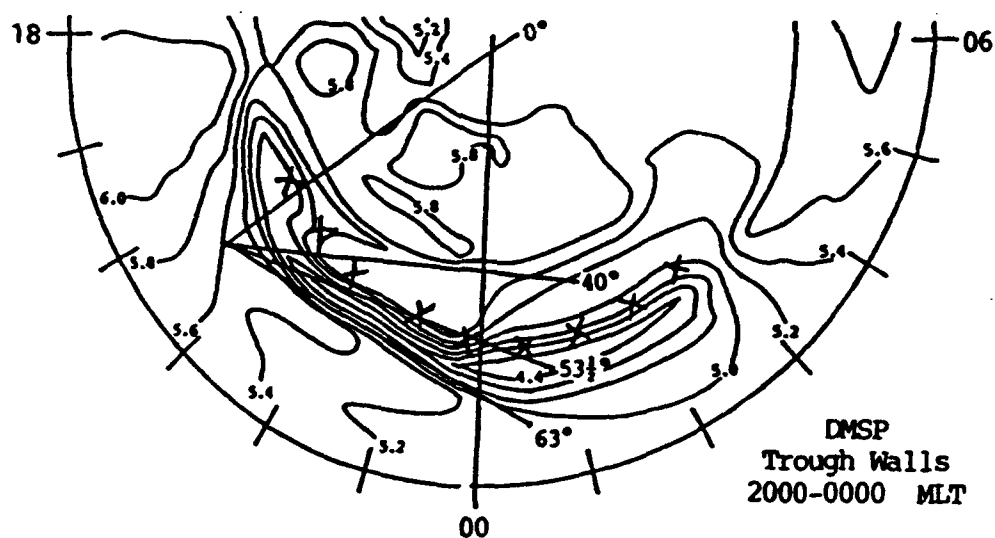
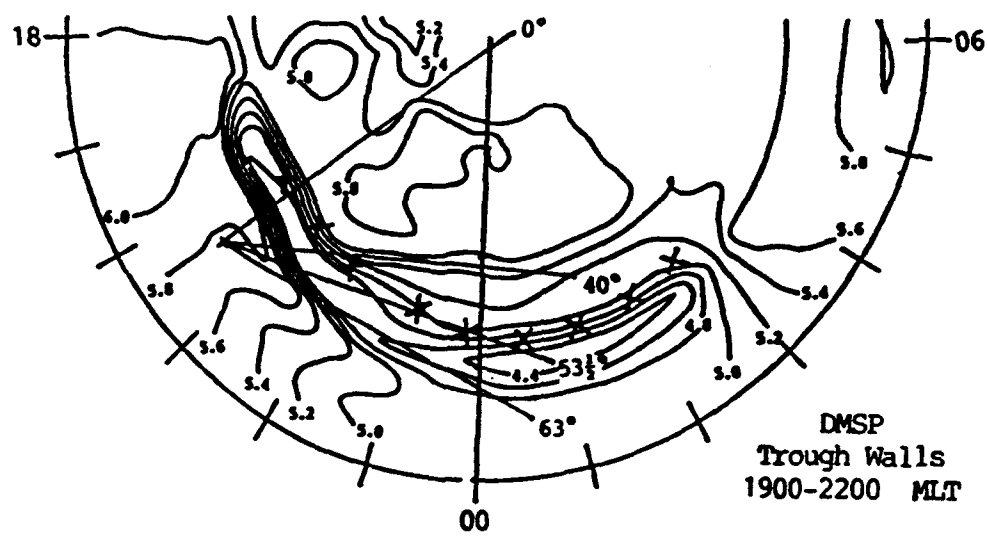


Fig. 36. Trough representations depicted in contours of $\text{Log}_{10} O^+$ concentration at 300 km altitude in MLAT-MLT coordinates. The top and bottom panels show two DMSP depictions of the trough-wall from the first experimental period. The line of X's marks the location of trough-minimum densities from the TDIM output.

each of the four azimuths tested).

Both DMSP modifications from Figure 36 were extracted from DMSP passes during the first period. The top panel of Figure 36 shows the DMSP modification used for azimuths 53.5° , 40.0° , and 0.0° . The DMSP modification in the bottom panel was only used for azimuth 63.0° , because the ray path was nearly parallel to the trough equatorward wall, an orientation not possible for the DMSP modification in the top panel for the transmitter location I selected.

Throughout the ray-tracing simulations, I concentrated on finding the ray-transmission parameters (azimuth and elevation angles) at which the ground range of the ray's landing point was most different from that of the corresponding ray path through the TDIM trough. These parameters determined which trough region the ray was directed into from the transmitter site.

Trough Structure Along the Ray Path

Before presenting the ray tracing results, it is appropriate to review the main differences in trough structure between the various trough depictions (as shown on Figures 34 to 36) with respect to the ray paths used in the ray-tracing simulations. The trough electron-density differences along a given ray path, as specified by a given azimuth, determined the ray-path behavioral differences as the rays propagated through the various trough representations. The ray paths at the various azimuths differed in two main respects: 1) the region of the trough in which they were aimed, and 2) their orientation with respect to the electron-

density isolines. I compared ray-path locations in the trough depictions with respect to the corresponding locations in the TDIM trough representations. The line of X's on Figures 34 to 36 marks the location of trough-minimum O^+ densities from the TDIM modelled trough. I assumed O^+ density was equal to electron density at 300 km altitude.

As discussed in Chapters III and IV, the digisonde troughs from the first two periods resembled each other with respect to trough location, width, depth, and horizontal gradients. This is not surprising, since geomagnetic conditions and the resulting trough structure were similar during the first two periods. The 300 km trough-minimum O^+ densities from the first two periods (Figures 34 and 35) were consistently about two to four degrees of latitude equatorward of the TDIM trough-minimum densities (trough base). The digisonde trough-base densities were about 1.5-6.0 times deeper than the TDIM trough-base densities in the evening sector. As a result, the digisonde latitudinal trough-wall gradients from the first two periods were much steeper than the TDIM trough-wall gradients. In contrast, equatorward of the trough, from about 2030-2130 MLT, the digisonde O^+ density modifications from the first two periods were about 1.2-1.6 times higher than the corresponding TDIM values. These enhanced densities occurred early along the various ray paths (close to the transmitter), and would most affect high elevation-angle rays.

The digisonde trough representation from the third period (Figure 35, bottom panel) was markedly different from those of the first two periods. Since

the level of geomagnetic activity was relatively low, the digisonde trough representation from the third period was shifted about three to five degrees of latitude poleward of the first two period's troughs. The relatively quiet magnetic activity level also caused the third-period trough to be shallower, with more gradual horizontal electron-density gradients relative to the troughs from the first two periods. However, the third-period trough provided the closest match to the TDIM trough. The digisonde trough base was about one to two degrees of latitude poleward of the TDIM trough base. Trough-minimum O^+ density values were similar in the evening sector, except from 2030-2130 MLT. Equatorward of the trough, also from about 2030-2130 MLT, the third-period trough densities were about 1.2-1.6 times larger than the corresponding TDIM values at 300 km altitude, as in the first two periods.

The DMSP trough representations (Figure 36) differed from the digisonde trough depiction from the first period in only one respect: steepness of the latitudinal electron-density gradients in the trough walls. The DMSP trough in the top panel of Figure 36 had the strongest trough-wall latitudinal gradients (1900-2200 MLT) used in the ray-tracing simulations. In the bottom panel of Figure 36, the DMSP latitudinal gradients were nearly perpendicular to the 63.0° azimuth ray path in the equatorward wall (from 2100-0000 MLT).

Ground-Range Test Results at a Fixed Frequency

Figures 37 to 40 show the ground-range test results at the four azimuths

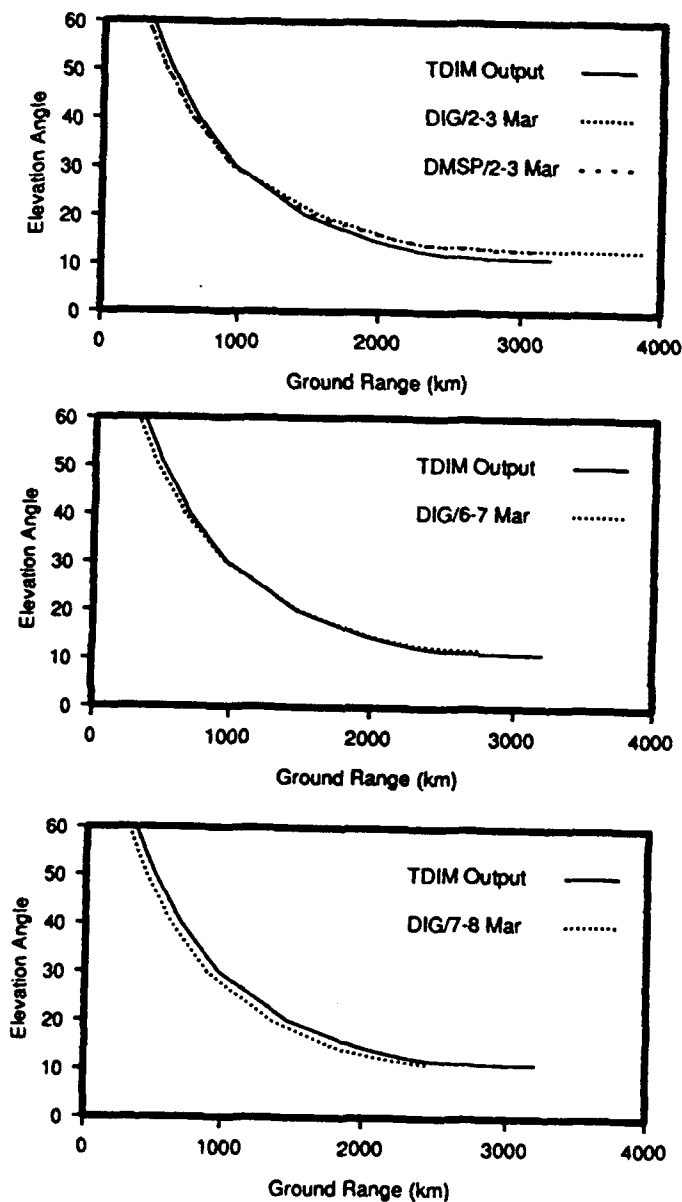


Fig. 37. Ray-tracing results of ground-range tests for a range of elevation angles ($10-60^\circ$) at a fixed frequency of 6.0 MHz and an azimuth of 63.0° . Results for rays which passed through the TDIM, digisonde, and DMSP trough representations are shown.

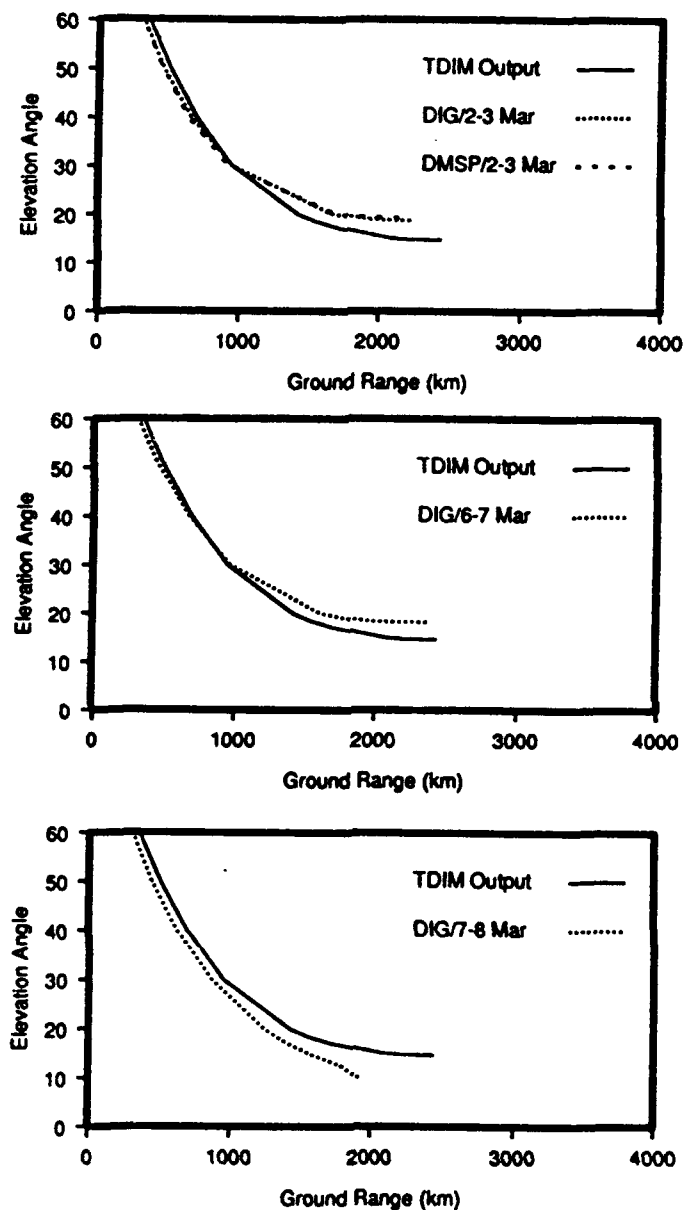


Fig. 38. Ray-tracing results of ground-range tests for a range of elevation angles ($10-60^\circ$) at a fixed frequency of 6.0 MHz and an azimuth of 53.5° . Results for rays which passed through the TDIM, digisonde, and DMSP trough representations are shown.

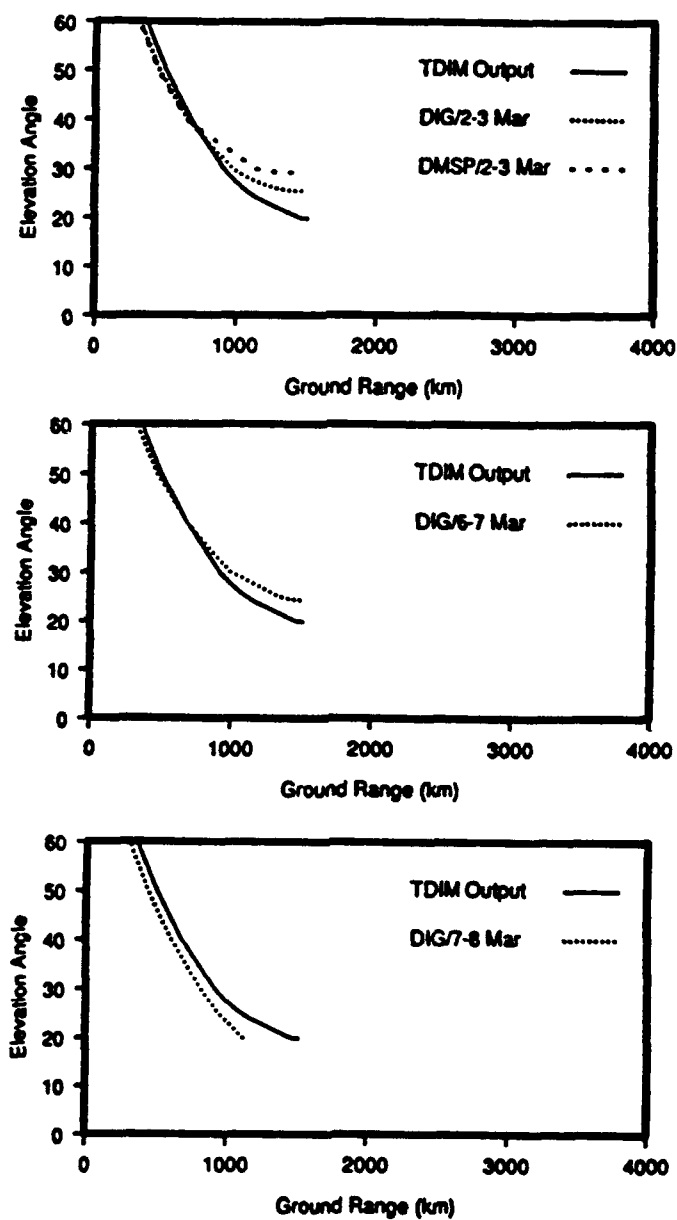


Fig. 39. Ray-tracing results of ground-range tests for a range of elevation angles (10-60°) at a fixed frequency of 6.0 MHz and an azimuth of 40.0°. Results for rays which passed through the TDIM, digisonde, and DMSP trough representations are shown.

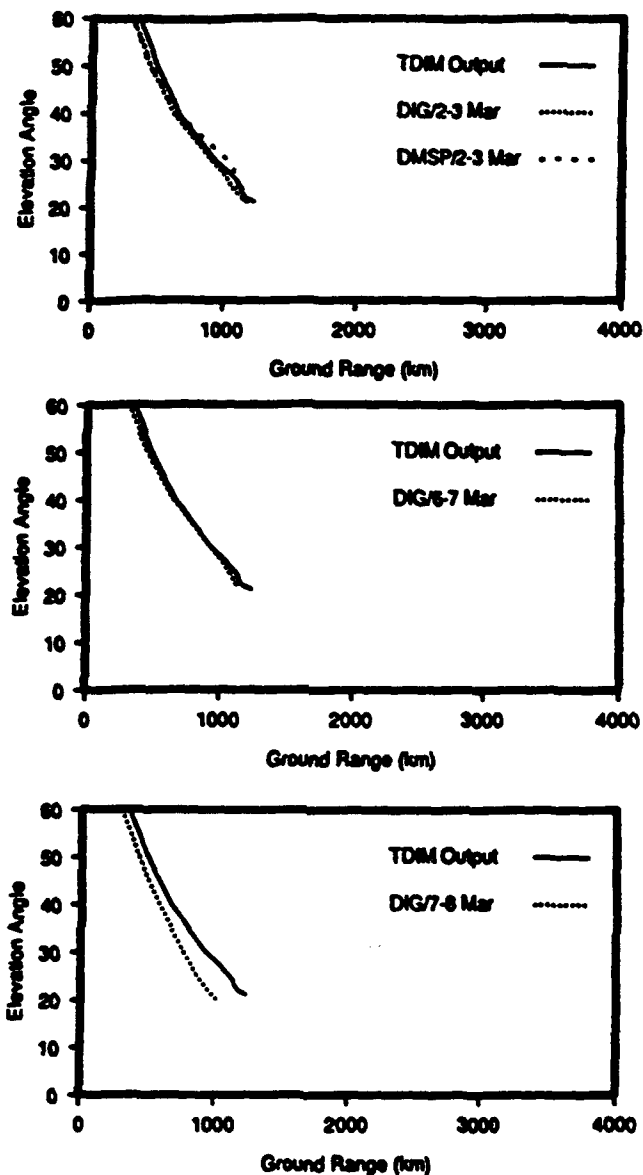


Fig. 40. Ray-tracing results of ground-range tests for a range of elevation angles ($10-60^\circ$) at a fixed frequency of 6.0 MHz and an azimuth of 0.0° . Results for rays which passed through the TDM, digisonde, and DMSP trough representations are shown.

selected (63.0° , 53.5° , 40.0° , and 0.0°). Each figure shows the results for the troughs from the TDIM output and the three experimental periods, with ground range plotted for the various elevation angles tested (12.0 - 60.0°). Ray frequency was held constant at 6.0 MHz. Figures 37 to 40 clearly show the results adhered to a fundamental principle of ray-path geometry: ground range increases as the elevation angle decreases. Another clear feature of these figures is the overall agreement between the ground-range results for the TDIM output and the digisonde and DMSP modifications, with notable exceptions at the lowest elevations for each azimuth. Ground-range results from the first two periods were quite similar to each other, while the third-period results differed from the first two periods. This is as expected, since the digisonde troughs from the first two periods resembled each other, while the trough from the third period was unique.

For the first two periods, the ground ranges for rays which passed through the modified troughs exceeded the corresponding TDIM values at the lowest elevations angles for three of the azimuths tested (63.0° , 53.5° , and 40.0°). Conversely, the ground-range values from the TDIM output were larger at higher elevation angles (above about 30 - 40°) at the same three azimuths. This transition elevation angle increased with decreasing azimuth (i.e., near 27° at 63.0° azimuth, and near 37° at 40.0° azimuth for the first period). These ground-range (GR) test results are summarized in Table 5. DIG and DMSP refer to the digisonde and DMSP modifications, respectively, and EP refers to the experimental period of the trough modification.

TABLE 5. Summary of Ground-Range Tests at 6.0 MHz

Azimuth	Modification	Elevation Angles	
		GR > TDIM	GR < TDIM
63.0	DIG/EP1	12.9-27.0	28.0-60.0
63.0	DMSP/EP1	12.9-27.0	28.0-60.0
63.0	DIG/EP2	11.9-24.0	28.0-60.0
53.5	DIG/EP1	18.7-29.0	30.0-60.0
53.5	DMSP/EP1	19.2-29.0	30.0-60.0
53.5	DIG/EP2	18.5-34.0	35.0-60.0
40.0	DIG/EP1	25.4-36.0	37.0-60.0
40.0	DMSP/EP1	29.2-37.0	38.0-60.0
40.0	DIG/EP2	24.2-39.0	40.0-60.0

At 0.0° azimuth, the ground-range results from the first two periods (with the exception of results from the DMSP modification at elevation angles of about 25-37°) resembled the results from the third period at all four azimuths tested. In these cases, the rays from the trough modifications usually landed closer in ground range than the corresponding TDIM values. The differences in ground range can be explained by variations in vertical electron-density gradients along the ray path.

Following the ray-propagation review in Chapter II, a radio wave in the ionosphere refracts away from the direction of the component of an electron-density gradient that is perpendicular to the ray path. The ray refracts more for

stronger gradients, and conversely, less for weaker gradients. Positive vertical gradients in the ionosphere cause the ray to refract downwards, while negative vertical gradients cause the ray to refract upwards. The strength and sign of the vertical gradients and the size of the normalized electron density (X value from equation (2)), as experienced by the ray along its path through the ionosphere, determine the ground range at which it lands from the transmitter. The role of X will be discussed in Chapter VI. Often, rays launched at the lowest elevation angles (about $10\text{-}20^\circ$, depending on azimuth) were trapped by the ionosphere and prevented from reaching the earth's surface. These rays obviously did not have ground ranges to plot, though they did reach apogee in the F region, only to become trapped by weak vertical gradients during descent from apogee.

Upon examination of the apogees of the ray paths with respect to trough location for the first two periods, I found the lower elevation-angle rays (about $12\text{-}30^\circ$) refracted in the equatorward-wall of the F-region trough. These rays landed at shorter ground ranges than the corresponding TDIM values. As the rays travelled farther poleward into the steep latitudinal gradients of equatorward trough walls from the first two periods, they encountered lower electron densities than rays in the corresponding locations of the TDIM trough. The resulting vertical electron-density gradients were weaker in the troughs from the first two periods, as shown in Figure 30. These low elevation-angle rays were slower to refract downward in response to the weaker vertical gradients, and as a result, landed at a longer ground range than the same rays through the TDIM output

(TDIM rays).

Conversely, the higher elevation-angle rays (above 26-40°, depending on azimuth) for the first two periods refracted equatorward of the trough, where the electron density was higher than the corresponding values in the TDIM output. These rays landed in a shorter ground range than the same TDIM rays, because they encountered stronger vertical gradients. Stronger vertical gradients also caused the rays from the third period to land in a shorter ground range at all elevation angles for each azimuth tested. The trough from the third period was not as deep as the first two period's troughs, and it was also shifted farther poleward. These rays encountered stronger vertical gradients during their ascent and early descent, causing them to refract downward before they reached the weaker vertical gradients of the trough base.

The largest differences in ground range between rays from the modified trough representations and the corresponding TDIM rays from Figures 37 to 40 occurred at the lowest elevation angles (about 12-30°). Table 6 lists the most extreme differences for each of the azimuths tested. The ground-range ratio was calculated by dividing the ground range for the ray from the modified trough representation by the ground range for the same ray from the TDIM output. I will examine some of the extreme cases in detail in Chapter VI. The ray-tracing results from the third period were due mostly to ray propagation equatorward of the trough, where the vertical electron-density gradients were stronger than in the TDIM output. The digisonde trough modifications were quite similar for the first

TABLE 6. Largest Ground-Range Differences at Each Azimuth

Trough Mod	Az	Elev	Ground Range (km)		Ground Range Difference	Ratio
			TDIM	Trough Mod	(km)	
DIG/EP1	63.0	12.9	2243	3866	+1623	1.72
DMSP/EP1	63.0	12.9	2226	3073	+830	1.37
DIG/EP2	63.0	11.9	2474	2755	+281	1.11
DIG/EP3	63.0	11.2	3207	2444	-763	0.76
DIG/EP1	53.5	18.7	1532	2221	+689	1.45
DMSP/EP1	53.5	19.2	1489	2142	+653	1.44
DIG/EP2	53.5	18.2	1580	2370	+790	1.50
DIG/EP3	53.5	14.7	2442	1581	-861	0.65
DIG/EP1	40.0	25.4	1084	1476	+392	1.36
DMSP/EP1	40.0	29.2	940	1406	+466	1.50
DIG/EP2	40.0	24.2	1144	1494	+350	1.31
DIG/EP3	40.0	19.8	1518	1123	-395	0.74

two periods, but the equatorward-wall latitudinal gradients were slightly stronger during the first period at the MLT of the ray paths. Additionally, the DMSP modifications were taken from satellite passes during the first period. For these reasons, I will concentrate only on the ray-tracing results from the first experimental period from here on.

Ray Propagation for Different Trough Regions

A comparison of the ray paths through the digisonde modification for the different azimuths provided insight on ray-path behavior in different trough regions. Figures 41 to 44 show the ground-range test results at the same four azimuths as in Figures 37 to 40, except only for trough representations from the first period. These figures also display the ground-range differences and ground-range ratios between the rays from the digisonde and DMSP troughs, as compared to the same rays from the TDIM troughs. The four azimuths had little difference in ground range for rays with elevation angles greater than about 30° . These rays encountered similar conditions (relatively high electron densities equatorward of the trough) at the four azimuths during refraction, reaching the lower densities of the equatorward wall only after they were refracted down.

However, large ground-range differences existed at elevation angles below 30° , especially for the lowest elevation angles at each azimuth. For instance, on Figure 41, the 12.9° elevation ray from the DMSP trough had a 72.4% higher ground range than the corresponding ray through the TDIM trough (a 1623-km difference). The rays at the various azimuths encountered the trough equatorward wall at different orientations during vertical refraction, as shown on Figure 34, bottom panel. Rays at 63.0° azimuth (Figure 41) generally refracted at an oblique angle to the MLT extent of the equatorward wall. The 63.0° azimuth rays between elevation angles of 11.1 - 12.8° were trapped as they reached the weak vertical gradients in the trough base (electron-density values below the $\log_{10} N_e$ of 4.8 cm^{-3} on Figure 34, bottom panel). At azimuth 53.5° (Figure 42), the rays also refracted

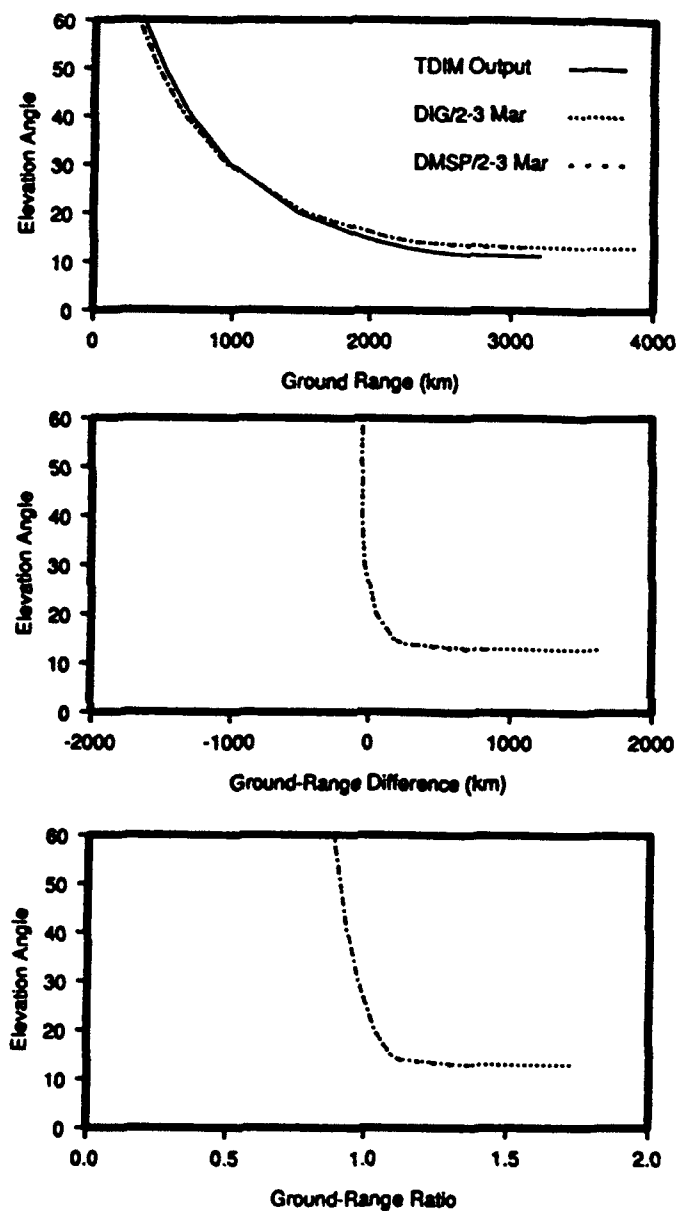


Fig. 41. Ground-range difference and ground-range ratio for ray-tracing test results from the first experimental period at a fixed frequency of 6.0 MHz and an azimuth of 63.0° .

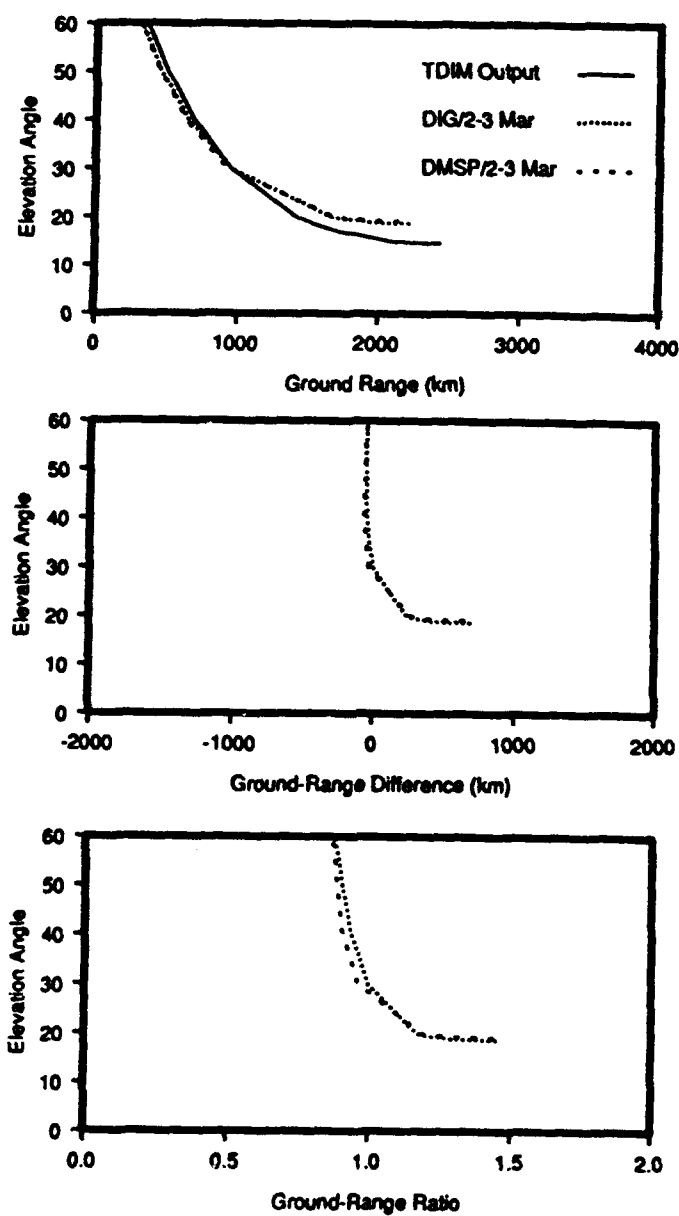


Fig. 42. Ground-range difference and ground-range ratio for ray-tracing test results from the first experimental period at a fixed frequency of 6.0 MHz and an azimuth of 53.5°.

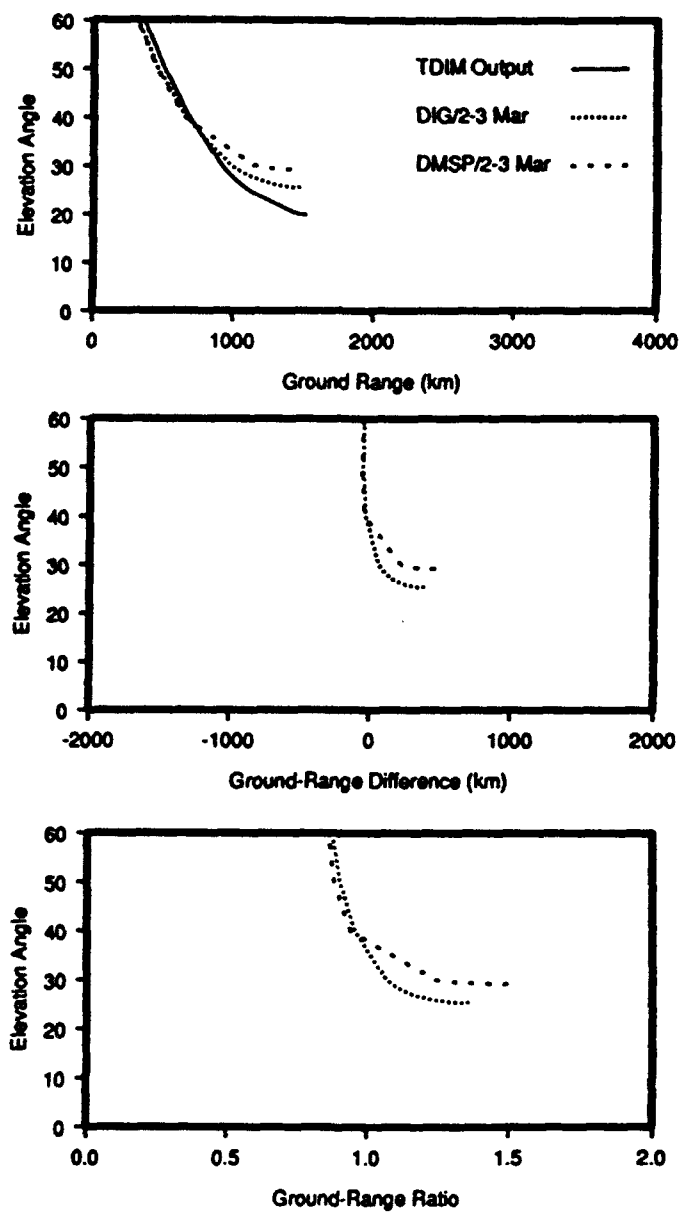


Fig. 43. Ground-range difference and ground-range ratio for ray-tracing test results from the first experimental period at a fixed frequency of 6.0 MHz and an azimuth of 40.0° .

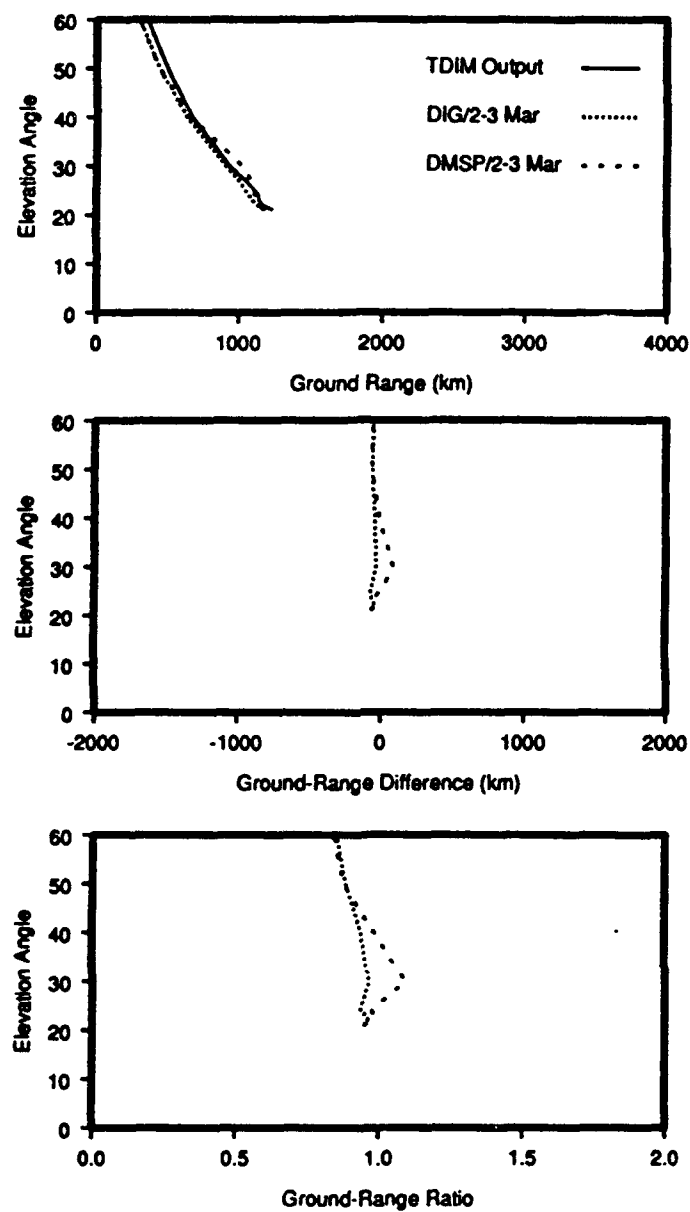


Fig. 44. Ground-range difference and ground-range ratio for ray-tracing test results from the first experimental period at a fixed frequency of 6.0 MHz and an azimuth of 0.0° .

in the equatorward wall, but at a more direct angle. These rays were trapped at elevation angles of 10.0 - 18.6° , reaching the weak trough-base vertical gradients over a wider range of elevation angles and a lower threshold (10.0°) than that of the 63.0° azimuth rays. The only 53.5° azimuth ray tested at an elevation angle below 18.7° that landed was for an E-region reflection (125 km apogee) at 9.0° elevation. Rays at elevation angles below 10.0° (all azimuths) typically only reached the earth's surface for reflections off the enhanced auroral-E region included in the TDIM output just poleward of the trough base.

Rays at azimuth 40.0° (Figure 43) were incident on the equatorward wall at an angle of about 45° , reaching the low trough-base electron densities earlier than for higher-azimuth rays. These rays were trapped for a wide range of elevation angles (12.4 - 25.3°), and penetrated at 10.0 - 12.3° . At azimuth 0.0° , the rays were roughly perpendicular to the equatorward wall, reaching the trough base along the most direct route. Though not plotted on Figure 44, rays at elevation angles of 10.0 - 12.0° reflected from the E and lower-F regions and landed at ground ranges of 894-2006 km from the transmitter. Higher electron densities at the earlier MLT (2030 instead of about 2130 for the other three azimuths) prevented these rays from penetrating at 6.0 MHz. However, 0.0° azimuth rays were trapped at elevation angles of 12.1 - 20.0° , due to the weak trough-base vertical gradients.

Figures 41 to 44 show that as the ray azimuth decreased, the rays with large ground-range differences shifted to higher elevation angles. This is because as ray

azimuth decreased, rays became trapped over a wider range of elevation angles as the threshold for trapping or penetrating also shifted to higher elevation angles. Additionally, the range of elevation angles which had a large ground-range difference increased. This trend occurred because the lower-azimuth rays were aimed more directly into the trough base, where they encountered weaker vertical electron-density gradients at higher elevation angles and over a larger range of elevation angles. Instead of trapping, they were able to reach the earth's surface, though at a farther ground range. Additionally, ground-range differences at the lowest elevation angles increased with increasing azimuth. This trend occurred because the higher azimuth rays (i.e., 63°) were incident to the trough equatorward wall at a more oblique angle, and as a result, travelled through the weak vertical gradients over a longer group path.

Ground-Range Test Results at a Variable Frequency

Figures 45 to 48 show the ground-range test results at the four azimuths selected (63.0° , 53.5° , 40.0° , and 0.0°) for trough representations from the TDIM output and the first experimental period. The tests were conducted for various ray frequencies (3.0-13.0 MHz, in steps of 2.0 MHz) at a constant elevation angle (different for each azimuth tested). I initially tried to use the elevation angle with the largest ground-range difference at each azimuth from the previous fixed-frequency tests. However, this method proved unsuccessful for comparisons with the corresponding TDIM rays, because all rays at frequencies above 6.0 MHz were

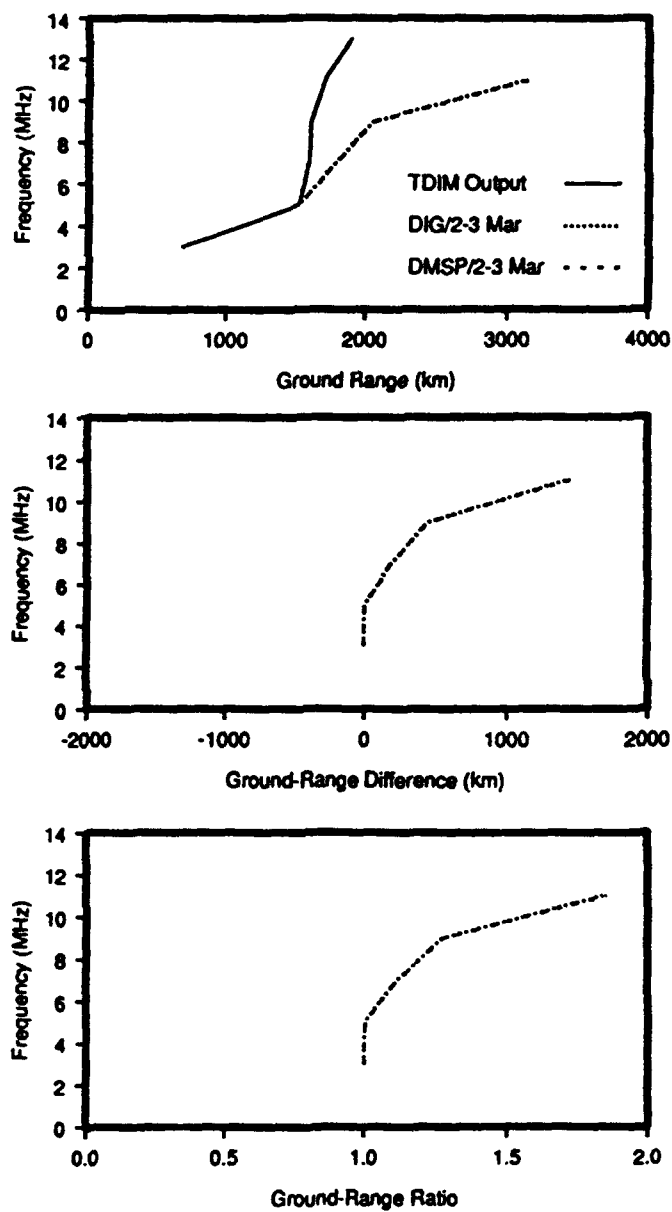


Fig. 45. Ray-tracing results of ground-range tests from the first experimental period for a range of frequencies (3.0-13.0 MHz) at a fixed elevation angle (18.0°) and an azimuth of 63.0° .

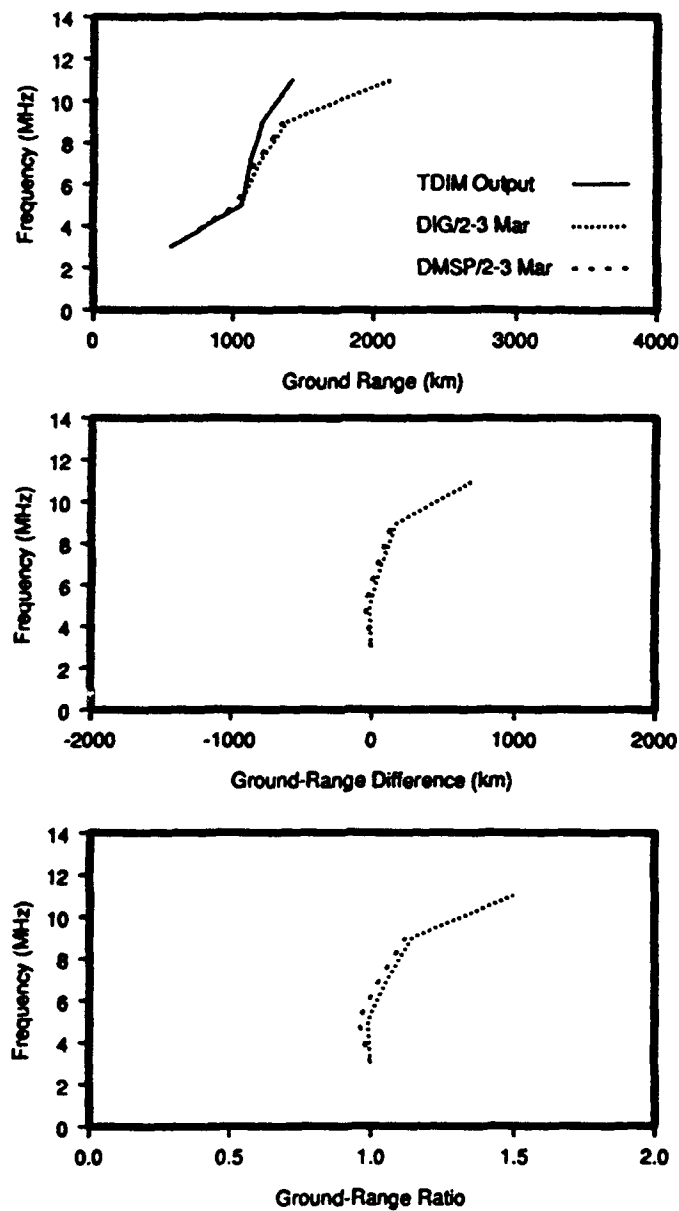


Fig. 46. Ray-tracing results of ground-range tests from the first experimental period for a range of frequencies (3.0-13.0 MHz) at a fixed elevation angle (25.0°) and an azimuth of 53.5° .

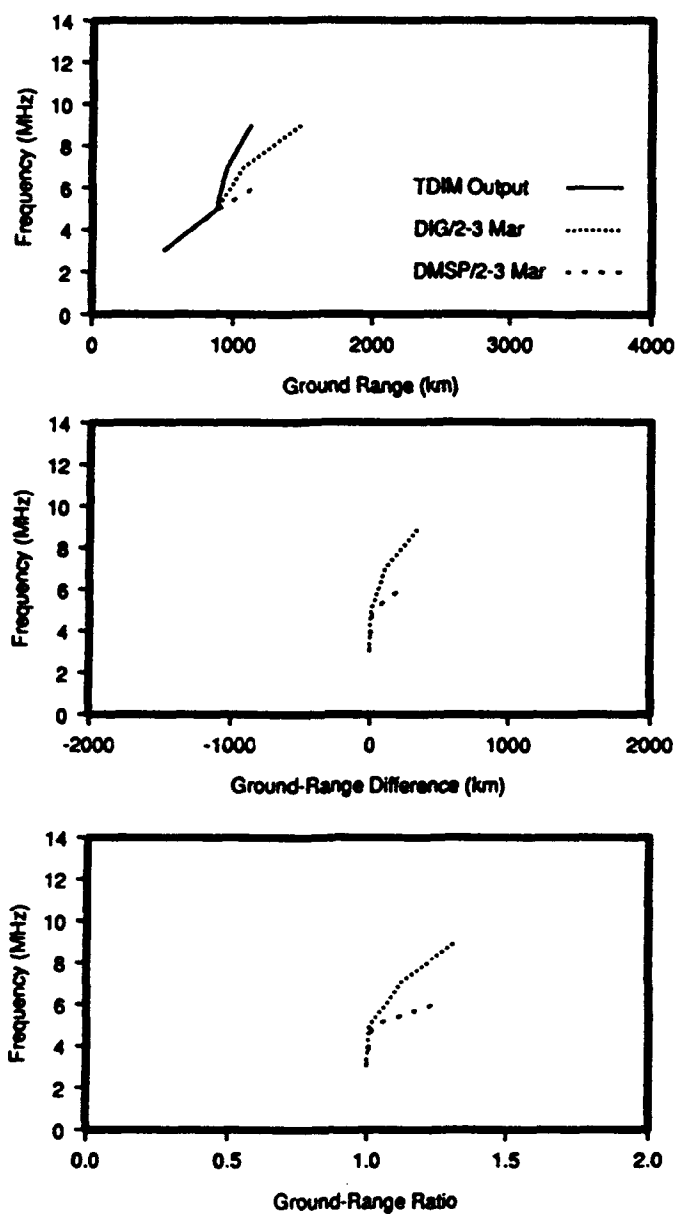


Fig. 47. Ray-tracing results of ground-range tests from the first experimental period for a range of frequencies (3.0-13.0 MHz) at a fixed elevation angle (30.0°) and an azimuth of 40.0° .

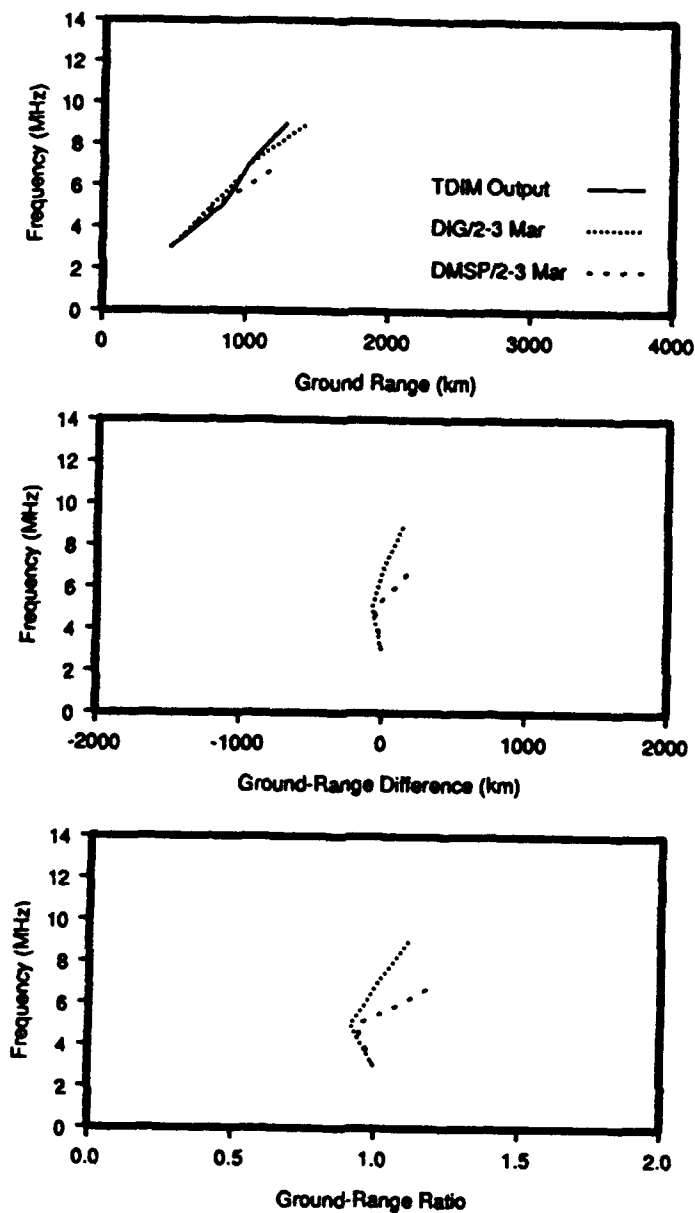


Fig. 48. Ray-tracing results of ground-range tests from the first experimental period for a range of frequencies (3.0-13.0 MHz) at a fixed elevation angle (30.0°) and an azimuth of 0.0° .

trapped, or they penetrated the entire ionosphere. I instead used elevation angles about five to seven degrees higher than those that exhibited the largest ground-range differences for the earlier fixed-frequency tests (at each azimuth). As a result, the threshold required for trapping shifted to higher frequencies (9.0-13.0 MHz instead of 6.0 MHz), and ground ranges were available to compare with the corresponding TDIM values.

All four azimuths showed little or no difference in ground range between the TDIM rays and the corresponding digisonde and DMSP rays at frequencies up to 5.0 MHz. Above 5.0 MHz, however, the ground-range values started to diverge, with the digisonde and DMSP values exceeding the TDIM values by an increasing amount as frequency increased. The largest differences were at the highest frequency for each azimuth. Increasing the frequency beyond this value caused the ray to become trapped, or to fully penetrate the ionosphere. Ground-range differences were largest for the highest azimuth (63.0°). The differences decreased substantially as the azimuth was shifted into the trough at more direct angles to the equatorward wall. This was partially because more rays got trapped or penetrated for the azimuths 53.5° and 40.0° , making them unavailable for ground-range difference comparisons. Also, the frequency threshold for trapping or penetration shifted to lower frequencies for lower azimuths. The lower-azimuth rays were aimed deeper into the weak vertical gradients of the trough base, causing them to penetrate or get trapped at lower frequencies than at higher azimuths.

Very little difference existed between the ground-range test results for the digisonde and DMSP troughs at azimuths 63.0° and 53.5° in Figures 45 and 46, but a fairly large difference existed for azimuths 40.0° and 0.0° at the higher frequencies of Figures 47 and 48. The smaller differences at the two higher azimuths was a result of the elevations angles chosen. At these elevation angles, the ray paths encountered nearly identical vertical gradients as they refracted through similar regions of the digisonde and DMSP trough depictions. As shown by the fixed-frequency tests on Figures 37 and 38, the range of elevation angles that allowed substantial variation between ground-range results from the digisonde and DMSP trough representations was quite small at these two azimuths, especially at 63.0° (Figure 37).

Figure 45 (63.0° azimuth) had the largest ground-range differences between rays from the TDIM and modified trough depictions for the variable-frequency tests. Similarly, Figure 41 (also 63.0° azimuth) had the largest ground-range differences for the fixed-frequency tests, though only for the lowest elevation angles (12.9 - 13.0°). Figure 49 shows a series of ground-range tests similar to the 6.0 MHz fixed frequency test in Figure 41. However, in Figure 49, ground range was plotted for variable elevation angles at a constant frequency of 10.0 MHz. Again, the largest ground-range differences between rays from the TDIM troughs and the more realistic digisonde troughs were at the lowest elevation angles. However, the largest ground-range differences for the higher frequency in Figure 49 spanned a greater range of elevation angles (16.4 - 20.0°) than the narrow

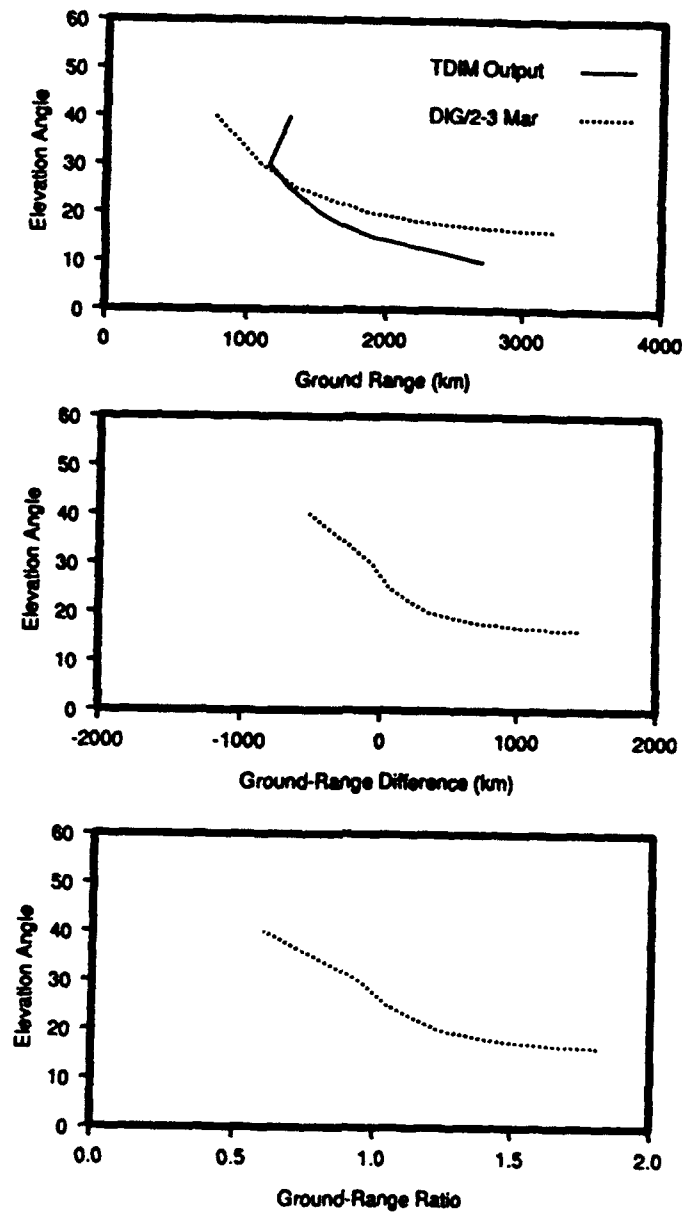


Fig. 49 Ground-range difference and ground-range ratio for ray-tracing test results from the first experimental period at a fixed frequency of 10.0 MHz and an azimuth of 63.0° .

elevation-angle range (12.9-13.0°) from Figure 41. Thus, increasing the ray frequency caused the range of elevation angles that experienced the largest ground-range differences to increase and shift to higher elevation angles.

The rays which propagated through the digisonde trough depiction (digisonde rays) were able to progress farther in ground range at the higher frequency, because they penetrated higher into the ionosphere before refracting back towards the surface. The TDIM rays landed at nearly identical ground ranges at the two frequencies (6.0 and 10.0 MHz) at elevation angles below about 27°.

The large, but opposite ground-range difference that occurred above the 27° elevation-angle ray on Figure 49 was caused by a partial trapping of the 30.0-40.0° elevation-angle rays through the TDIM output, thereby delaying their landing and increasing the ground range. All TDIM rays at elevation angles of 41.0° and above penetrated. The 40.0° elevation-angle ray through the TDIM output nearly missed becoming a trapped ray, or penetrating entirely.

CHAPTER VI

EFFECTS OF THREE-DIMENSIONAL GRADIENTS IN ELECTRON
DENSITY ON RADIO-WAVE PROPAGATION
IN THE TROUGH REGION*Overview*

The ray-tracing test results from Chapter V revealed the extent of the ground-range errors introduced when ray-tracing simulations were performed through the TDIM output, the most realistic model representation of the mid-latitude trough currently available. The Chapter V results also demonstrated that ray propagation through the trough base is often complicated by the tendency for the rays to get trapped or penetrate, thereby never reaching the earth's surface. The rays that were trapped, penetrated, or delayed during descent occurred most often at the lowest elevation angles for the transmitter site and trough representations used in this study.

The transmitter location represented the OTH-B radar site at Bangor, assuming the digisonde and DMSP trough representations used in the ray-tracing tests were shifted about five degrees of latitude equatorward. I purposely chose this orientation to allow the low elevation-angle rays to refract in the trough equatorward wall and trough base. This orientation of the OTH-B radar with respect to the trough is likely a common occurrence, especially for periods of high magnetic activity. Thus, the Bangor OTH-B radar likely encounters these same problems when transmitting through the trough during enhanced magnetic periods.

One of the primary goals in this study is to determine the sensitivity of high-

frequency radio propagation to realistic trough electron-density gradients. As stated in Chapter II, gradients in all three spatial dimensions are capable of influencing the ray along its path through the ionosphere. Vertical gradients cause the ray to refract in the vertical plane, thereby affecting the ray's ground range (if it lands). Weak vertical gradients allow the ray to get trapped or penetrate. The vertical electron-density gradient usually dominates the two horizontal gradients along the ray path. The amount of refraction depends on three factors: the strength of the component of the electron-density gradient perpendicular to the ray path (the cross-gradient component), the value of the normalized electron density X from equation (2), and the distance (in group path) the gradient affects the ray. Low elevation-angle rays experience a larger deviation for a given strong cross-gradient component and large X value, since they travel farther in group path through the ionosphere.

Substantial horizontal deviations are possible only for a limited range of ray orientations with respect to the proper trough conditions. As discussed in Chapter II, rays which are obliquely incident (within a critical angle) to strong horizontal electron-density gradients, as found in a steep trough wall, may deviate sharply from their original ray paths without penetrating the steep wall (as in Figure 6). Such a horizontal deviation is called a total internal reflection, and this may cause the ray to land up to 400 km from its intended landing point [Buchau *et al.*, 1973]. Rays which are incident to strong latitudinal electron-density gradients at angles outside the critical-angle range may also deviate horizontally as they refract in response to the strong horizontal cross gradients, though not as much as for rays

which experience total internal reflection.

I had to neglect small-scale fluctuations of electron density in this study. This prevented me from investigating the possibility that strong horizontal gradients at a smaller scale, such as those characteristic of plasma irregularities, are also capable of causing large horizontal ray-path deviations. Small-scale plasma irregularities at trough latitudes arise from plasma-instability processes associated with high auroral-energy inputs, which are not possible to model accurately at this time.

Methodology

In this chapter, I examined some of the more extreme cases of ground-range differences from Table 6 in greater detail. The *Huffines* [1990] modification of the *Jones and Stephenson* [1975] ray-tracing program calculated the three spatial components of the electron-density gradient from the ionospheric model output in small, variable step lengths along the ray path. The three spatial components of the gradient were with respect to altitude, magnetic latitude, and magnetic local time. The program calculated the components of the electron-density gradients with respect to the normalized electron density (X , as defined in equation (2)), so the normalized units were km^{-1} . Density units canceled when the square of the plasma frequency was divided by the square of the wave frequency. I examined ray-propagation conditions for rays with the largest ground-range differences from Table 6 for the first experimental period, so the differences in the vertical gradient along the rays path could be identified. To do this, I plotted the three normalized

electron-density gradient components, along with the normalized electron density (X values), approximately every 50 km of group path for rays through the TDIM trough output and the corresponding rays through the digisonde and DMSP trough representations. I excluded ray paths at 0.0° azimuth, since no large ground-range differences existed at this azimuth.

Large Ground-Range Differences

For the rays at a fixed frequency of 6.0 MHz and an azimuth of 63.0° , the largest ground-range differences (with respect to rays through the TDIM trough) for rays through the digisonde and DMSP trough depictions occurred at elevation 12.9° (as listed in Table 6). Figure 50 shows the ionospheric conditions along the ray path for the three rays. The top four panels show values of normalized electron density (X) and the three spatial components of the normalized electron-density gradient, plotted approximately every 50 km of group path for each ray. The ray-tracing program calculated the gradients by differentiating X along the ray path. All three gradients were plotted in normalized units of km^{-1} . The gradient axes span from -1.0 to $+1.0 \times 10^{-2} \text{ km}^{-1}$, with tick marks every $2.5 \times 10^{-3} \text{ km}^{-1}$. The bottom panel shows a vertical profile of the ray path (altitude versus ground range in km), with the altitude scale reduced by approximately 1/10 relative to the ground-range scale. Only values above 100 km altitude were plotted, so the actual transmission and ray-landing points are not shown on this depiction. The ground-range scales are identical for all five plots on Figure 50, so the normalized electron-density values and gradients can be determined at the different altitudes

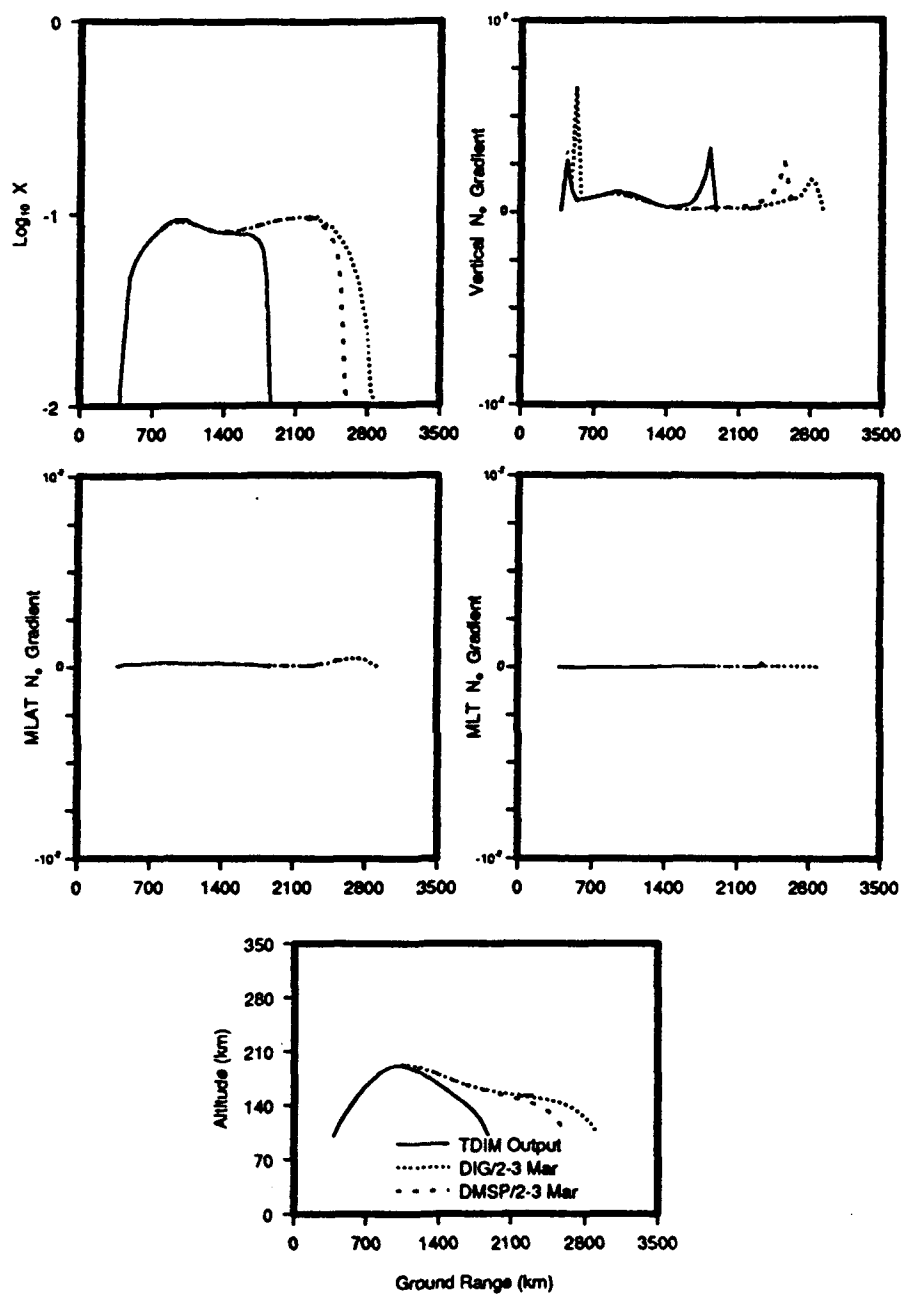


Fig. 50. $\text{Log}_{10} X$ and the three-dimensional gradients of electron density along the ray path (63.0° azimuth, 12.9° elevation, and 6.0 MHz frequency).

of the ray paths shown.

The ray that propagated through the TDIM output (the TDIM ray) from Figure 50 landed at a ground range of 2243 km, whereas the digisonde and DMSP rays landed at ground ranges of 3866 and 3073 km (ground-range ratios of 1.72 and 1.37), respectively. On Figure 50, the vertical electron-density gradient was the only factor which changed appreciably along the ray paths (with the exception of electron density (X), which drastically increased and decreased as the rays entered and left the F region, respectively). The two horizontal electron-density gradients were relatively weak throughout the ray trajectories, so horizontal ray-path deviations were assumed to be negligible. In the following pages, I explain the changes of electron-density values and gradients along the ray paths in detail. The important results are summarized later in the chapter.

The vertical gradient along the TDIM ray path (about 250 km in ground range on either side of the 191 km apogee) ranged from 5.3×10^{-4} to $1.1 \times 10^{-3} \text{ km}^{-1}$ at about 800-1300 km ground range (180-190 km altitude), approximately 9-14% higher than that for the digisonde and DMSP rays. The X values for the three rays were similar (0.08-0.09). The slightly stronger vertical gradients caused the TDIM ray to refract downward from apogee slightly more than the digisonde and DMSP rays. At a ground range of about 1700 km (132 km altitude), the TDIM ray refracted sharply towards the surface, as the vertical gradient quickly rose from 4.3×10^{-4} to $3.3 \times 10^{-3} \text{ km}^{-1}$. X was about 0.05-0.07.

From 1500-2100 km ground range, the vertical gradients for the digisonde and DMSP rays were only about $1.4\text{-}3.0 \times 10^{-4} \text{ km}^{-1}$, causing them to make a slow

descent from apogee. Beyond a ground range of about 2370 km (138 km altitude), the DMSP ray started to descend as the vertical gradient rose from 6.4×10^{-4} to $2.6 \times 10^{-3} \text{ km}^{-1}$ at 2550 km ground range (121 km altitude). X ranged from 0.05 to 0.08. At this point, the digisonde ray was still descending slowly, because the vertical gradient was relatively small ($3.5\text{-}5.8 \times 10^{-4} \text{ km}^{-1}$). The digisonde ray finally started to descend more rapidly at a ground range of about 2600 km (140 km altitude), as the vertical gradient rose from 7.2×10^{-4} to $1.1 \times 10^{-3} \text{ km}^{-1}$ at 2800 km ground range (132 km altitude). X ranged from 0.04 to 0.06. The two vertical-gradient enhancements below 700 km ground range occurred early in the ray's trajectories (well before apogee), and the value of X was too small (0.02-0.06) to allow the rays to refract downward substantially.

In Figure 50, the sharp vertical-gradient enhancements occurred late in the ray paths. The digisonde and DMSP rays would likely have been trapped without them, but the TDIM ray was already committed to land, due to its slightly higher vertical gradient near apogee. The effect of the late vertical-gradient enhancement at 1700 km ground range was to bring the TDIM ray down to the surface about 800 km closer in ground range.

Figure 51 shows 53.5° azimuth rays at a fixed frequency of 6.0 MHz and an elevation of 18.7° . The TDIM ray landed at a ground range of 1532 km, while the digisonde ray landed at 2221 km, a ground-range ratio of 1.45. The DMSP ray was trapped. Vertical gradients controlled the vertical refraction of the rays, especially at ray apogee (near 205 km altitude). The two horizontal gradients were again negligible.

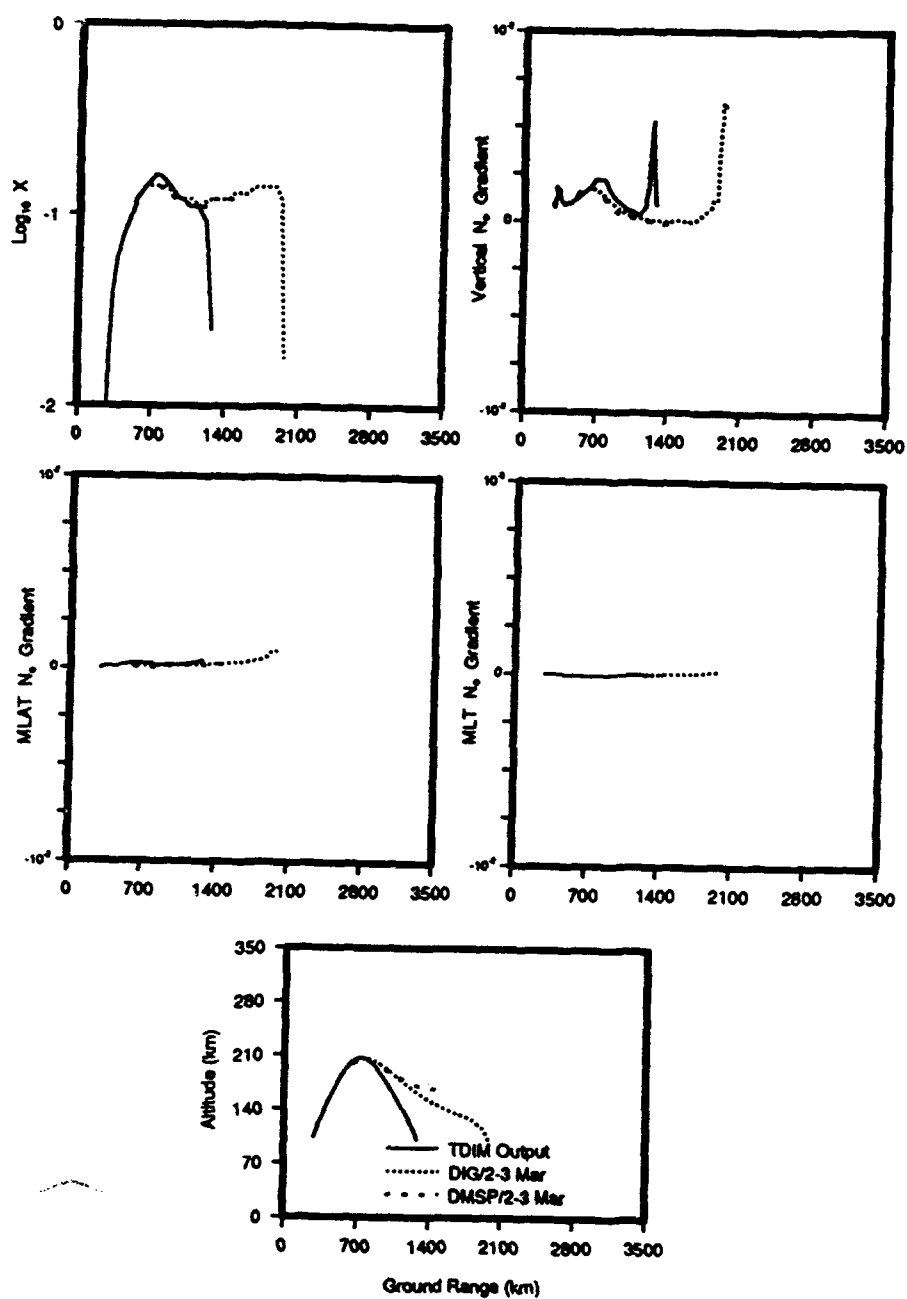


Fig. 51. $\text{Log}_{10} X$ and the three-dimensional gradients of electron density along the ray path (53.5° azimuth, 18.7° elevation, and 6.0 MHz frequency).

The TDIM ray encountered enhanced vertical gradients relative to the other two rays, as in Figure 50. Starting at 445 km ground range (157 km altitude), the TDIM ray refracted downwards rapidly as the ray-path vertical gradient rose from 1.0 to $2.2 \times 10^{-3} \text{ km}^{-1}$ at 685-776 km ground range (205-207 km altitude). X ranged from 0.08 to 0.16. Though the TDIM vertical gradient reached $5.3 \times 10^{-3} \text{ km}^{-1}$ near 1258 km ground range (110 km altitude), the value of X was small (< 0.05), and the ray was already descending rapidly, so there was no large effect.

Just after apogee, the digisonde ray encountered vertical gradients about 27-40% weaker than those experienced by the TDIM rays from 700 to 1000 km ground range (206-190 km altitude), thereby slowing its descent. The DMSP ray experienced even weaker vertical gradients (27-66% weaker than for the TDIM ray) at the same ground range and altitude. The values of X were high (0.12-0.14) for both rays. By the time the DMSP ray reached 1200 km ground range (175 km altitude), it encountered weak negative vertical gradients ($-6.0 \times 10^{-6} \text{ km}^{-1}$), which had strengthened to $-1.2 \times 10^{-4} \text{ km}^{-1}$ by the time the ray became trapped at 1600 km ground range (166 km altitude). The digisonde ray continued its slow descent from apogee through weak vertical gradients ($7.5 \times 10^{-4} \text{ km}^{-1}$ or less) until it reached a ground range of 1839 km (126 km altitude). At this point, the vertical gradient rose to $1.2 \times 10^{-3} \text{ km}^{-1}$, to eventually peak at $6.3 \times 10^{-3} \text{ km}^{-1}$ at 1930 km ground range (114 km altitude). This late vertical-gradient enhancement accelerated the digisonde ray's descent, because X was still large (0.12).

The ground-range difference between the TDIM and digisonde rays in

Figure 51 was mainly due to the vertical-gradient differences near and just after ray apogee. The late vertical-gradient enhancement at 1930 km ground range reduced the difference by forcing the digisonde ray to descend rapidly to the surface.

Figures 50 and 51 differed in one interesting respect. On Figure 51, the rays descended into enhanced E-region electron densities (near 10^4 cm^{-3}), due to the presense of the TDIM-simulated auroral oval at the higher latitude reached by the 53.5° azimuth rays. The enhanced E-region densities caused the negative vertical gradients experienced by the DMSP ray as it became trapped between the E- and F-region peak altitudes of electron density. Negative vertical gradients will be discussed later in this chapter.

The 40.0° azimuth digisonde ray on Figure 52 (elevation 25.4° , frequency 6.0 MHz) propagated farther poleward than the 53.5° azimuth DMSP ray during its descent, thereby encountering the enhanced auroral-E region at even higher electron densities. High E-region densities helped to increase the ground-range difference between the TDIM and digisonde rays. The TDIM ray landed at a ground range of 1084 km, while the digisonde ray landed at 1476 km (a ground-range ratio of 1.36), and the DMSP ray penetrated. The high E- and lower F-region electron densities led to high X values over most of the three ray paths at 40.0° azimuth. After the three rays reached 342 km ground range, X ranged from 0.10 to 0.25, allowing the various vertical-density enhancements to refract the rays.

Vertical gradients once again dominated the ray-path refraction; horizontal gradients were weak. The TDIM ray encountered strong positive vertical gradients

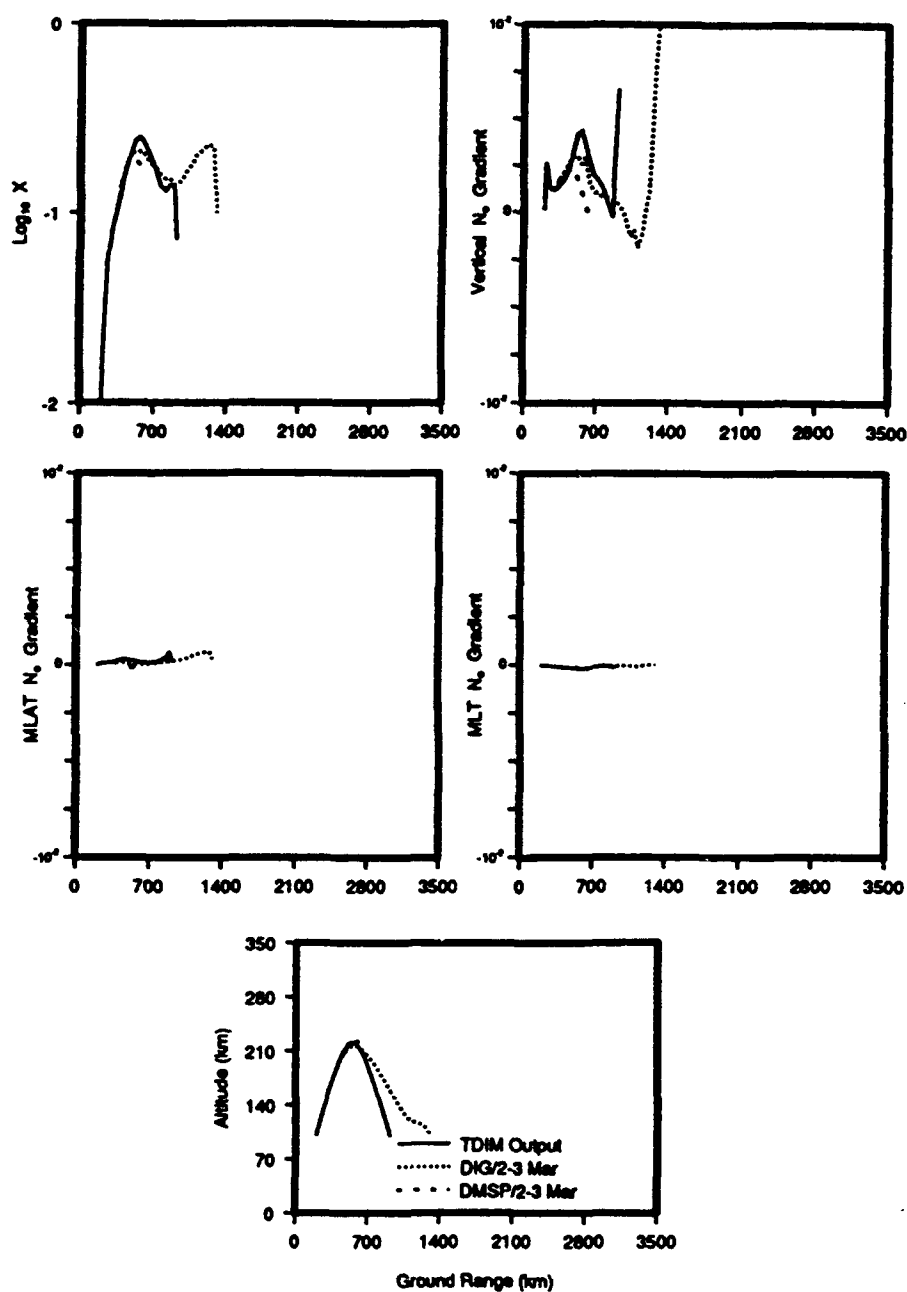


Fig. 52. $\text{Log}_{10} X$ and the three-dimensional gradients of electron density along the ray path (40.0° azimuth, 25.4° elevation, and 6.0 MHz frequency).

over almost the entire ray path, leading to its rapid descent. The vertical gradient consistently exceeded $1.3 \times 10^{-3} \text{ km}^{-1}$, starting early in the ray's ascent at 342 km ground range (166 km altitude) and ending late in the ray's descent at 760 km ground range (168 km altitude). It reached a peak of $4.4 \times 10^{-3} \text{ km}^{-1}$ at the TDIM ray's apogee (562 km ground range, 222 km altitude). The smaller, early vertical-gradient peak at 224 km ground range and the larger, late peak at 920 km ground range had negligible effects on ray refraction; they both occurred at a low altitude ($< 115 \text{ km}$). The first peak occurred early, and X was too small (0.02) to allow the ray to refract much downward. By the time the later peak occurred (reaching $6.6 \times 10^{-3} \text{ km}^{-1}$), the ray was already descending rapidly towards the surface.

The digisonde ray experienced vertical gradients ($2.1\text{-}3.0 \times 10^{-3} \text{ km}^{-1}$) that were about 24-41% weaker than the corresponding TDIM vertical gradients from 500 to 600 km ground range (centered around the 217 km apogee of the digisonde ray). This caused the digisonde ray to undergo weaker refraction near apogee, so it descended at a more gradual pace than the TDIM ray. At about 978 km ground range (145 km altitude), the digisonde ray encountered negative vertical gradients, which reached a negative peak of $-1.9 \times 10^{-3} \text{ km}^{-1}$ at 1103 km ground range (122 km altitude). As a result, the digisonde ray leveled out for about 200 km ground range before it encountered strong positive vertical gradients ($> 1.5 \times 10^{-3} \text{ km}^{-1}$) at 1226 km ground range (114 km altitude), which forced the ray towards the surface again. The vertical gradient switched from negative to positive as the digisonde ray descended below the E-region peak electron density.

The DMSP ray encountered vertical gradients similar to the other two rays for ground ranges up to 523 km (216 km altitude). However, after the ray reached 600 km ground range (220 km altitude), the vertical gradients decreased sharply (below $3.0 \times 10^{-4} \text{ km}^{-1}$), allowing the ray to penetrate at 225 km altitude.

Frequency Variation Effects

All the raytracing cases examined in this chapter thus far were for a fixed frequency of 6.0 MHz. The next two figures show results for an increase in frequency from 6.0 to 11.0 MHz. As found in Chapter V, a frequency increase (all other parameters remaining the same) caused a larger ground-range difference between rays through the TDIM trough depiction and the corresponding digisonde or DMSP trough representations.

Figure 53 shows TDIM and DMSP rays at azimuth 63.0° , elevation 10.0° , and frequency 6.0 MHz. This case differs from the previous cases in that the DMSP ray landed at a closer ground range (3267 km) than the corresponding TDIM ray (4086 km), a ground-range ratio of 0.80. The early vertical-gradient enhancement ($2.7 \times 10^{-3} \text{ km}^{-1}$) at 534 km ground range (117 km altitude) caused both rays to refract slightly, but not enough to turn towards the ground, since X was small (0.02-0.05). After this early peak, both rays encountered weak vertical gradients ($< 5.6 \times 10^{-4} \text{ km}^{-1}$) from 700-1700 km ground range. However, as the TDIM ray rose above 170 km, the value of X increased to 0.08-0.09, and the vertical gradients were strong enough ($4.0\text{-}5.4 \times 10^{-4} \text{ km}^{-1}$) to level out the TDIM ray from 1400 to 1750 km ground range. The DMSP ray experienced slightly

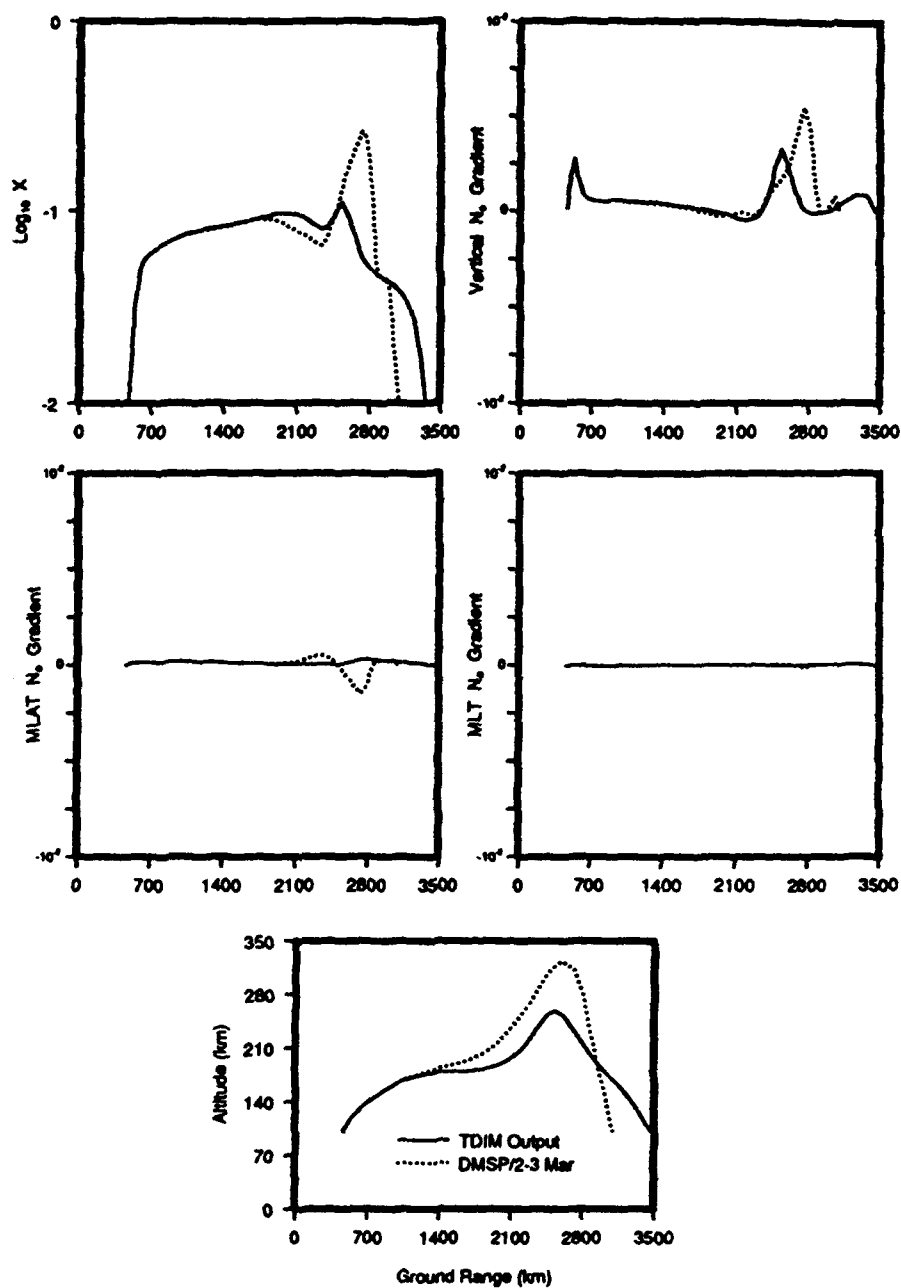


Fig. 53. $\text{Log}_{10} X$ and the three-dimensional gradients of electron density along the ray path. (63.0° azimuth, 10.0° elevation, and 6.0 MHz frequency).

weaker gradients ($1.1\text{--}4.6 \times 10^{-4} \text{ km}^{-1}$), allowing it to continue upward as the TDIM ray had leveled off.

The DMSP ray encountered weak negative vertical gradients (from -1.6 to $-2.6 \times 10^{-4} \text{ km}^{-1}$) and relatively high X values (0.08-0.09) at 1842-2258 km ground range (204-264 km altitude), and as a result, refracted upward. The TDIM ray also refracted upwards from 1978-2337 km ground range (188-231 km altitude), as it also encountered weak negative vertical gradients (-1.2 to $-4.5 \times 10^{-4} \text{ km}^{-1}$) and high X values (0.08-0.10). As the TDIM ray continued to climb, it experienced strong positive vertical gradients ($> 1.3 \times 10^{-3} \text{ km}^{-1}$) and high X values (0.09-0.11) from 2439-2656 km ground range (246-259 km altitude), reaching its strongest vertical gradient ($3.3 \times 10^{-3} \text{ km}^{-1}$) at apogee (259 km). The DMSP ray climbed higher than the TDIM ray, eventually reaching stronger vertical gradients ($> 2.1 \times 10^{-3} \text{ km}^{-1}$) and higher X values (0.12-0.26). Though the DMSP ray reached a higher apogee than the TDIM ray, the stronger vertical gradients and higher X values caused the DMSP ray to descend more rapidly and land 819 km closer in ground range.

Figure 54 shows the same TDIM and DMSP rays as in Figure 53 (azimuth 63.0° , elevation angle 10.0°), except the frequency has been increased to 11.0 MHz. The frequency increase markedly changed both rays, though the ground range changed substantially only for the TDIM ray, which landed at a 31% shorter ground range (2809 km) than at 6.0 MHz (4086 km). The ground range of the DMSP ray increased only about 10% (3608 km), though the vertical profile of the ray path was substantially different.

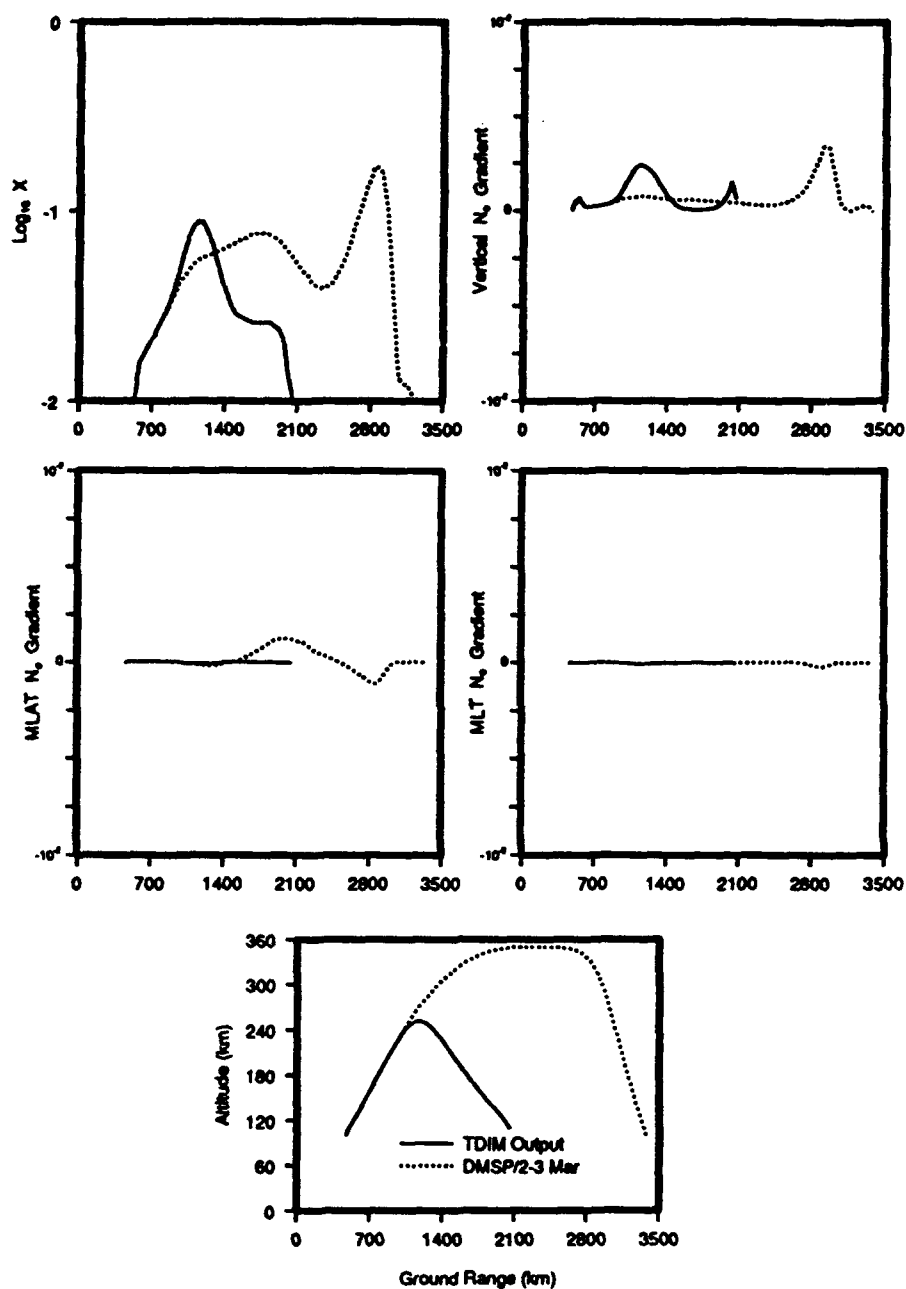


Fig. 54 $\text{Log}_{10} X$ and the three-dimensional gradients of electron density along the ray path (63.0° azimuth, 10.0° elevation, and 11.0 MHz frequency).

At 11.0 MHz, neither ray experienced negative vertical gradients throughout their ray paths. Since the frequency had increased 5.0 MHz, the rays did not encounter the early vertical-gradient enhancement ($2.7 \times 10^{-3} \text{ km}^{-1}$) at 534 km ground range (117 km altitude), which caused the 6.0 MHz rays to level off. The higher frequency caused the rays to experience lower X values (0.01-0.02) than at 6.0 MHz (0.02-0.05), thereby also reducing the vertical gradients ($2.4\text{-}6.8 \times 10^{-4} \text{ km}^{-1}$). This allowed the rays to penetrate higher into the F region (missing the negative vertical-gradient region), to eventually encounter stronger positive vertical gradients and higher X values. The TDIM ray encountered strong vertical gradients ($>1.5 \times 10^{-3} \text{ km}^{-1}$) at 1000-1300 km ground range (233-252 km altitude), reaching its strongest vertical gradient ($2.4 \times 10^{-3} \text{ km}^{-1}$) at apogee (252 km). X ranged from 0.06 to 0.09. As a result, the TDIM ray refracted rapidly towards the surface. The DMSP ray continued upward beyond the TDIM apogee, because it continued to encounter weak vertical gradients ($2.9\text{-}7.5 \times 10^{-4} \text{ km}^{-1}$). However, as the ray climbed from 252 to 340 km, the values of X increased from 0.05 to 0.08, allowing the weak vertical gradients to refract the ray enough to level it out near the 350 km apogee. As the ray descended from 342 to 294 km altitude (2750-2965 km ground range), the vertical gradient increased to $1.4\text{-}3.4 \times 10^{-3} \text{ km}^{-1}$ and X increased to 0.10-0.17, causing the ray to refract rapidly towards the surface.

Negative Vertical Electron-Density Gradients

The rays in Figure 53 are unique in this study in the sense that strong negative vertical gradients caused the rays to refract rapidly upwards after they

had leveled off in altitude. The TDIM ray in Figure 53 provides a good example of the complications of ray refraction caused by the presense of enhanced auroral E-region electron densities. Figure 55 shows altitude profiles of electron density along the TDIM ray path. At 201 km altitude, the TDIM ray encountered a negative vertical gradient of $-4.0 \times 10^{-4} \text{ km}^{-1}$. The top panel of Figure 55 shows the electron-density altitude profile for the location of the ray at 201 km altitude (61.3° MLAT, 2306 MLT). The ray was in a region of decreasing electron density with height (a negative vertical gradient), which occurs at altitudes just above the E-region electron-density peak ($N_m E$). This situation will also occur if $N_m E$ exceeds $N_m F$, except negative vertical gradients will exist at all altitudes above the E-peak. At 255 km altitude, the TDIM ray experienced a strong positive vertical gradient of $2.1 \times 10^{-3} \text{ km}^{-1}$. The bottom panel of Figure 55 similarly shows the electron-density altitude profile for the ray location at 255 km altitude (60.6° MLAT, 2330 MLT). The ray was in a region of increasing electron density with height.

Conditions Required for Vertical Ray Refraction to Surface

Table 7 lists the ranges of vertical gradients, X values, and group path for the various vertical refractions which caused a ray to return to the surface. The group-path range refers to the distance the gradient range existed for the ray path. Most vertical gradients listed occurred near the ray apogee. For these, altitude range (Alt) is listed in ascending order. The asterisks on five of the altitude ranges refer to those vertical gradients that occurred as a late enhancement (altitude range listed in descending order), causing a relatively trapped ray to

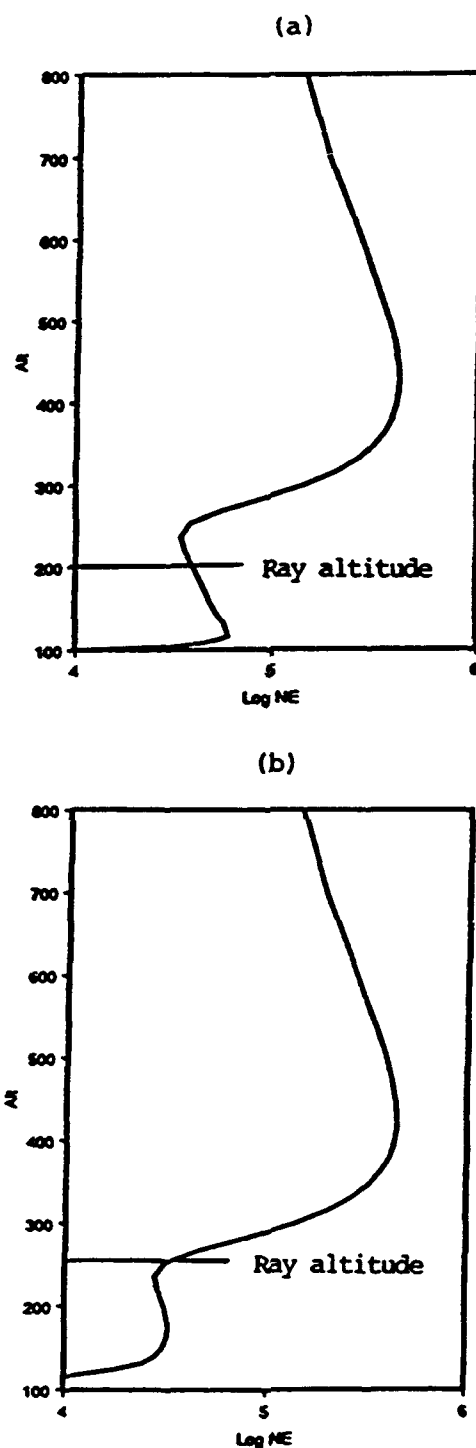


Fig. 55. Altitude profiles of $\log_{10} N_e$ (cm^{-3}) along the TDIM ray path from Figure 53. The top panel shows the ray experienced a negative vertical electron-density gradient at 201 km altitude. The bottom panel shows the ray experienced a strong positive gradient at 255 km altitude.

TABLE 7. Conditions For Vertical Ray Refraction to Surface

Trough	Az	El	Fr (MHz)	Group Path (km)	Alt (km)	Vertical Gradient (10^{-3} km^{-1})	X
TDIM	63.0	12.9	6.0	200	184-191	1.0-1.1	0.09
DIG	63.0	12.9	6.0	272	140-113*	0.7-1.7	0.02-0.06
DMSP	63.0	12.9	6.0	146	132-109*	1.0-2.6	0.04-0.07
TDIM	53.5	18.7	6.0	528	157-207	1.0-2.2	0.08-0.16
DIG	53.5	18.7	6.0	424	157-206	1.0-1.7	0.08-0.14
DIG	53.5	18.7	6.0	152	126-101*	1.2-6.3	0.12-0.14
TDIM	40.0	25.4	6.0	504	166-222	1.4-4.4	0.10-0.25
DIG	40.0	25.4	6.0	360	166-217	1.5-3.0	0.10-0.21
DIG	40.0	25.4	6.0	60	114-109*	1.5-7.6	0.22-0.23
TDIM	63.0	10.0	6.0	240	246-259	1.3-3.3	0.07-0.11
DMSP	63.0	10.0	6.0	348	274-324	1.6-5.5	0.12-0.26
TDIM	63.0	10.0	11.0	306	233-252	1.5-2.4	0.06-0.09
DMSP	63.0	10.0	11.0	240	232-294*	1.4-3.4	0.10-0.17

descend to the surface. At 53.5° and 40.0° azimuth, the digisonde ray required two vertical-gradient enhancements to bring it down to the surface, one near the apogee, and the other late in the ray path. At 63.0° azimuth, the digisonde and DMSP rays would likely have been trapped if it were not for the late vertical-gradient enhancement. In all cases, the TDIM ray was able to reach the surface

due to relatively strong vertical gradients near the ray apogee. The DMSP and digisonde rays encountered weaker vertical gradients near apogee, and required the later enhancement to cause the ray to refract to the surface.

The conditions near apogee which refracted the ray enough to reach the surface varied with azimuth and elevation angle, but generally the ray was subjected to vertical gradients of at least $1.0 \times 10^{-3} \text{ km}^{-1}$ for several hundred km of group path at X values exceeding 0.05. In the cases where the conditions near ray apogee were not sufficient to cause the ray to refract enough to reach the surface, either the vertical gradient or the X value did not reach these values, or both. Usually these rays did refract enough to level out in altitude or descend gradually. Those rays which encountered a vertical-gradient enhancement during descent (late enhancement) were able to reach the ground. Trapped rays did not encounter a late enhancement. The late vertical-gradient enhancements typically occurred at E-region altitudes (with one exception) and were stronger at 53.5° and 40.0° azimuth, where the ray descended below the peak electron density of the aurorally-enhanced E region.

Vertical gradients on the order of 10^{-4} km^{-1} were strong enough to cause slight ray refraction if X exceeded 0.05 for several hundred km of group path. Of all the rays examined from Table 7, the digisonde ray at 63.0° azimuth, 12.9° elevation angle, and 6.0 MHz frequency (from Figure 50) experienced the weakest conditions during a significant refraction. The late vertical-gradient enhancement ranged from 7.0×10^{-4} to $1.7 \times 10^{-3} \text{ km}^{-1}$ for 272 km of group path at X values of

0.02-0.06, causing the ray to refract enough from a gradual descent to deviate towards the surface.

Horizontal Ray Deviations

The strong latitudinal gradients in the DMSP trough representations provided the opportunity to determine the amount of horizontal deviation experienced by rays which passed through the trough-wall gradients at oblique incidence. The DMSP rays from Figures 53 and 54 experienced stronger latitudinal electron-density gradients than did previous cases. Since these rays were at 63.0° azimuth, they were incident to the strong equatorward-wall gradients at a relatively oblique angle (bottom panel of Figure 36). The DMSP ray in Figure 54 experienced the stronger latitudinal gradients of the two cases. As the ray passed through the equatorward wall, it encountered strong positive latitudinal gradients ($1.0\text{-}1.3 \times 10^{-3} \text{ km}^{-1}$) and moderate X values (0.05-0.07) from 1846-2160 km ground range (344-350 km altitude). As the ray continued to propagate slightly poleward, it moved across the narrow trough base into the poleward wall. In the poleward wall, the ray encountered fairly strong negative latitudinal gradients (-9.0×10^{-4} to $-1.1 \times 10^{-3} \text{ km}^{-1}$) and high X values (0.13-0.17) from 2780-2910 km ground range (339-314 km altitude, during descent).

Figure 56 shows the ground projection of the ray path in MLAT-MLT coordinates. The ray deviated about 165 km poleward of the straight-line path (measured at the ray landing point), as a result of the enhanced positive latitudinal gradients it experienced in the equatorward wall just before ray apogee. The ray

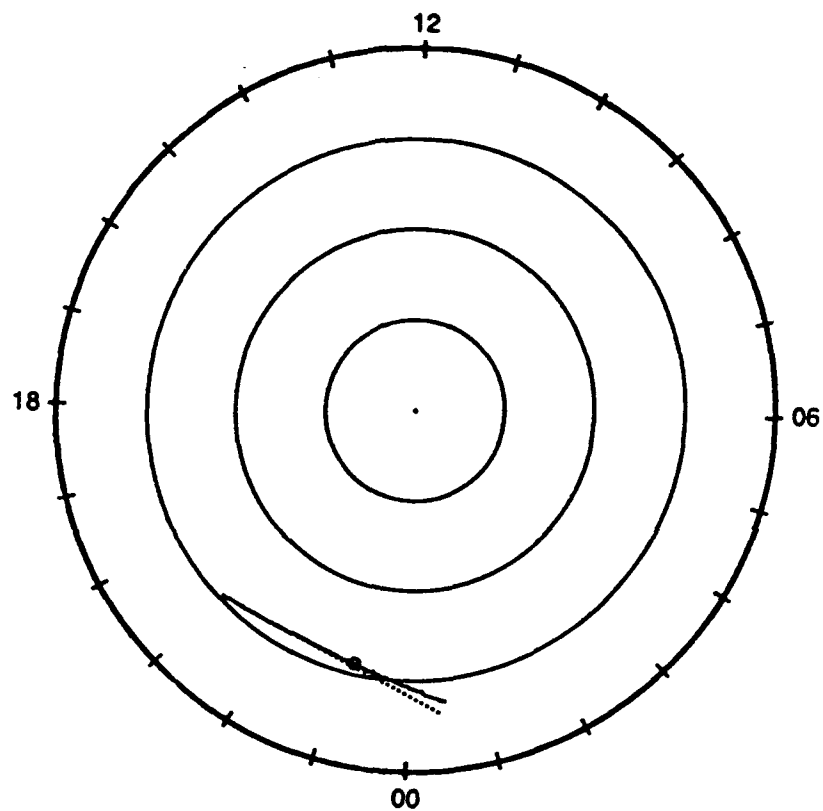


Fig. 56. Ground projection of the ray path from Figure 54 (solid line) in MLAT-MLT coordinates. This ray path deviated about 165 km poleward from the straight-line path (dotted line) in response to strong latitudinal gradients in the trough equatorward wall.

also experienced a negative latitudinal-gradient enhancement in the poleward wall after ray apogee. Since the resultant horizontal deviation was poleward (opposite of the direction of the positive equatorward-wall latitudinal gradients), it was caused by the strong positive gradient enhancement, which occurred earlier in the ray path than the negative gradient enhancement. The negative latitudinal-gradient enhancement was slightly weaker, and thus, likely too weak and too late to fully compensate for the earlier, stronger positive latitudinal-gradient enhancement. It also occurred over a substantially shorter group path.

CHAPTER VII

CONCLUSIONS

A combination of at least three digisonde stations from the high-latitude digisonde network (Goose Bay, Argentia, and Narssarssuaq, Sondrestrom, or Millstone Hill) can provide a realistic large-scale depiction of the trough for weak to moderate geomagnetic conditions on a near-real time basis. Comparisons of trough depictions and latitudinal electron-density profiles from the Millstone Hill incoherent scatter radar and digisonde f_oF_2 measurements for the same time periods showed the digisonde trough depictions were realistic in the large-scale. However, the digisonde depictions were not capable of representing the smaller-scale trough structure specific for the three experimental periods.

The trough representations that result from the digisonde f_oF_2 measurements will usually be realistic throughout the evening sector. The digisonde depictions were not as realistic in the morning sector, because the digisonde stations experienced problems (i.e., E-region blanketing, spread-F) as the trough and auroral oval shifted equatorward. Latitudinal electron-density gradients in the trough walls will likely not be as strong as in reality, because the spatial resolution of the digisonde network is not sufficient to accurately depict narrow trough-wall gradients of a width of about two degrees of latitude or less.

Comparisons of trough depictions from the digisonde data and Time Dependent Ionospheric Model (TDIM) output showed significant differences in trough latitudinal location, depth, width, and horizontal electron-density gradients.

At the medium geomagnetic condition ($K_p = 3.5$), the model underestimated the equatorward trough penetration by two to four degrees of latitude during the first two experimental periods. Latitudinal placement of the trough is especially important for ionospheric models used in conjunction with ray-tracing programs. The TDIM troughs were too shallow and wide, with no appreciable poleward wall in the F region. Typically, the digisonde troughs were about three to ten times deeper, causing the latitudinal electron-density gradients of the trough walls to be up to seven times steeper than those from the model.

The ray-tracing simulations revealed that HF radio-propagation systems, such as the OTH-B radar, are highly sensitive to trough electron-density conditions. The trough has several adverse effects on ray propagation. At the transmitter site used in this study, low elevation-angle rays often penetrated the entire ionosphere if they entered the low electron densities of the digisonde trough base. Rays at slightly-higher elevation angles were trapped by weak vertical electron-density gradients in the trough base. The rays which entered the digisonde trough at elevation angles just above those that got trapped experienced the largest ground-range differences relative to the same rays which propagated through the TDIM output (TDIM rays). These digisonde rays typically landed 200-900 km farther in ground range (differences of 20-50%), though one digisonde ray landed over 1600 km farther in ground range, a 72% difference.

The digisonde and DMSP modifications to troughs from the TDIM output reduced the $N_m F_2$ values and vertical gradients within the trough and increased the $N_m F_2$ values and vertical gradients equatorward of the trough. Digisonde and

DMSP rays at elevation angles below 30-40° (depending on azimuth) reached ray apogee in the trough. Those rays which reached apogee in the equatorward wall encountered weaker vertical gradients relative to the same TDIM rays, and refracted more gradually towards the surface. However, rays which reached apogee in the trough base either got trapped or penetrated the entire ionosphere. Digisonde and DMSP rays at elevation angles above 30-40° reached apogee equatorward of the trough, where stronger vertical gradients refracted them towards the surface earlier than the corresponding rays through the TDIM output. They typically landed 100 km or less closer in ground range, a 5-15% difference.

As a ray was transmitted at more direct azimuths into the trough base (lower azimuths in this study), it encountered the low electron-density values and weak vertical gradients at higher elevation angles, as well as the lower elevation angles. Thus, a ray gets trapped or penetrates for a larger range of elevation angles as the ray enters the trough base at more direct incidence angles to the trough walls.

As the ray frequency was increased from 6.0 to 10.0 MHz for a fixed azimuth and elevation angle, the range of elevation angles also increased for rays which experienced large ground-range differences. The higher-frequency ray was able to penetrate higher in altitude, because the X value decreases with increasing ray frequency for a given electron density (plasma frequency). The rays that did not fully penetrate landed at a farther ground range than at the lower frequency, because they travelled farther in altitude and ground range.

The electron-density values and vertical gradients were most important in

controlling vertical ray refraction near apogee. Generally, if the ray encountered positive vertical gradients of at least $1.0 \times 10^{-3} \text{ km}^{-1}$ and X values exceeding 0.05 for at least 200 km group path, it would refract sharply towards the surface. Rays which did not encounter these conditions near apogee eventually encountered strong enough vertical gradients and X values to level out or descend gradually. If not, they penetrated or were trapped. Vertical gradients on the order of 10^{-4} km^{-1} were sufficient to cause slight refraction if the ray encountered X values above 0.05 for several hundred km of group path.

The vertical electron-density gradient component usually dominated the two horizontal components. Most rays I examined experienced horizontal deviations less than five to ten km. However, I found one ray (63.0° azimuth, 10.0° elevation, 11.0 MHz frequency) which experienced a poleward deviation of about 165 km at its landing point relative to a straight-line ray path. Well before it reached apogee, this ray encountered strong equatorward-wall latitudinal gradients ($1.0\text{-}1.3 \times 10^{-3} \text{ km}^{-1}$) and fairly high X values (0.05-0.07) for about 320 km group path. Though I did not have time to fully investigate the problem of horizontal deviations, they seemed to be the exception, rather than the rule. The longitudinal (MLT) gradient component was always negligible for the cases I examined.

The high occurrence-rate of large ground-range differences was likely the most significant finding in this study. It means that HF radio-propagation system operators almost always encounter large ground-range errors when transmitting through the trough region, if they use an ionospheric model which overestimates electron-density values in the trough.

CHAPTER VIII

RECOMENDATIONS FOR FUTURE STUDY

I did not have sufficient time to investigate the phenomenon of total internal reflection for rays which are incident to a steep trough wall within a specific critical angle. This phenomenon would be the next logical step to investigate for future ray-tracing simulations through realistic digisonde trough depictions. Further tests regarding ground range could also be done for a wider range of frequencies, azimuths, and elevation angles than I used.

During the March 1989 experiment, the Geophysics Lab collected backscatter ionograms from the OTH-B radar signal for the first observational period (J. Buchau, private communication, 1990). Future researchers could use the ray-tracing program to attempt to simulate the backscatter ionograms by ray tracing through the digisonde trough depictions used in this study. The ray would have to be directed at the location of the OTH-B radio-wave apogee (as shown on the backscatter ionogram) at the same transmitter location, frequency, elevation angle, and azimuth used by the OTH-B radar. Such a test would provide an excellent opportunity to examine the ability of the digisonde measurements to produce an accurate trough depiction for use in ray-tracing simulations.

REFERENCES

- Buchau, J., C. P. Pike, and M. Wong, Detailed specification of the arctic ionosphere and an application to three-dimensional raytracing, *Air Force Cambridge Res. Lab. Tech. Rep.*, 73-0726, 1973.
- Buchau, J., B. W. Reinisch, D. N. Anderson, E. J. Weber, and C. Dozios, Polar cap plasma convection measurements and their relevance to the modelling of the high-latitude ionosphere, *Radio Sci.*, 23, 521-536, 1988.
- Budden, K. B., *Radio Waves in the Ionosphere*, Cambridge University Press, Cambridge, U. K., 1961.
- Buonsanto, M. J., J. C. Foster, A. D. Galasso, D. P. Sipler, and J. M. Holt, Neutral winds and thermosphere/ionosphere coupling and energetics during the geomagnetic disturbances of March 6-10, 1989, *J. Geophys. Res.*, 95, 21,033-21,050, 1990.
- Chamberlain, J. W., and D. M. Hunten, *Theory of Planetary Atmospheres*, Academic Press, San Diego, CA, 1987.
- Collis, P. N. and I. Haggstrom, Plasma convection and auroral precipitation processes associated with the main ionospheric trough at high latitudes, *J. Atmos. Terr. Phys.*, 50, 389-404, 1988.
- Dandekar, B. S., *Handbook of Geophysics and the Space Environment*, Air Force Geophysics Laboratory ADA 167000, National Technical Information Services, Springfield, VA, 1985.
- Davies, K., *Ionospheric Radio Propagation*, National Bureau of Standards Monograph 80, U. S. Government Printing Office, Washington, D. C., 1966.
- Davies, K., *Ionospheric Radio Waves*, Blaisdell, Waltham, MA, 1969.
- Davies, K., and C.M. Rush, High-Frequency ray paths in ionospheric layers with horizontal gradients, *Radio Sci.*, 20, 95-110, 1985.
- Dieminger, W., *Radio Wave Propagation*, Advisory Group for Aerospace Research and Development, AGARD Lecture Series XXIX, Technical Editing and Reproduction Ltd., London, U. K., 1968.
- Hargreaves, J. K., *The Upper Atmosphere and Solar-Terrestrial Relations*, Van Nostrand Reinhold, New York, NY, 1979.

- Helms, J. H., and A. D. Thompson, Ray-tracing simulation of ionization trough effects upon radio waves, *Radio Sci.*, 8, 1125-1132, 1973.
- Huffines, G. R., Using the USU ionospheric model to predict radio propagation through a simulated ionosphere, *Master of Science Thesis*, Utah State University, UT, 1990.
- Jones, A. M., and J. J. Stephenson, A versatile three-dimensional raytracing computer program for radio waves in the ionosphere, *U. S. Dept. Comm. Off. Telecomm.*, Inst. Telecomm. Sci. OT Report 75-76, Washington, D. C., 1975.
- Moffett, R. J., and S. Quegan, The mid-latitude trough in the electron concentration of the ionospheric F-layer: a review of observations and modelling, *J. Atmos. Terr. Phys.*, 45, 315-343, 1983.
- Rush, C. M., Ionospheric radio-propagation models and predictions - a mini-review, *IEEE Trans. Ant. Prop.*, 34, 1163-1170, 1986.
- Schunk, R. W., The terrestrial ionosphere, *Sol. Terr. Phys.*, 27, 609-676, 1983.
- Schunk, R. W., A mathematical model of the middle and high latitude ionosphere, *PAGEOPH*, 127, 255-303, 1988.
- Schunk, R. W., P. M. Banks, and W. J. Raitt, Effects of electric fields and other processes upon the nighttime high-latitude F layer, *J. Geophys. Res.*, 81, 3271-3282, 1976.
- Sojka, J. J., Global scale, physical models of the F-region ionosphere, *Rev. Geophys.*, 27, 371-403, 1989.
- Sojka, J. J., and R. W. Schunk, A theoretical study of the high-latitude F region's response to magnetospheric storm inputs, *J. Geophys. Res.*, 88, 2112-2122, 1983.
- Spiro, R. W., R. A. Heelis, and W. B. Hanson, Ion convection and the formation of the mid-latitude F-region ionization trough, *J. Geophys. Res.*, 83, 4255-4264, 1978.
- Titheridge, J. E., The real-height analysis of ionograms: a generalized formulation, *Radio Sci.*, 24, 831-849, 1988.
- Whalen, J. A., The daytime F-layer trough and its relation to ionospheric-magnetospheric convection, *J. Geophys. Res.*, 94, 17,169-17,184, 1989.

APPENDIX

APPENDIX

The *Jones and Stephenson* [1975] ray-tracing computer program was developed for "tracing rays through an anisotropic medium whose index of refraction varies continuously in three dimensions," according to *Jones and Stephenson*. The program numerically integrates Hamilton's six differential equations to simulate ray propagation through the ionosphere, taking into account the effects of electron density, earth's magnetic field, and the electron-neutral collision frequency in the computation of the ionospheric refractive index. The main advantage of numerical ray tracing is its high degree of accuracy in simulating radio propagation. Long computer-processing time is the method's main disadvantage.

The ray-tracing program is written in standard Fortran and composed of 14-17 subroutines, depending on the propagation conditions the user chooses. The main program (NITIAL) initializes the ray-tracing conditions (transmitter location, wave frequency, azimuth, and elevation angles of transmission). A vital subroutine (TRACE) calculates the actual ray path, calling on other subroutines which numerically integrate and evaluate the differential equations (RKAM and HAMLTN). Another important subroutine is RINDEX, which calculates the phase refractive index and its three spatial gradients, in addition to the group refractive index and the polarization. Other subroutines are provided to refine the ray-path geometry and plot the ray path.

The program provides the user freedom to select the appropriate subroutines

desired for the models of electron density, earth's magnetic field, and the electron collision frequency. Several versions of each are provided. I used model output from the TDIM to simulate the three-dimensional trough electron density and its three spatial gradients in spherical-polar coordinates.

I chose to include the effects of the earth's magnetic field and electron-neutral collisions by using the Appleton-Hartree subroutine (AHWFWC). This subroutine used an earth-centered dipole approximation to model the geomagnetic field. I used a subroutine that combines two constant exponential-altitude profiles (EXPZ2) to model the electron-neutral collision frequency. Though these two effects were included in the ray-tracing calculation, they typically did not appreciably affect ray refraction. They should be used when considering radio-wave absorption and polarization effects on ray propagation.

I ray traced with the extraordinary ray component only. Table 8 lists the input conditions I kept fixed throughout the simulations. All other parameters (except transmitter location, frequency, azimuth, and elevation angle) were initialized by the program, and I did not change their values.

The collision frequencies CF_1 and CF_2 provided by the *Jones and Stephenson* [1975] ray-tracing program (listed in Table 8) were outdated. More appropriate values for CF_1 and CF_2 would be $8.58 \times 10^4 \text{ s}^{-1}$ and $1.65 \times 10^3 \text{ s}^{-1}$, respectively (D. Crain, private communication, 1991). Though I used the outdated collision frequencies, I verified that they did not affect the ray-tracing results in this study.

TABLE 8. Ray-Tracing Fixed-Input Conditions

Transmitter height	0.0 km
Receiver height	0.0 km
Number of ray hops	2
Gyrofrequency on the surface at the equator	0.8 MHz
Geographic latitude of the north magnetic pole	78.5° north
Geographic longitude of the north magnetic pole	291.0° east
Collision frequency (CF_1) at H_1	$3.65 \times 10^4 \text{ s}^{-1}$
H_1 , reference height	100.0 km
A_1 , exponential decrease of CF_1 with height	0.148 km^{-1}
Collision frequency (CF_2) at H_2	30.0 s^{-1}
H_2 , reference height	140.0 km
A_2 , exponential decrease of CF_2 with height	0.0183 km^{-1}
